Crystal-Liquid Transitions Studied With Colloids in an Electric Bottle

Crystal-Liquid Transitions Studied with Colloids in An Electric Bottle

A DISSERTATION PRESENTED
BY
HYERIM HWANG
TO
THE SCHOOL OF ENGINEERING AND APPLIED SCIENCES

IN PARTIAL FULFILLMENT OF THE REQUIREMENTS
FOR THE DEGREE OF
DOCTOR OF PHILOSOPHY
IN THE SUBJECT OF
APPLIED PHYSICS

HARVARD UNIVERSITY
CAMBRIDGE, MASSACHUSETTS
FEBRUARY 2016

Dissertation advisor: Professor Frans Spaepen
Professor David A. Weitz

Hyerim Hwang

Crystal-Liquid Transitions Studied with Colloids in An Electric Bottle

Abstract

This dissertation explores the crystal-liquid transition in a colloidal system. Model colloidal suspensions serve as analogues for the study of condensed matter because they display the same phase behavior as atoms or molecules. One key parameter that governs the phase behavior of all kinds of colloidal suspensions is the particle concentration. We used electric field gradients in an apparatus named "electric bottle", which provides a good control over the particle concentration. The spatial distribution of particles is set by dielectrophoresis at equilibrium, and crystallization occurs at high volume fractions. We used charge-stabilized colloidal systems with phase boundaries that depend on the charge. This way gives two types of crystals (body-centered cubic and face-centered cubic crystals). With confocal microscopy, we directly imaged the colloidal suspension in three dimensions. We investigated two kinds of crystal-liquid transitions. First, we studied crystallization and melting at the single particle level by switching the electric field on and off. We investigated the kinetics of solidification and melting at the crystal-liquid interface by measuring the attachment and detachment rates. The attempt frequency for crystallization is given by the random walk, in analogy to collision-limited growth of atomic crystals. The driving force for melting and solidification is obtained from a biased random walk analysis. The interface mobility for melting is greater than that for crystallization. Second, we performed a study of the equilibrium interface between the body centered cubic crystal and the liquid. Equilibrium fluctuations were observed and the stiffness of the interface is determined by the capillary fluctuation method. The high-index interfaces and those with rectangular symmetry show isotropic stiffness, and they are less stiff than those in hard-sphere colloids. We studied on a charged-colloidal system with long range repulsion that crystallizes into a body-centered cubic crystals at low volume fractions, and transforms to a face-centered cubic crystals at higher volume fractions during dielectrophoretic compression.

To my parents.

Contents

Listing of figures

Listing of tables

Acknowledgments

First and foremost, I would like to express my deepest gratitude to my supervisor, Prof. Frans Spaepen for his continuous support and patience throughout my Ph.D study. He has been always there for me to listen and give advice. His immense knowledge and enthusiasm motivated me and his guidance was always valuable in all the time of research. I could not have imagined having a better advisor and mentor for my study.

My sincere gratitude also goes to my another supervisor, Prof. David Weitz. I have been fortunate to have an advisor who gave me both the freedom to explore the science on my own and at the same time the guidance to overcome when my steps toward science faltered. He taught me how to question thoughts and how to express ideas.

Besides my advisors, I would like to acknowledge my thesis committee Prof. Vinny Manoharan for his insightful questions and fruitful comments. I also thank my qualifying exam committees, Prof. Jennifer Lewis and Dr. Ian Morrison. I am very grateful to them for the discussions that helped me widen my work from various perspectives.

I have been aided for many years with developing the apparatus in various electric shops. Winfield Hill in Rowland Institute helped me to make an essential part of my experimental set up. Jim MacArthur gave me a useful advice to design an electric bottle and solve technical details of my work. The late Frank Molea has provided his old equipment that I needed for the electrical measurements.

I was an amazingly lucky person to have wonderful colleagues in my daily life. Not only scientific discussions but also casual conversations with Zsolt Terdik, Emily Redston, and Georgios Tsekenis have made my time at Harvard more pleasant. My first colloid tutors, Emily Russell, Kate Jensen, and Tom Kodger, gave me many lessons for the experiments at the beginning of the study. I have also benefited from the conversations with many others, particularly Joe McDermott, Manis Chaudhuri, and Adrian Pegararo.

A very special thanks goes to Korean friends whom I met at Harvard, especially Junhyun Lee, Jeongmo Choi, Jeeeun Choi, and Jeongyun Kim. Their constant care and support all these years helped me to stay focused on my graduate study. I deeply appreciate them and I would never forget the time we supported and encouraged each other.

Last but not the least, I would like to thank my family. My parents, Sanggeun Hwang and Heakyung Park have been a constant source of love, concern, support and strength throughout my life. My two sisters, Junghyun and Jungwon always supported me spiritually and encouraged me with their best wishes. I must give a special mention for the support given by my husband Shinhyun who is also one of my best scientific mentors. None of this would have been possible without the love and patience of him.

1

Introduction

1.1 Colloids

A "colloid" refers to a mixture of particles dispersed in a solvent. The particles have diameters ranging in 1 $nm \sim 1\ \mu m$, which is larger than the size of molecules[1]. We can classify the colloids as sol, emulsion, foam, and aerosol based on the phases of the particles and the suspending medium. We encounter colloids of these various forms in everyday life, although we may not realize it. Milk, mayonnaise and ice creams are representative colloids in food, in that they all have particles as one substance of a mixture. Cosmetic products are also colloids in a form of an emulsion, which involves two immiscible liquids. Besides these, colloids are also used in many other industrial applications such as the paint, pharmaceutical, and detergent industry.

These uses in wide areas are primarily due to the complexity of their behaviors. Therefore, the understanding of colloidal systems has been a central issue from both fundamental and practical standpoints.

1.2 Colloids as model systems

In the early 1900s, Perrin found that colloidal particles move around in a random path due to the collisions with the solvent molecules, thereby performing a Brownian motion[2]. The thermally induced Brownian motion causes the colloids to display phase behaviors similar to that of as atoms or molecules. Micrometer-scale colloidal particles are sufficiently large ($\sim 1\ \mu m$) to be observed by optical techniques and the speed of their motion is slow enough ($\sim 0.1\ sec$) which makes it possible to investigate the dynamics of individual particles'. These properties make colloids important model systems, which is exactly what we use them for in this thesis[3,4]. We make use of the analogy between colloids and atoms to study dynamics of the condensed matter because their phase behavior is very similar. Many of the interactions such as hard sphere or electrostatic interactions which determine the behavior of the condensed matter, also determine the behavior of the colloids.

The experimental model system that we use is the colloidal suspension: solid particles dispersed in a liquid. As colloidal particles themselves are hard objects, the particles can act as hard spheres (referred as 'excluded volume interaction') when the system is made to have only infinite repulsion when they touch. The system can be tuned to have other interactions, such as soft repulsive interaction, or attractive interaction, which result in richer phase behavior.

The interaction is tuned by the screening length of the particles and the ionic strength of solvent[5]. Colloidal particles are charged spheres because they always have surface charges due to their intrinsic chemistry. When the particles are suspended in a solvent, ions in the solvent can be absorbed to or released from the surface of the particles. The ions can screen the surface

charge, thus tuning the interaction between particles. In a solvent of low ion concentration, the Coulomb interaction is dominant because the surface charges are not sufficiently screened. In a solvent with salt, on the other hand, the interaction can be tuned to have hard-sphere-like interactions by screening the surface charges.

1.2.1 Hard Spheres

Hard spheres have the simplest interaction, which has no interactions between particles except the excluded volume. That is to say, they have extremely strong repulsion at very close distances, and zero for all other cases, as indicated in Equation 1.1 where a is the radius. This behavior is an extreme form of the short range repulsion in the Lennard-Jones potential which is due to the Pauli exclusion principle[6]. Therefore, in hard spheres, the phase selection depends only on the volume fraction. In other words, the phase behavior of hard spheres is completely determined by entropy. In 1986, Pusey and van Megen first experimentally showed the phase behavior of nearly-hard spheres[7]. The phase diagram of hard spheres as a function of volume fraction is shown in Figure 1.1. Hard spheres are first crystallized when the packing fraction reaches about 0.50[8]. They can be packed further up to 0.74 when they are close-packed. The hard spheres can form glass which is a liquid-like structure kinetically trapped in the range of $0.58 \sim 0.64$.

$$U(r) = \begin{cases} \infty, & r < 2a \\ 0, & r \geq 2a \end{cases} \tag{1.1}$$

1.2.2 Soft spheres: our experimental system

Colloids can have soft interaction potentials by having a long range repulsion. Technically, we can give repulsive interaction to the particles by keeping the particles' surface charge or adding

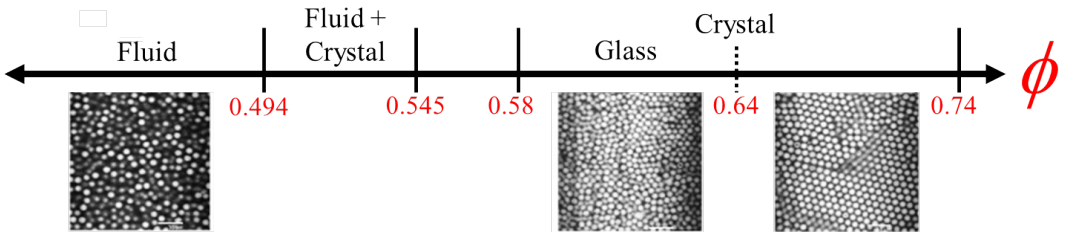

Figure 1.1: Phase diagram of hard sphere system as a function of volume fraction, ϕ. As the volume fraction increases, the colloidal suspension goes from the liquid to the crystal phase[9].

additional electrolytes which carry charges to the solvent. Each charged colloid is surrounded by a cloud of charges, which keep the colloids separated, thus stabilizing the colloidal suspension. A soft sphere interaction potential is defined in Equation 1.2 where a is a radius of a particle.

$$U(r) = \begin{cases} \epsilon \left(\frac{\sigma}{r}\right)^n, & r \leq 2a \\ 0, & r > 2a \end{cases} \tag{1.2}$$

Commonly, the interaction of soft spheres is controlled by the electrical double layer as the particles with surface charge interact by screened electrostatic repulsion. The surface charge of a particle is balanced by charges in the solvent, and an electrical double layer is a layer that forms around a surface charge to neutralize it. The charges are concentrated around the surface by forming a first monolayer (the Stern layer), with further charges are distributed in the next layers. The interaction potential, depicted in Figure 1.2 (a), decreases exponentially through the layers. The Debye length, κ^{-1} is the thickness of the double layer, which is often used to characterize the range of the interaction. Figure 1.2 (b) shows a Debye sphere, whose radius is the Debye length plus the particle diameter. Each colloidal particle in a charged suspension is surrounded by Debye sphere, in which the charges are electrically screened.

The phase behavior of the soft colloids is different from that of hard spheres. One example

(a)

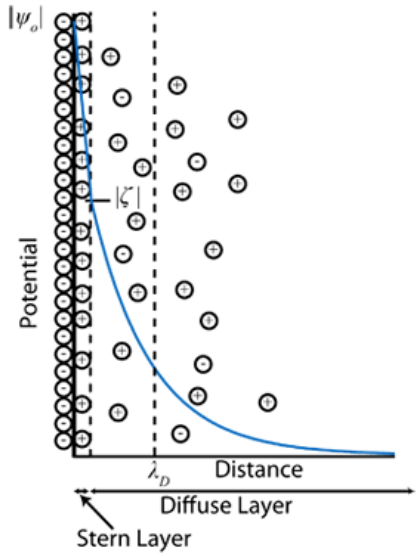

(b)

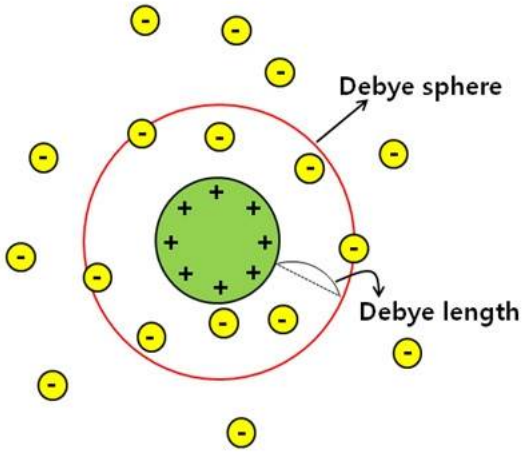

Figure 1.2: a) Schematic of the electrical double layer. b) Debye sphere.

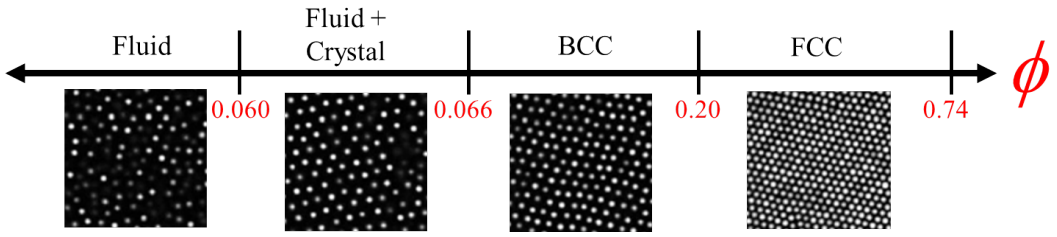

Figure 1.3: Phase diagram of soft sphere system as a function of volume fraction, ϕ. As the volume fraction increases, the colloidal suspension goes from the liquid phase to the BCC crystal phase. With a further compression, the BCC crystal phase transforms to the FCC crystal phase[11].

of phase diagram of a charge-stabilized colloids is shown in Figure 1.3. Spherical colloidal particles crystallize into body-centered cubic (BCC) crystals at low packing fractions because higher repulsive interaction potential shifts the phase boundary[10]. As the particles are packed more closer, the crystal structure is transformed to face-centered cubic (FCC) crystals.

Another common colloidal interaction is a short-range attractive one called the depletion force[12]. The force is caused by an osmotic pressure when the suspension contains additional polymers or particles whose size is smaller than that of the dispersed particles. When two colloidal particles are close and surrounded by the polymers, there is a space where the polymers can not penetrate. This results in pushing the two particles with a certain pressure and attracting each other.

In this thesis, we use the charge-stabilized colloidal system with a soft repulsive interactions. The experimental details of the suspension will be described in Section 3.1.2.

1.2.3 Confocal microscopy

Optical microscopy has been a powerful tool to observe many systems whose length scales are in the range of the wavelengths of visible light. However, the interaction with light limits the depth of the observation. In biological samples or dense colloidal suspensions, the light scatters

from the interfaces, thus obscuring images.

Marvin Minsky first introduced the confocal microscopy, which is widely used to study the three dimensional structures and their dynamics. He tried to solve the depth of focus limitation of the optical microscopy by making two main improvements. His first patent is shown in Figure 1.4. He used a point illumination and a pinhole aperture in the image plane to remove out-of-focus light. Figure 1.5 shows a schematic of a confocal microscope. Light from a laser passes through a dichroic mirror, and enter the microscope objective. The fluorescent sample is excited by the light, which is returned and passes back through the microscope objective. It is reflected by the mirror and reaches a confocal pinhole. The pinhole plays an essential role, in that it collects only the light coming from the focus plane and rejects all out-of-focus light. Photomultiplier tube (PMT) detects the light coming through a pinhole. A confocal microscope scans from point to point, thus, the complete 3D image is reconstructed from 2D slice images. Confocal microscopy is used a lot for observing biological samples, but also in dense colloidal systems. Studies to find a solvent to match refractive index of the particles have made colloids as a better model systems[3]. Further improvements of the speed and resolution allow us to study the dynamics of condensed matter by scanning the colloidal system in real time. Figure 1.6 is an image of fluorescently dyed PMMA particles suspended in organic solvents, taken by the confocal microscope.

1.3 Colloids under external control

A variety of fields have been used to manipulate the the concentration, growth, or structure of colloids. It is important from a fundamental point of view because it allows us to study phase behavior and transitions in detail. The particle concentration is a critical factor in the phase behavior of all colloidal suspensions. In the hard sphere system, the phase behavior is completely determined by a volume fraction. Even for soft spheres in Figure 1.3, a volume

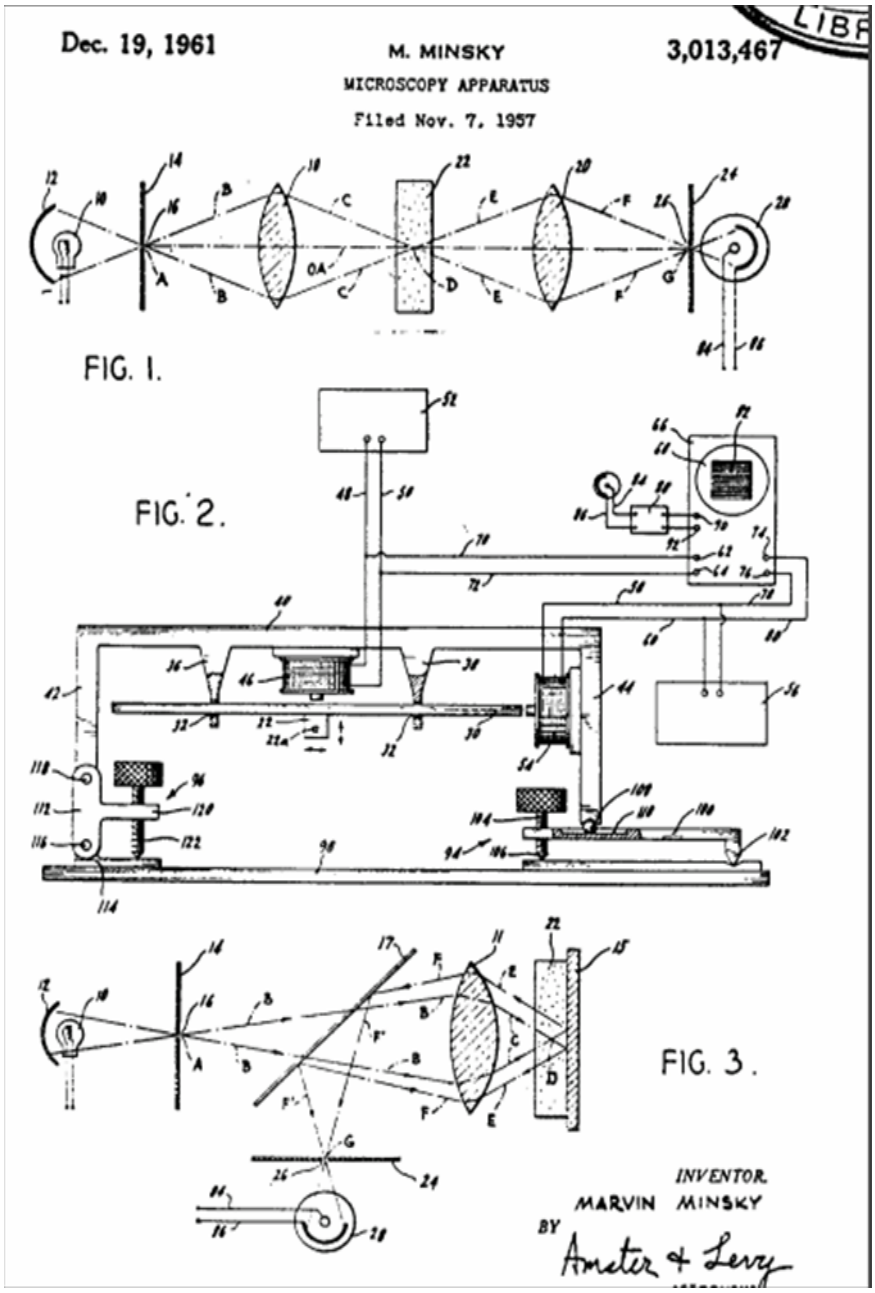

Figure 1.4: Marvin Minsky's patent of the confocal microscope. Fig. 1 is a schematic showing the principle of the transmission confocal scanning microscope, whose side view is shown in Fig. 2 and Fig. 3 in a single-lense configuration.

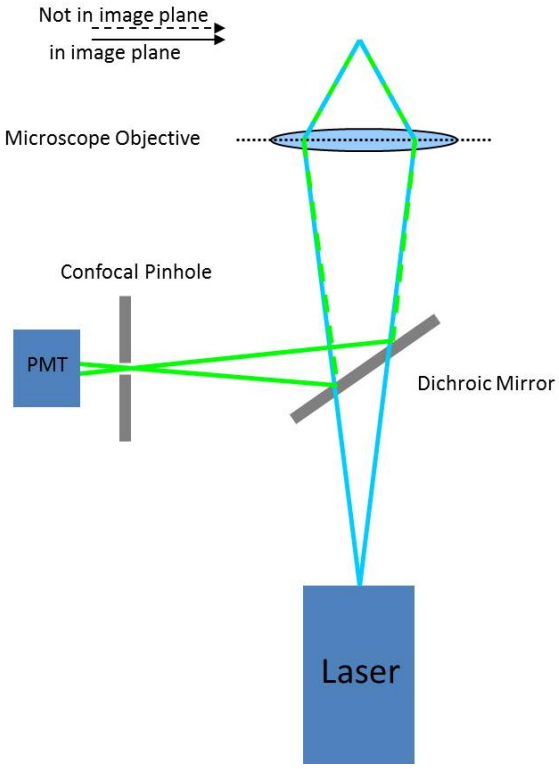

Figure 1.5: A schematic figure of a confocal microscopy. Illumination and returning light are colored by blue and green, respectively.

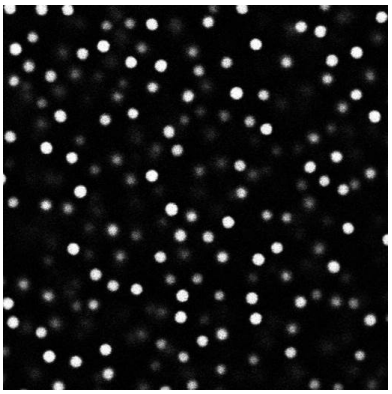

Figure 1.6: A confocal image of 1.7 μm fluorescently dyed PMMA colloidal particles suspended in an organic solvent.

fraction is still an important factor. Thus, a control over the particle concentration enables us to observe the growth from one phase to another.

1.3.1 Gravity, temperature gradient

Most colloid samples whose density does not match that of the solvent sediment or cream and they form gravity-induced colloidal crystals. In 1997, the Chaikin group performed the crystallization experiments in microgravity in Space Shuttle to investigate gravity effects on the crystallization[13]. They grew height-dependent colloidal crystals in two different environments as shown in Figure 1.7 (a). The structure of the colloidal crystals grown in microgavity is different from that grown in normal gravity. Although the microgravity experiments gave information about the field effects on crystallization, gravity as a body force has limitations, in that it is not easy to manipulate dynamically. Temperature gradient, another body force, can also induce crystallization by forming a density gradient[14]. The osmotic pressure is linearly related to the temperature. Figure 1.7 (b) shows the osmotic pressure as a function of volume fraction at two different temperatures. The crystal growth can be controlled by tuning the temperature gradient. While the temperature gradient allows good control, it is limited by the freezing and boiling points of the solvent.

1.3.2 Electric field gradient: previous studies

An electric field gradient also can be used as a body force to control particle concentration and concentration gradient. Electric fields allow better control than other body forces because localized manipulation and real-time adjustment are possible. Also, its intensity and frequency can be tuned easily. When a particle is exposed to an electric field, it experiences two kinds of electrokinetic forces: electrophoresis and dielectrophoresis. Electrophoresis is the motion of particles in a uniform field and is determined by the net intrinsic electrical charge of the

(a)

(b)

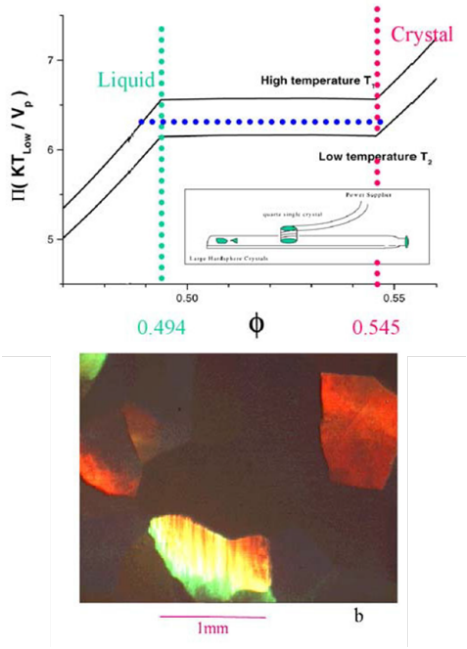

Figure 1.7: a) Gravity-induced colloidal crystals. b) Temperature-gradient induced colloidal crystals where the osmotic pressure is linearly related to the temperature.[13,14]

particle. Dielectrophoresis is the motion of particles in a non-uniform field and is determined by field-induced charges. Two electrokinetic forces are described by Equation 1.3, where the first term and the second term stand for electrophoresis and dielectrophoresis, respectively. In Equation 1.3, q is a charge and $\vec{p}$ is an induced dipole moment in an electric field $\vec{E}$.

$$\vec{F} = \vec{F}_{EP} + \vec{F}_{DEP} = q \cdot \vec{E} + (\vec{p} \cdot \nabla)\vec{E} \tag{1.3}$$

The dielectrophoretic force results from the induced dipole of dielectric particles interacting with a non-uniform electric field[15]. More details about the dielectrophoresis will be given in Section 2.4. In 2006, Chaikin's group first designed an experimental setup to trap the colloidal particles by the dielectrophoresis[16]. As shown in Figure 1.8, it is a capacitor filled with a colloidal suspension. It produces a uniform field under the electrode and, a non-uniform field under the electrode-free region, which finally causes a concentration gradient. Basically the most polarizable material climbs the field gradient towards the highest field region to minimize macroscopic electrostatic energy. In their experiment, as the colloidal particles are more polarizable than the suspending medium, they are attracted toward the region of strong electric field. Starting from a dilute colloidal suspension, the concentration became denser in the central region where the electric field is stronger, whereas the region far outside the electrode becomes more dilute. The ability of the setup to create the steep density gradients allows us to study a concentration-dependent phase diagram in a single device.

Electric field induced charges depend on the dielectric constant contrast of particle and solvent. Opposite to the earlier work, we can change the direction of particles' movement by changing the solvent. van Blaaderen's group showed negative dielectrophoresis-induced particle transport[17]. The particles with lower polarizability are repelled from the regions of strong electric field, and are concentrated in the center of the slit. Figure 1.9 shows the Bragg reflection

(a)

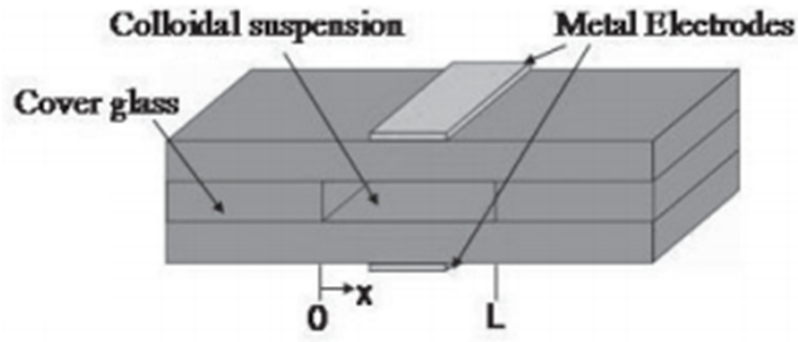

(b)

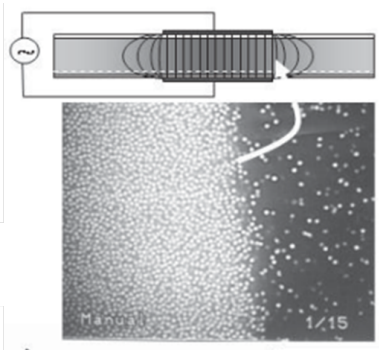

Figure 1.8: a) Schematic figure of an electric bottle. b) Steep density gradient induced by dielectrophoresis in an electric bottle.[16]

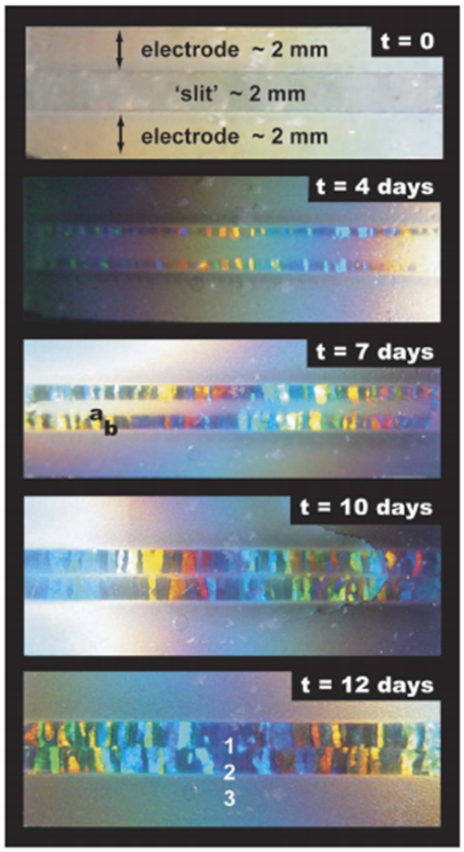

Figure 1.9: Bragg reflection images of crystallization induced by negative dielectrophoretic compression.[17]

in crystals formed by negative dielectrophoresis. We see from these reflection that the crystals nucleated at the edge of slits and grew inwards until they met in the center.

The time-dependent changes in the particle concentration in a single device will allow us to observe the crystal growth mechanism. Based on the ideas above, we developed an "electric bottle" for our experimental goals, which will be discussed in Section 3.2.1.

1.4 Contents of this dissertation

This dissertation consists of two parts. In the first part, Chapters 2-3, we introduce an experimental setup that enables us to manipulate the colloidal particle concentration, and we study the background of dielectrophoresis and the suspension characteristics. The second part is a study of the crystal-liquid transitions observed in an electric bottle. Chapter 4 presents the results on crystallization and melting kinetics of two types of crystals studied at the single particle level. We measured the attachment and detachment rates and identified the kinetics of growth mechanism. Chapter 5 presents the results of measurement of the stiffness of an equilibrated interface between a BCC crystal and the liquid. In Chapter 6, we show observations of the solid-solid transformation between BCC and FCC crystals.

2

Background

In this chapter, we study the dynamics of colloids and their interactions between them, which are essential background for the study. We also introduce dielectrophoresis which is a body force to control the particle concentration and induced dielectrophoretic equilibrium.

2.1 Dynamics of colloids

Colloidal particles suspended in a solvent have interesting dynamics that are essential to their use as model atoms. The particles perform a random motion that results from the collisions

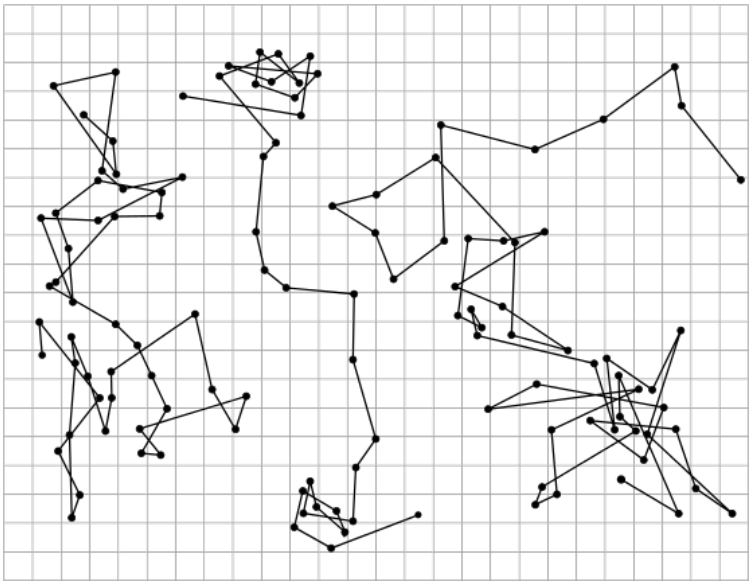

Figure 2.1: The trajectory of 0.53 μm diameter colloidal particles. Positions are measured once every 30 seconds.[18]

with solvent molecules, which is often called Brownian motion. In Figure 2.1, the trajectories of colloidal particles of 0.53 μm suspended in a fluid are shown[18]. Each point indicates the position of the particle, measured once every 30 seconds.

Einstein first derived the diffusion coefficient of a particle undergoing Brownian motion in a fluid, which is called the Stokes-Einstein equation[19]. The diffusion coefficient D of a particle of radius r in a fluid with a viscosity η at temperature T is

$$D = \frac{k_B T}{6\pi\eta r}, \tag{2.1}$$

where k_B is the Boltzmann constant. Einstein related the diffusion coefficient D to the mean square displacement (MSD) of a particle as a function of observation time Δt. Equation 2.3 describes how the mean squared displacement of particles in a fluid scale with time when they are moving caused by thermal motion, where n is the number of spatial dimensions and Δx are

the displacements during the measurements. x_0 is the reference position of the particle.

$$MSD = \langle (x - x_0)^2 \rangle = \frac{1}{\Delta t} \sum_{t=1}^{\Delta t} (x(t) - x_0)^2 \tag{2.2}$$

$$\langle \Delta x^2 \rangle = (2n) D \Delta t \tag{2.3}$$

2.2 DLVO THEORY: ELECTROSTATIC INTERACTIONS OF COLLOIDS

The repulsive interaction which stabilizes the like-charged colloids is a type of electrostatic interaction, as mentioned in Section 1.2.2. The interaction can be explained by the DLVO (Derjaguin, Landau, Verwey, and Overbeek) theory, which is a dispersion stabilizing theory[20]. It describes the balance between two forces: van der Waals attraction and electrostatic repulsion, as depicted in Figure 2.2. The Van der Waals attraction results from the forces between molecules in each colloidal particle. The electrostatic repulsion appears when two colloids approach and their electric double layers begin to interfere. The potential has a maximum due to the surface charge at contact and it decreases to zero outside the electric double layer. The DLVO theory describes the tendency of colloids to either aggregate or separate by combining the two potentials of attraction V_A and repulsion V_R.

$$V = V_A + V_R \tag{2.4}$$

Here, we mostly used the repulsive colloidal system, where the net total interaction potential is electrostatic-dominant. As explained in Section 1.2.2 briefly, a surface in a solvent is charged from either dissociation of surface charges of the particles or adsorption of charged polyelectrolytes from the surrounding solution. The surface charge is counterbalanced by the ions in the solvent, which results in the formation of the electric double layer in Figure 1.2. The Stern layer

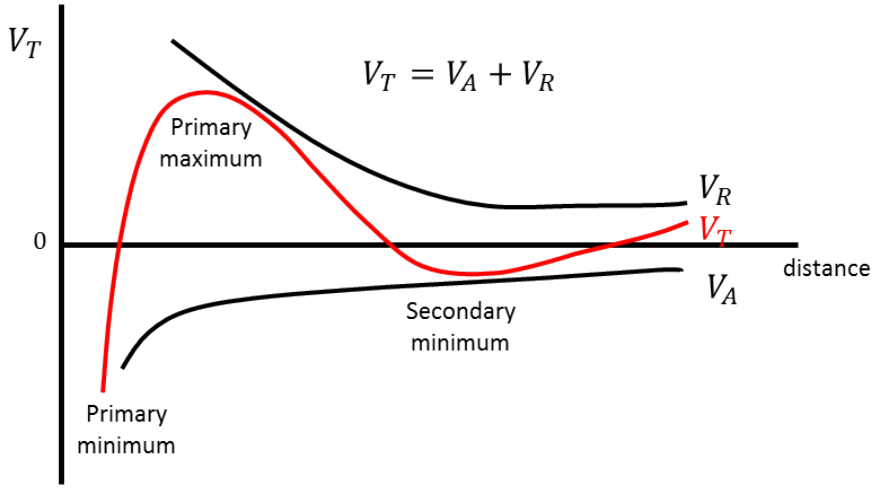

Figure 2.2: Potential energy curves of dispersion. Van der Waals attraction potential, electrostatic repulsion potential, and the combination of the two opposite potentials as a function of distance between particles are shown.

is immobile as the charges are strongly attached to the surface. The diffuse layer is relatively mobile because the charges are loosely bound to the surface. We can tune these layers by changing the ionic condition of solvent. The thickness of the double layer, inverse Debye length κ is described as

$$\kappa = \sqrt{\frac{\epsilon_r \epsilon_0 k_B T}{\Sigma \rho_{\infty i} e^2 {z_i}^2}}, \tag{2.5}$$

where $\rho_{\infty i}$ is the density of ion i in the solution, z is the valence of the ion, ϵ_0 is the vacuum permittivity, and the ϵ_r is the relative permittivity[3].

2.3 Charged colloids in nonpolar solvents

Charges dissociate easily in a polar solvent, whereas they do not in a non-polar solvent due to its low polarizability. To control charging in a nonpolar solvent, the surfactant molecules are used because they are amphiphilic. The surfactants form aggregates in the form of inverse micelles,

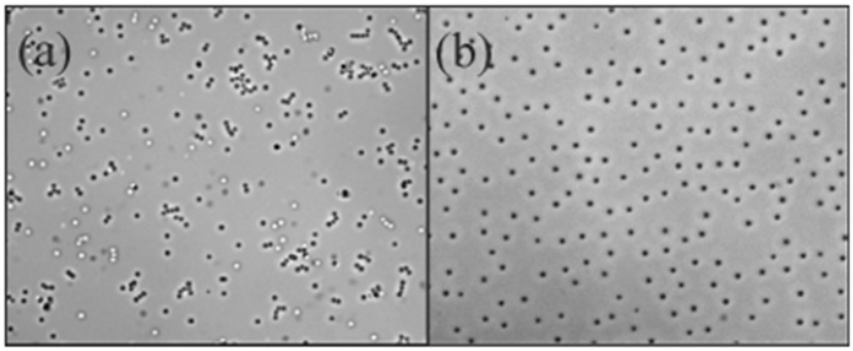

Figure 2.3: Colloidal particles in (a) pure dodecane solvent and (b) 12 *mM* AOT containing dodecane solvent.[21]

with their polar head groups aggregating to make a core, and their nonpolar tails exposed to solvent. The polar head groups play a role as charge carriers, which stabilize the charged colloids in a nonpolar solvent.

A surfactant molecule widely used as a stabilizing agent is dioctyl sodium sulfosuccinate, often called AOT. The AOT micelle behavior in a nonpolar solvent has been studied by Weitz's group[21]. Figure 2.3 shows the charge stabilization by the addition of AOT. The inverse micelles that are formed above the critical micelle concentration (c.m.c) act as a salt, thereby determining the ionic strength of the solvent. Adding AOT to a dodecane solvent results in an increase of the conductivity and inverse screening length as shown in Figure 2.4. They found that the AOT concentration controls the range of the interaction, with higher AOT concentrations giving a stiffer interaction. Similar results using a different nonpolar solvent mixture were achieved recently by the same group [22]. The nonpolar solvent mixture is composed of *cis*-decalin and tetrachloroethylene (TCE) which is the solution used in this thesis.

Figure 2.5 shows the phase behavior of a colloidal suspension of $\phi = 0.23$ as a function of AOT concentration. The phase changes from BCC crystal to FCC crystal and to a fluid in Figure 2.5 (b) to (d), which indicates that the interaction becomes more short-ranged with increasing

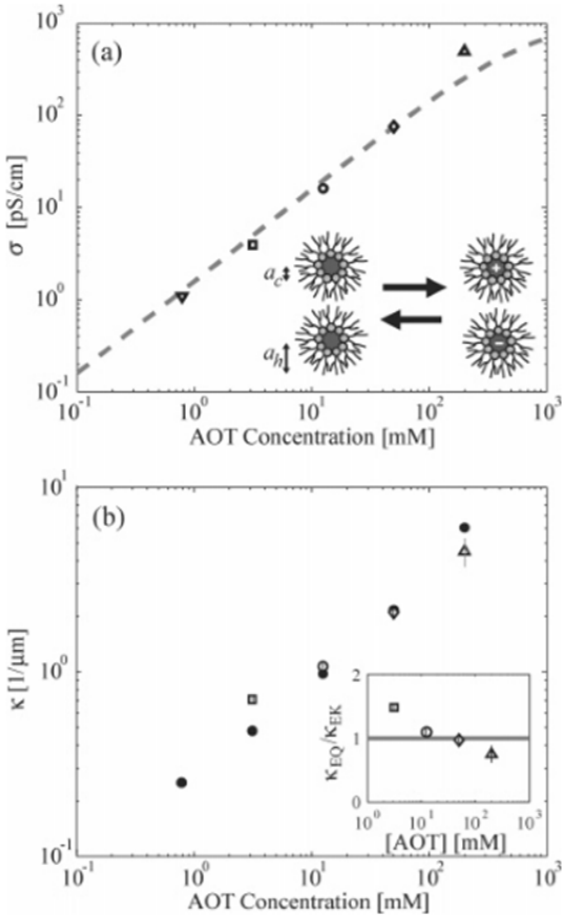

Figure 2.4: AOT inverse micelles in a dodecane solvent. (a) Conductivity of the solution with no particles. (b) Inverse screening length from conductivity.[21]

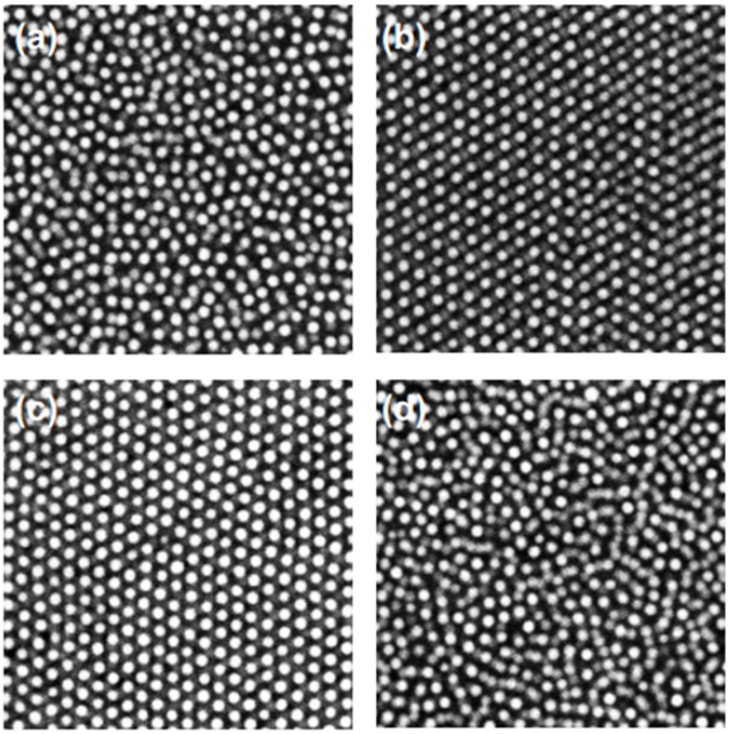

Figure 2.5: Confocal images of colloidal suspensions with different AOT concentration. (a) 1 *mM*, liquid (b) 5 *mM*, BCC crystal (c) 50 *mM*, FCC crystal (d) 200 *mM*, liquid.[22]

the AOT concentration. The liquid phase in Figure 2.5 (a) is for uncharged particles, since the low AOT concentration is below the critical micelle concentration.

2.4 Dielectrophoresis

Dielectrophoresis is an electrokinetic phenomenon, which was first described by Herbert Pohl in 1951[15]. It is the movement of a neutral object in a dielectric fluid in an inhomogeneous electric field, where the electric field can either be DC or AC. Under an electric field, any kind of dielectric materials obtain an induced dipole moment $\vec{p}$

$$\vec{p} = \alpha \vec{E}, \tag{2.6}$$

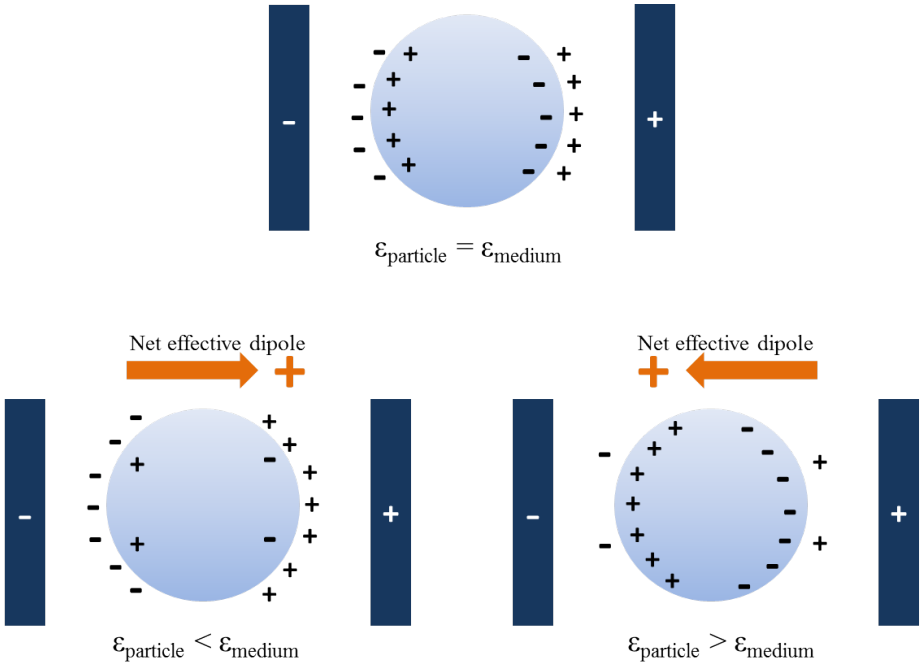

Figure 2.6: Direction of the effective dipole moment induced in a dielectric particle with dielectric constant $\varepsilon_{particle}$ in a dielectric medium with dielectric constant ε_{medium} in a homogeneous electric field.

where α is the polarizability and E is the electric field. A dielectrophoretic force F_{DEP} is exerted on the induced dipole moment p in the field with a non-zero gradient tensor $\nabla\vec{E}$,

$$F_{DEP} = (\vec{p} \cdot \nabla)\vec{E}. \tag{2.7}$$

2.4.1 Induced polarization and electric forces

Figure 2.6 sketches the direction of the effective dipole moment. The induced dipole moment vanishes when the particle and the medium have the same dielectric constant. Otherwise, the unpaired surface charges that result from the dielectric constant mismatch of the two dielectric materials, induce a net effective dipole moment.

(a)

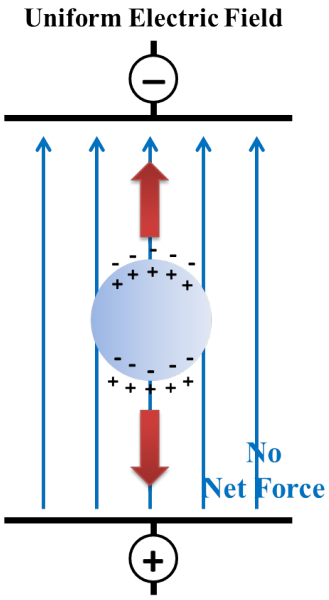

$$\vec{F}_{DEP} = (\vec{p} \cdot \nabla)\vec{E} = 0$$

(b)

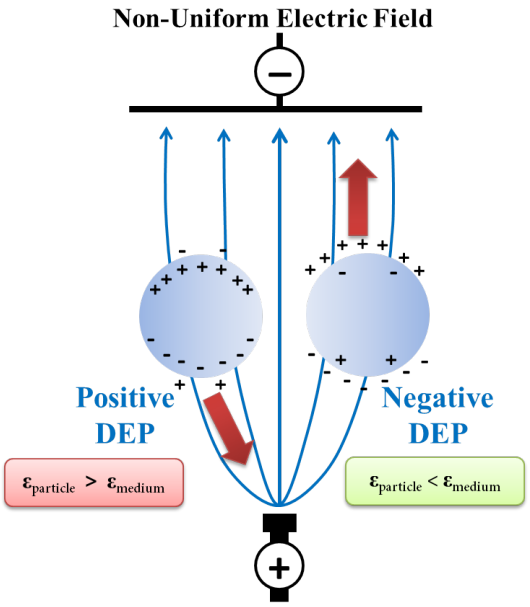

$$\vec{F}_{DEP} = (\vec{p} \cdot \nabla)\vec{E} \neq 0$$

Figure 2.7: Schematic illustrating dielectrophoresis resulting from (a) a homogeneous electric field and (b)an inhomogeneous electric field.

The dielectrophretic force appears when the field gradient and the induced dipole moment interact. The dielectrophoretic forces in a uniform and a non-uniform field are drawn in Figure 2.7. In a uniform field where the field gradient is zero, the particle does not experience any dielectrophoretic forces. In Figure 2.7 (b), the field gradient is stronger where the lines converge. Particles with dielectric constant $\varepsilon_{particle}$ are placed in a dielectric medium with dielectric constant ε_{medium}. Dielectric materials with lower dielectric constant contain a few polarization charges, whereas those with higher dielectric constant contain more polarization charges. Thus, dielectrophoresis pulls the more polarizable particle towards the strong field, while the less polarizable particle is repelled away from the strong field.

2.4.2 Dielectrophoretic force

The dielectric particle obtains an induced dipole moment p of the Equation 2.6, with a strength of

$$\vec{p} = 4\pi\varepsilon_m \left(\frac{\varepsilon_p - \varepsilon_m}{\varepsilon_p + 2\varepsilon_m} \right) r^3 \vec{E}. \tag{2.8}$$

The fraction in Equation 2.8 is referred to as the Clausius-Mossotti factor $K(\varepsilon_1, \varepsilon_2)$[23],

$$K(\varepsilon_1, \varepsilon_2) = \frac{\varepsilon_2 - \varepsilon_1}{\varepsilon_2 + 2\varepsilon_1}. \tag{2.9}$$

The Clausius-Mossotti factor will be explained with more detail in Section 2.4.3. The dielectrophoretic force F_{DEP} acting on the dipole moment $\vec{p}$ under an inhomogeneous field $\vec{E}$ is

$$\begin{aligned} F_{DEP} &= 4\pi\varepsilon_m \left(\frac{\varepsilon_p - \varepsilon_m}{\varepsilon_p + 2\varepsilon_m} \right) r^3 (\vec{E} \cdot \nabla)\vec{E} \\ &= 2\pi\varepsilon_m \left(\frac{\varepsilon_p - \varepsilon_m}{\varepsilon_p + 2\varepsilon_m} \right) r^3 \nabla \mid \vec{E} \mid^2, \end{aligned} \tag{2.10}$$

where $\nabla \mid \vec{E} \mid^2 = 2\vec{E} \cdot \nabla\vec{E}$.

2.4.3 Dielectrophoresis in an AC field

A dielectrophoretic force can be observed under with AC or DC conditions. In AC, monopoles in a dielectric material do not change their mean position. Also, the AC mode allows dielectrophoresis in charged materials that conduct. As the Clausius-Mossotti factor which governs the effective dipole moment depends on frequency, we can gain control over the dielectrophoretic force by changing the sign of K in Equation 2.9. The polarizability of a material, often quantified by the dielectric constant, depending on the frequency of the electric field. Frequency-dependent dielectric constants are shown in Figure 2.8 (a). The dielectric constant is complex, with ε' related to the stored energy of the medium and ε'' related to the loss of energy. Figure 2.8 (b) shows the plot of the real and imaginary parts of the Clausius-Mossotti factor as a function of frequency. For all experiments in this thesis, we applied AC electric fields at 1 MHz. As shown in Figure 2.8, the real parts of the Clausius-Mossotti factor is dominant under this condition, and hence we will exclude the imaginary part.

2.5 Dielectrophoretic equilibrium in an electric bottle

We employed dielectrophoresis in our "electric bottle", to manipulate the particles and to establish different equilibrium states.

The Helmholtz free energy F of a colloidal suspension in the presence of an external potential can be written as,

$$F = F_0(\phi) + W(\phi, \vec{E}) \cdot V \tag{2.11}$$

where $F_0(\phi)$ is the free energy of the suspension without the field, which is mostly determined by the number density of particles. $W(\phi, \vec{E}) \cdot V$ is the external energy contributed by the electric

(a)

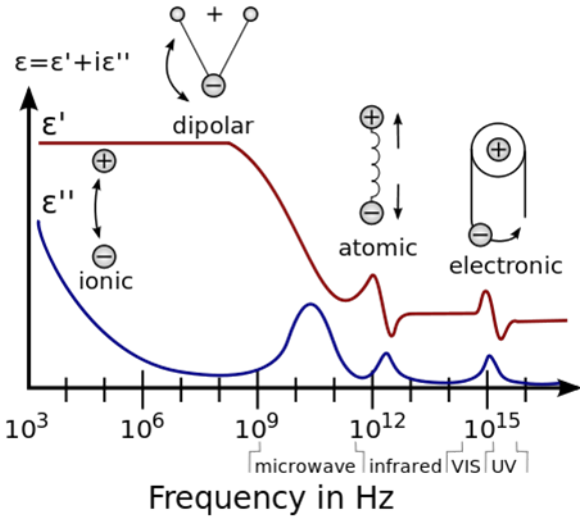

(b)

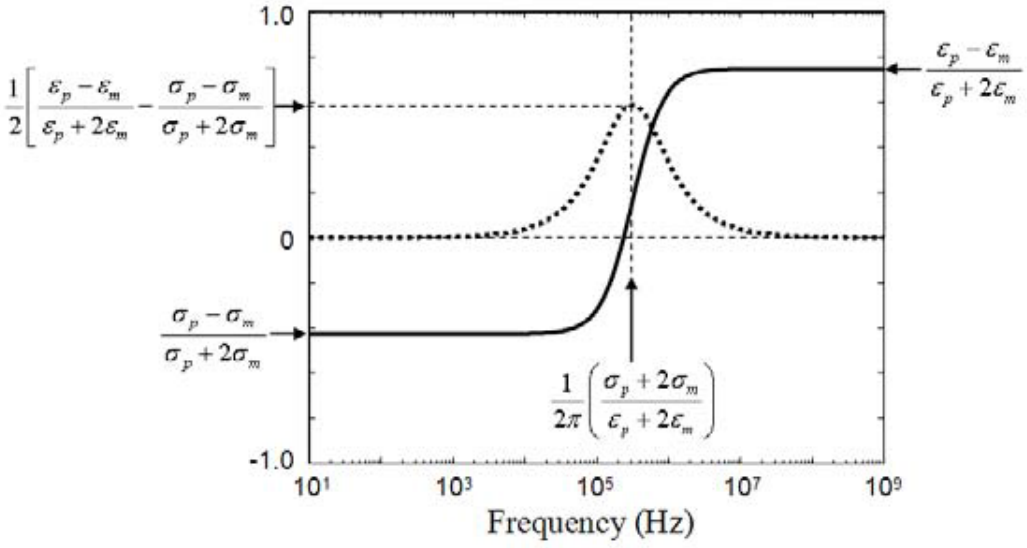

Figure 2.8: Clausius-Mossotti factor. (a) Dielectric constants as a function of frequency[24].(b) Variation of the real and imaginary parts of the Clausius-Mossotti factor with frequency.

field. The chemical potential of the suspension μ is

$$\begin{aligned}\mu &= \left(\frac{\partial F}{\partial N}\right)_{T,V} \\ &= F_0\prime(\phi)\frac{\partial \phi}{\partial N} + V_p\left(\frac{\partial W}{\partial \phi}\right)_{T,V},\end{aligned} \tag{2.12}$$

where the first term is the chemical potential of the suspension without the external field, and the second term is the change in chemical potential by the electric field. Here, the second term comes from

$$\left(\frac{dW}{dN}\right)_{T,V} V = \left(\frac{\partial W}{partial\phi}\frac{\partial \phi}{\partial N}\right)_{T,V} V, \tag{2.13}$$

where $\phi = NV_p/V$ is a volume fraction and its derivative is $d\phi/dN = V_p/V$.

Under the action of electric field gradient, the colloidal particles move until the electrostatic energy is counterbalanced by the chemical energy. Once the system finally reaches equilibrium, the total chemical potential μ must be the same everywhere, $\nabla\mu = 0$.

$$\nabla\mu = \frac{\partial}{\partial x}\left(F_0\prime(\phi)V_p + V_p\frac{\partial W}{\partial \phi}\right) = 0 \tag{2.14}$$

From the equation 2.14, we get

$$\left(F_0\prime\prime(\phi) + \frac{\partial^2 W}{\partial \phi^2}\right)\nabla\phi = -\frac{\partial^2 W}{\partial\phi\partial(E^2)}. \tag{2.15}$$

$F_0\prime\prime(\phi)$ can be obtained from the equation of state:

$$\Pi_0 V = NZ(\phi)k_B T, \tag{2.16}$$

where $Z(\phi)$ is the compressibility factor. The osmotic pressure Π is:

$$\begin{aligned}\Pi &= -\frac{\partial F}{\partial V} \\ &= \Pi_0 - W(\phi, E) + \phi\frac{\partial W}{\partial \phi}\end{aligned} \tag{2.17}$$

From the equation of state and the Equation 2.17, we obtain

$$\frac{\phi}{V_p}Z(\phi)k_BT = -F_0(\phi) + \phi F_0\prime(\phi). \tag{2.18}$$

Taking the derivative of equation 2.18 with respect to ϕ, gives

$$k_BT\left(\frac{Z(\phi)}{V_p} + \frac{\phi}{V_p}Z\prime(\phi)\right) = \phi F_0\prime\prime(\phi) \tag{2.19}$$

which finally gives

$$\left(\frac{k_BT}{\phi V_p}(Z(\phi) + \phi Z\prime(\phi)) + \frac{\partial^2 W}{\partial \phi^2}\right)\nabla\phi = -\frac{\partial^2 W}{\partial\phi\partial(E^2)}\nabla(E^2). \tag{2.20}$$

In Equation 2.20, W indicates the total change in electrostatic energy in the presence of an electric field. For a non-conducting suspension, the electrostatic energy is

$$W = \frac{1}{2}\left(\varepsilon_s(\phi) - \varepsilon_m\right)E^2, \tag{2.21}$$

where ε_s depens on volume fraction. According to the Maxwell-Wagner model[25],

$$\varepsilon_s = \varepsilon_m\frac{1 + 2\phi\beta}{1 - \phi\beta} \tag{2.22}$$

where $\beta = (\varepsilon_p - \varepsilon_m)/(\varepsilon_p + 2\varepsilon_m)$ is the Clausius-Mossotti factor.

$$\frac{\partial^2 W}{\partial \phi^2} = \frac{E^2 \varepsilon_m 3\beta^2}{(1-\phi\beta)^3} \tag{2.23}$$

$$\frac{\partial^2 W}{\partial \phi \partial (E^2)} = \frac{1}{2}\frac{3\varepsilon_m \beta}{(1-\phi\beta)^2} \tag{2.24}$$

Substitution of the second derivatives of W in Equation 2.20 gives the final relation

$$\left(\frac{k_B T}{\phi V_p}(Z(\phi) + \phi Z\prime(\phi)) + \frac{E^2 \varepsilon_m 3\beta^2}{(1-\phi\beta)^2}\right)\nabla\phi = -\frac{1}{2}\frac{3\varepsilon_m\beta}{(1-\phi\beta)^2}\nabla(E^2). \tag{2.25}$$

From this Equation, we can numerically calculate the spatial particle distribution ϕ, once we have electric field profile E and the compressibility factor $Z(\phi)$. The compressibility factor is often calculated from the "equation of state"[26], which can be obtained from theoretical analyses or simulations. For the hard sphere system there are very precise expressions, such as Equation 2.26 by Carnahan and, Starling and Equation 2.27 for by Hall for a fluid phase[27,28].

$$Z(\phi) = \frac{1+\phi+\phi^2}{(1-\phi)^3} \tag{2.26}$$

$$Z(\phi) = \frac{1+\phi+\phi^2 - 0.67825\phi^3 - \phi^4 - 0.5\phi^5 + 3.2\phi^6}{1 - 3\phi + 3\phi^2 - 1.04305\phi^3} \tag{2.27}$$

Hall also constructed an expression for a crystal phase

$$\begin{aligned} Z_{FCC} = {} & \frac{12-3\psi}{\psi} + 2.557696 + 0.1253077\psi + 0.1762393\psi^2 \\ & - 1.053308\psi^3 + 2.818621\psi^4 - 2.921934\psi^5 + 1.118413\psi^6, \end{aligned} \tag{2.28}$$

with $\psi = 4(1-\phi/\phi_{max})$ and $\phi_{max} = 0.74$.

2.5.1 Equilibrium spatial distribution of particles

At equilibrium, the electrostatic energy is balanced by the chemical free energy of the colloidal suspension. Thus, we obtain a field-induced particle distribution in a single electric bottle device. Figure 2.9 shows the spatial distribution of the concentration of hard-sphere-like particles in a electrode-slit of an electric bottle at equilibrium. Here, the dielectric constant of the particles ($\epsilon_p \sim 2.6$) is higher than that of the suspending medium ($\epsilon_m \sim 2.3$), corresponding to positive dielectrophoresis. As shown in the figure, the particles are more concentrated near the electrode edge where the field is stronger, whereas the concentration is lower at the center region in which the field is low.

The charge-stabilized colloidal system used in this thesis is more closely described by a Yukawa potential[29]. Analytical expressions for the equation of state of these kinds of charged spheres are not available. Experimentally, we were able to obtain spatial distribution of the density of charge-stabilized soft spheres in a sample, which gives us a general picture of the concentration-dependent phase diagram. The suspension is composed of PMMA particles suspended in a mixture of solvents and additional surfactant AOT molecules. The details of this system will be described in next Chapter. The particles have repulsive interactions, so that they crystallize at lower volume fractions than the hard spheres. Figure 2.10 shows the concentration gradient in a single slit of an electric bottle.

2.5.2 Negative dielectrophoresis

Depending on the direction of the particle movement, we can distinguish two types of dielectrophoresis. The above equilibrium density gradient is induced by positive dielectrophoresis, where the particles are more concentrated at higher field strength. We can induce negative dielectrophoresis by changing the sign of Clausius-Mossotti factor in Equation 2.9. If we suspend

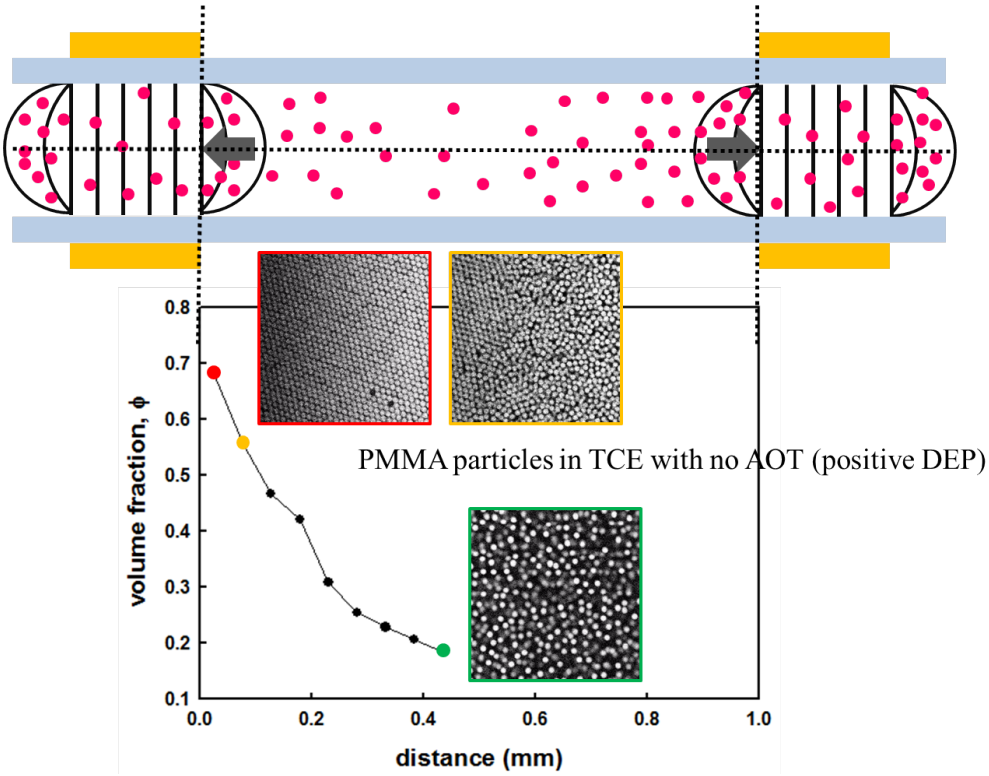

Figure 2.9: Spatial distribution of the density of the hard spheres along the electric field gradient. The images were taken in the center of the cell and the volume fraction of the hard spheres were measured by counting the number of particles by particle locating.

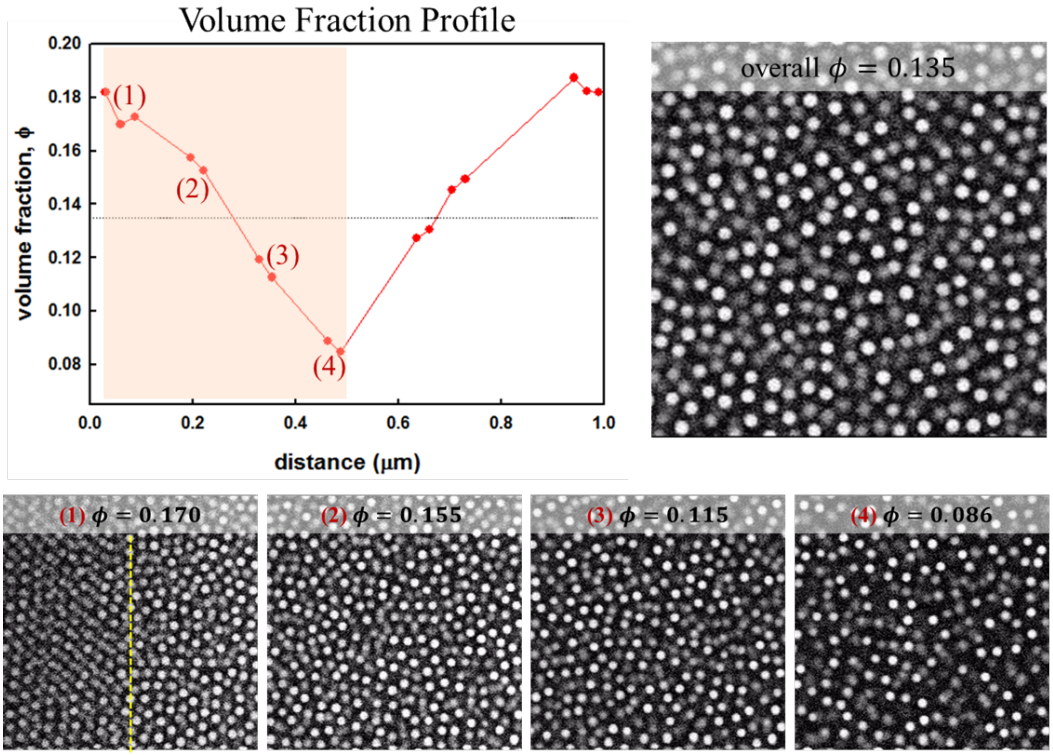

Figure 2.10: Spatial distribution of the density of soft spheres along the electric field gradient. Each image was taken in the center of the cell and the volume fractions of the soft spheres were measured by counting the number of particles from particle locating.

the PMMA particles of $\varepsilon_p = 2.6$ in a solvent with a higher dielectric constant, the particles experience negative dielectrophoresis. A solvent mixture that matches the density and refractive-index is a mixture of cyclohexyl bromide and *cis*-decalin, which has a dielectric constant of $\varepsilon_m \approx 6 \sim 7$.

With this solvent mixture, the particles concentrate in the regions of low electric field strength. Figure 2.11 shows the result. The confocal images were taken at the region indicated with green arrow, where the field strength is very low. As a result of balancing the electrostatic energy, the particle concentration increases and the particles which were initially in a liquid phase, crystallize after 90 minutes of compression.

Figure 2.12 gives a impression of a concentration gradient induced by an electric field. The numbers on the images correspond to the positions which are indicated with green arrows in the schematic figure of Figure 2.12 (a). Under the electric field, the particles are compressed in the center of the slit where the field is very low, whereas they are decompressed near the electrode where the strength of field is higher. Figure 2.13 shows a change of the density near the electrode as a function of time. The particles are continuously moving toward the region of low electric field, where the electrode is on the right side of each image.

In an electric bottle, melting or solidification can be driven by adjusting the electric field gradient. As soon as the electric field is switched off, the off-equilibrium system causes melting because the compressed crystal relax to the original fluid. Figure 2.14 shows the change of the concentration. all crystals have melted away 72 hours after switching electric field off.

2.6 Dielectrophoretic velocity

When the particles are exposed to a dielectrophoretic force, they move through a suspending medium with a certain velocity. This velocity depends on the field gradient and on the suspension's volume fraction. We estimated the terminal dielectrophoretic velocity of a particle in a

(a)

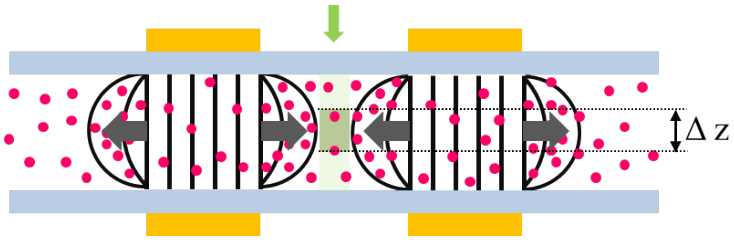

(b)

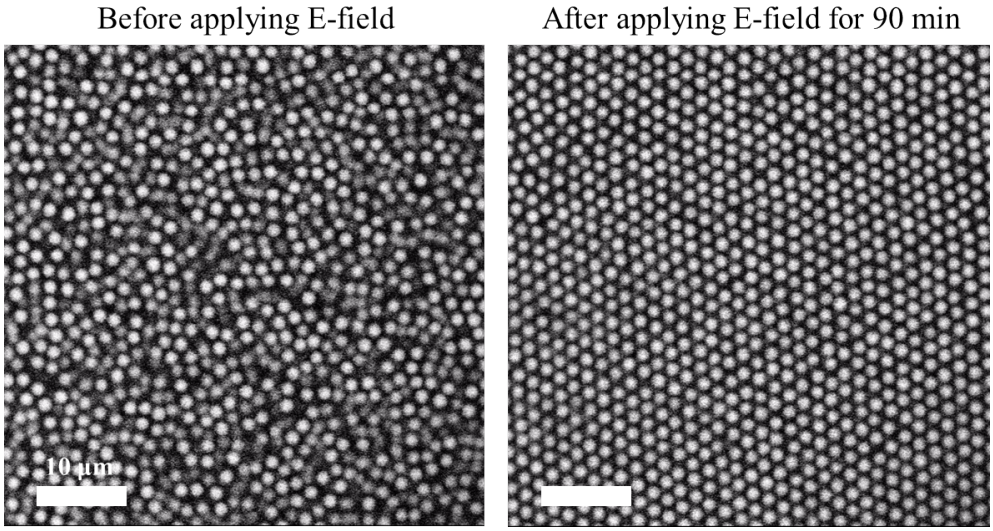

Figure 2.11: Crystallization after the dielectrophoretic compression (a) Schematic side view of an electric bottle with a scanning region indicated. (b) Structure change from liquid to crystalline, after applying an electric field for 90 minutes.

(a)

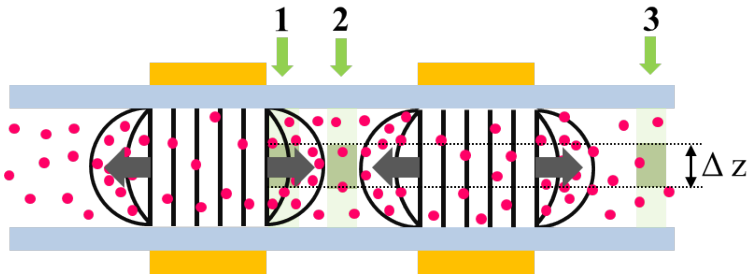

(b)

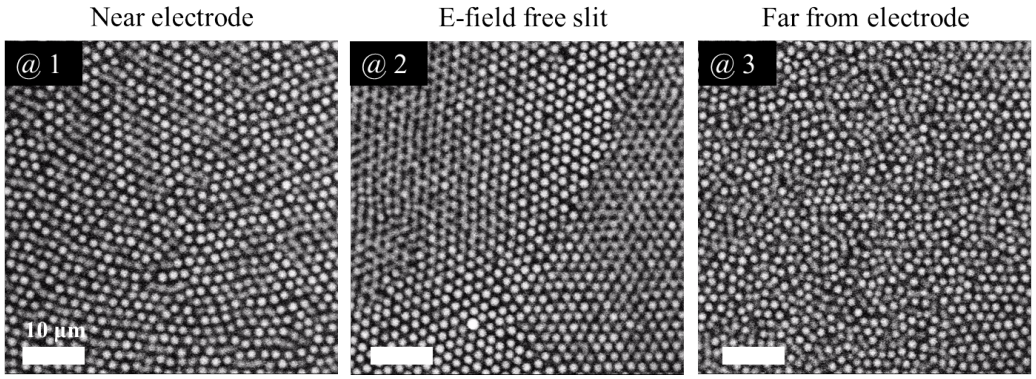

Figure 2.12: Spatial distribution of particles induced by negative dielectrophoresis (a) Schematic side view of an electric bottle with three scanning regions indicated. (b) Confocal images of colloids at each different regions.

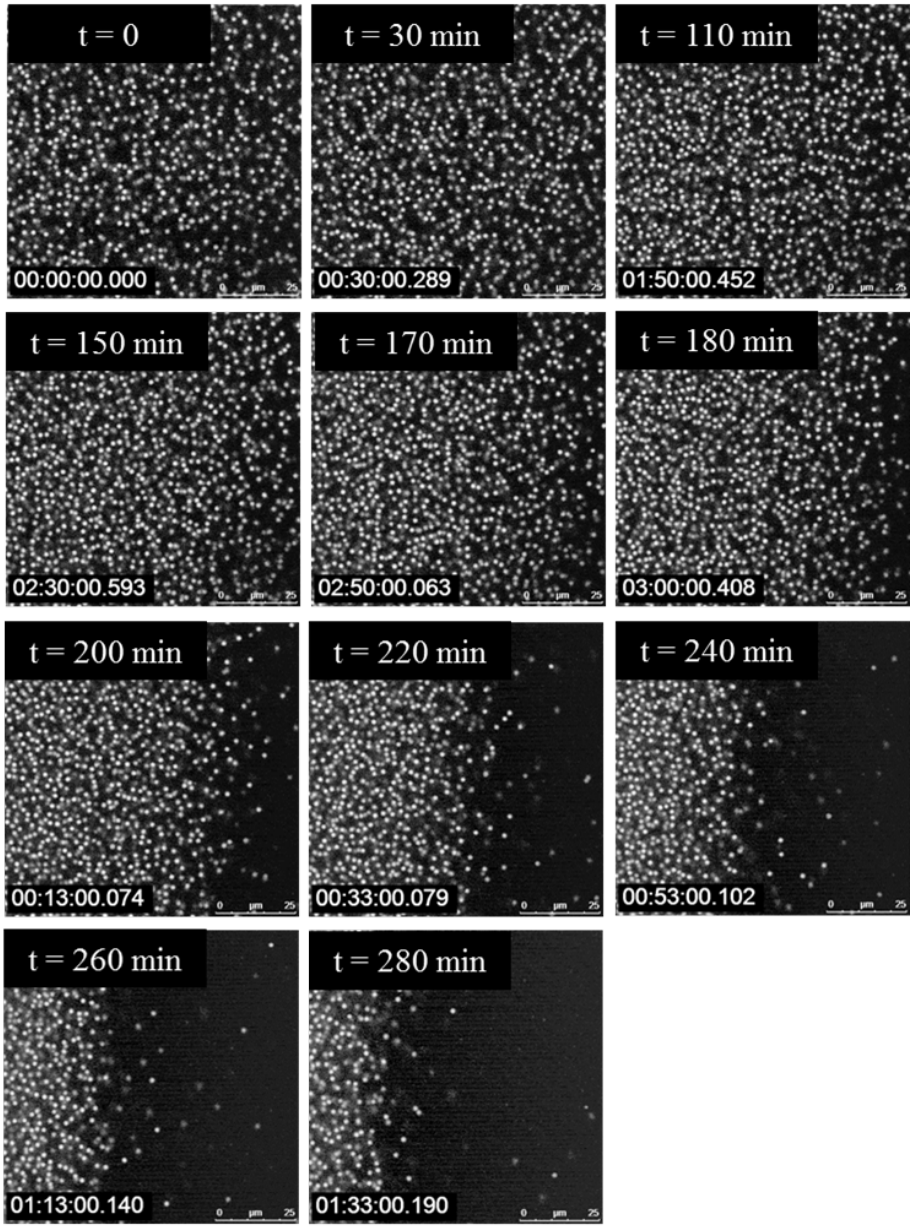

Figure 2.13: Movement of particles in time near a strong field gradient. Particles with lower polarizability are repelled away from the region of strong electric field over time.

(a)

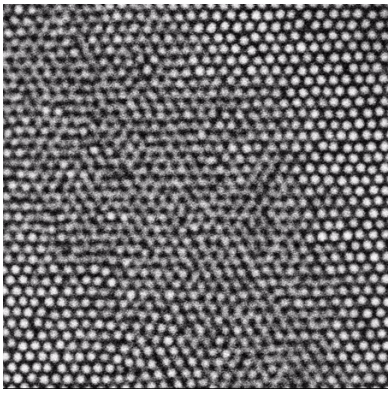

(b)

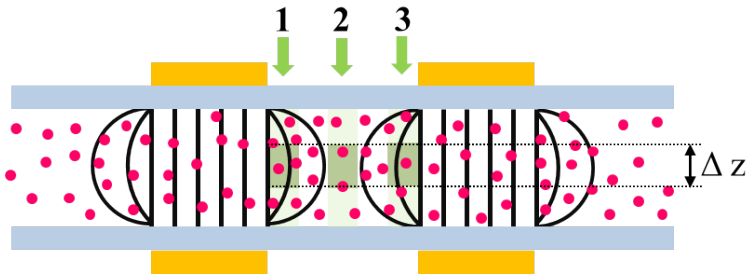

(c)

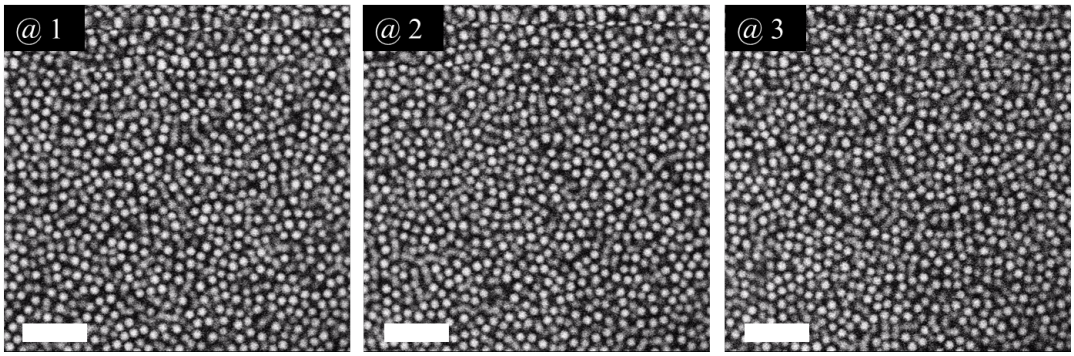

Figure 2.14: Melting in an electric bottle. (a) Crystals induced by a negative dielectrophoresis. (b) Schematic side view of an electric bottle with three scanning regions indicated. (c) The melt (fluid) phase 72 hours after turning off the electric field.

dilute solution by taking into account the Stokes drag[30]. In Figure 2.15, a particle is schematically shown with the two forces it experiences under terminal conditions. The drag force is determined by the viscosity η as described in Equation 2.1. In this solvent mixture of *cis*-decalin and cyclohexyl bromide, the viscosity is $\eta = 2.2\ mPa \cdot s$ as measured by a rheometer. Thus, the self-diffusion coefficient is $D = 1.17 \times 10^{-13}\ m^2/sec$. At the electric condition indicated with a red arrow in Figure 2.15 (b), the estimated velocity is

$$v_{DEP} = \frac{F_{DEP}}{6\pi\eta r} \sim 0.297 \mu m/sec, \tag{2.29}$$

where $F_{DEP} = -F_{Drag} = 6\pi\eta r v$. A velocity measurement by tracking a particle in an experimental system gives $v \sim 0.274\ \mu m/sec$, which closely correponds to that obtained from Equation 2.29.

(a)

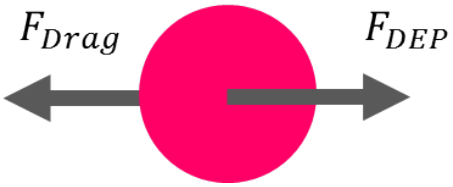

(b)

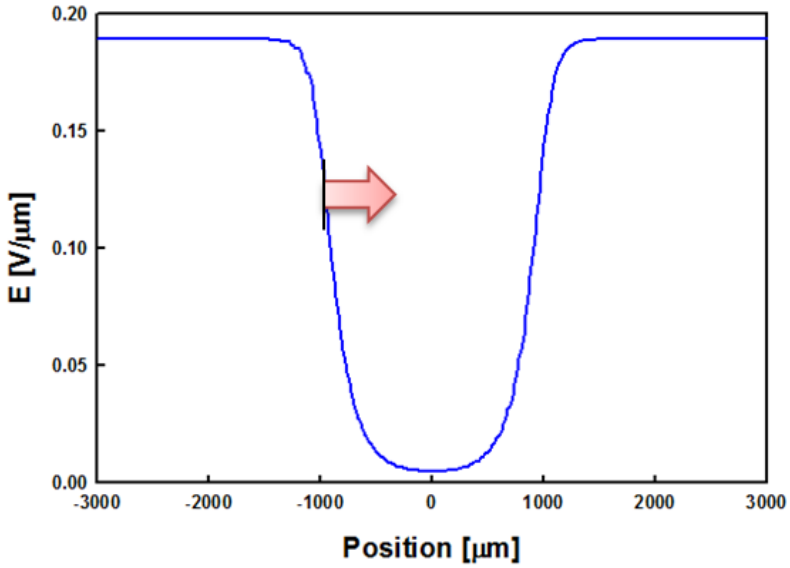

Figure 2.15: Dielectrophoretic velocity. (a) Calculated electric field profile at experimental electric condition, $V_{rms} = 56.6$ and $\omega = 1$ MHz. The red arrow indicates the position at which the particle's velocity measured. (b) A particle in a fluid experiencing dielectrophoretic force.

3

Experimental Setup and Analysis

This chapter describes the suspension characteristics, the experimental techniques for sample preparation, and the analysis methods.

3.1 Suspension preparation

Our experimental system is composed of fluorescently labeled $r \approx 1.8\ \mu m$ poly(methyl methacrylate)(PMMA) particles that are sterically stabilized with poly(hydroxystearic acid). The particles are suspended in a non-polar solvent that is a mixture of 40 $vol.\%$ decahydronaphtalene (*cis*-decalin) and 60 $vol.\%$ tetrachloroethylene (TCE). We chose these solvents to closely

Solvent	Refractive Index	Density[g/cm^{-3}]	Viscosity [cP]
TCE	1.505	1.623	0.890
cis-decalin	1.479	0.898	3.353

Table 3.1: Properties of the tetracholoroethylene (TCE) and *cis*-decalin solvents.

match the refractive index of the particles to minimize scattering in a confocal microscopy, as well as particle density to avoid sedimentation. A colloidal suspension in a mixture of the two solvents behaves as nearly hard-spheres.

3.1.1 Density matching

It is important to match the densities of the particles and the solvents to prevent the sedimentation. Even slight sedimentation can affect the crystal structures and dynamics of transitions, as has been observed in the crystallization in microgravity and normal gravity[13]. The density of the PMMA particles is $\sim$ 1.18 g/cm^{-3}, which is in-between the densities of the two solvents, as shown in Table 3.1. Although we can roughly estimate the volume required to match the densities from the rule of mixtures, adjustments are needed to reach the perfect match. Thus, we further add small amount of either solvent until we do not see any sedimentation. If the particles are creaming, we add *cis*-decalin which is less dense, and if the particles are sedimenting, we add TCE which is denser. We use the centrifuge to observe the sedimentation or creaming of particles.

Density matching is sensitive to temperature because the thermal expansion coefficients are different for solvents and particles[31]. The solvent has the larger thermal expansion coefficient. When the temperature increases, the solvent becomes less dense by expanding, which results in the solvent creaming. For this reason, we tried to set the temperature of centrifuge as close as possible to that of the observation and measurements.

3.1.2 Charge-stabilized colloids

Here, in this thesis, we used charge-stabilized colloidal suspensions which have repulsive interactions between particles. Adding dioctly sodium sulfosuccinate (often referred to as Aerosol OT or AOT) gives a repulsive interaction between particles. As mentioned in Section 2.3, AOT molecules form inverse micelles above a certain concentration ($\sim 10\ mM$). These act as charge carriers, and hence the particles have charge and the solvent has a conductivity. A schematic of inverse micelles formed in colloidal suspension is shown in Figure 3.1. The strength of interactions can be tuned by the amount of AOT molecules concentration, and the resulting repulsive interactions produce different type of crystals. Empirically, we often use the 5 mM and 15 $mM \sim 20\ mM$ AOT concentrations to produce the FCC and BCC crystals at high ϕ, respectively. At 5 mM, which is below the critical micelle concentration, the particles remain uncharged or slightly charged. When we match the density of the solvent with that of the charge-stabilized colloids, we first prepare all solvents in which a particular concentration of AOT molecules dissolved. Then, we go through the same steps in Section 3.1.1 by adding either solvents little by little until they are completely matched.

3.2 Sample cells: electric bottle

3.2.1 An electric bottle

We designed the electric bottle sample cell by developing the original idea from Chaikin's group for our experimental objection[16]. A schematic figure of an electric bottle is shown in Figure 3.2. It is composed of two coverslips ($22 \times 22\ mm^2$, No. 1 thickness) separated by two spacers (No. 0 thickness). The bottom plate is coated with transparent ITO (indium tin oxide) and the top plate has alternating 1 mm wide gold electrodes and electrode-free regions, as shown in Fig. 3.2. The transparent ITO electrode enables us to observe the changes under the electrodes,

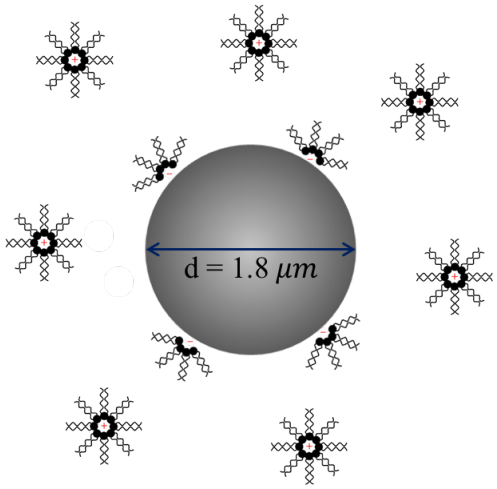

Figure 3.1: Inverse micelles in a suspension. AOT inverse micelles act as charging agents by charging the particle surface, as well as charge carriers by screening the surface charge

which is not possible with the opaque gold electrodes of the original Chaikin design. For the electrodes on the top plate, we used scotch tape to define the exposed and unexposed areas and deposited 30 *nm* gold using a sputter coater. The whole sample cell of the two cover slips with electrodes and the spacers was fixed on a 1 *mm* thick glass slide for mechanical stability. We glued every part with a UV-curing optical adhesive (Norland No. 68). Then, we filled the sample cell with the colloidal suspension and completely sealed it using epoxy glue. When flowing the suspension, we tried to exclude bubbles and dusts by flowing the suspension carefully using capillary forces and keeping the sample cells in a clean area. To make electrical contacts on the electrodes of the top and bottom plates, we used silver paste and thin thermocouple wire, and soldered it with a low melting temperature solder. Silver paste makes better adhesion with the solder. Figure 3.3 shows an example of an electric bottle cell with gold electrodes and slits.

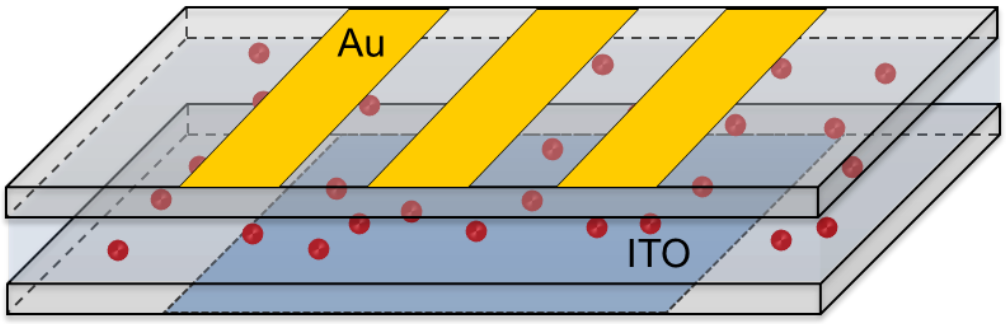

Figure 3.2: Schematic diagram of an “electric bottle” to manipulate colloid densities by the electric field gradients.

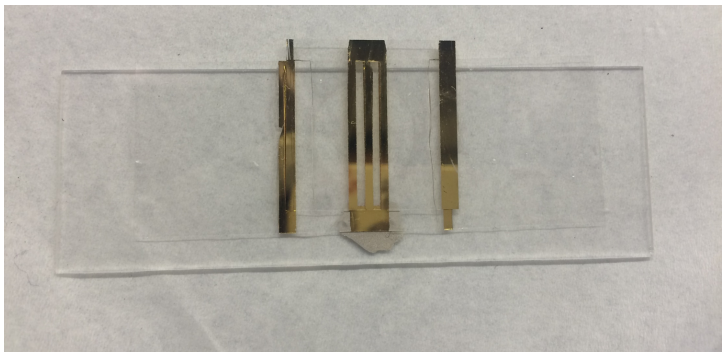

Figure 3.3: Electric bottle sample cell. The sample cell is assembled on a glass slide for a mechanical stability.

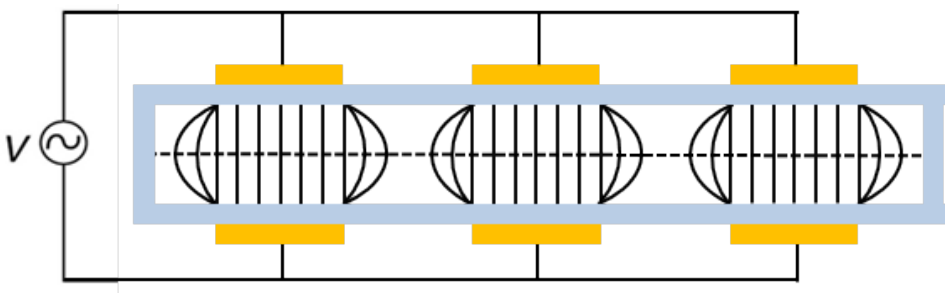

Figure 3.4: A schematic side view of an electric bottle with a contour line of an electric field. A fringe-like lines represent the inhomogeneous field.

3.2.2 Electric field

To achieve the high voltage and high frequency at the same time, we used a function generator and connected with voltage amplifier. The function generator is 10 MHz waveform generator (Agilent 33210A), and the amplifier is DC-3 MHz, 50 W amplifier which is designed by Winfield Hill in Rowland Institute. We connected the two output channels with an oscilloscope to check electric fields.

3.2.3 Details about the experimental system

The electrode design of a sample cell in Figure 3.3 produces alternating uniform and non-uniform electric fields. Figure 3.4 shows a schematic of the electric field lines in a side view of the cell. Figure 3.5 (a) shows an electric field profile calculated using a COMSOL in the midplane of the cell as shown by the dotted lines in Figure 3.4. The calculations are for the two different electrical conditions, which we used experimentally 60 V, 80 V and $\omega = 1$ MHz. There is a steep electric field gradient near each electrode edge, where we expect dielectrophoresis.

The dielectric constants for most of the colloidal suspension which were mostly used in this system are $\varepsilon_p = 2.6$ for the PMMA particles and $\varepsilon_m = 2.3$ for the solvent mixture. The contrast of the dielectric constants makes the particles experience the positive dielectrophoresis. Since

(a)

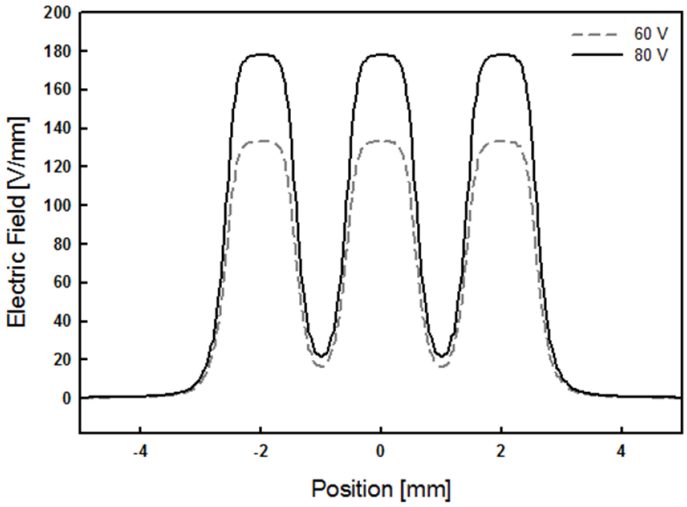

(b)

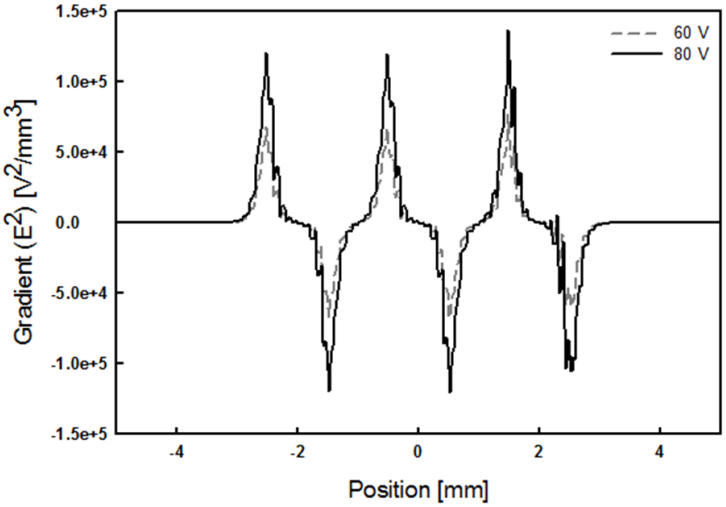

Figure 3.5: (a) Calculated electric field profiles for two experimentally applied voltages. (b) Gradient of squared electric fields.

an AC electric field is applied, the dielectrophoresis works for the charged-colloidal suspension, as well.

3.3 Confocal measurements

A confocal microscope allows us to track the particles in three dimensions and in time. The microscope used in most experiments is a Leica SP5 confocal laser-scanning microscope, usually in the resonant mode, which is the fast scanning mode option. We choose a laser depending on the excitation spectra of fluorescent dye in the particles. For single species of particles, a 543 *nm* helium-neon laser was used. For two-component system, we used two lasers. The microscope gives three dimension information by reconstructing all two dimensional images. An image of a single plane is an XY slice, and a series of XY slices in Z direction produces an XYZ stack. To know the evolution of transitions or equilibrium, series of XYZ stacks were taken over time.

A 63$\times$ glycerol Objective was used, which has a long working distance. Each single image of 512 $\times$ 512 pixels in XY was taken along regular distances in the Z direction. Measurements were made near the center plane of the cell to exclude effects from the glass surface. Before a microscope observation, we let the sample cells equilibrate for several days.

3.4 Particle locating

The first analysis step is to obtain the locations of the particle centers from the three-dimensional confocal image stacks. Particle locating algorithms and image processing are central to colloidal physics field and are being improved continuously. The algorithm we used in this thesis was originally written by Maria Kilfoil and further developed by Katharine Jensen, who added an interative method[32,33]. The algorithm removes the short wavelength noise and subtracts the background to define a clear particle signal. Then, it identifies the centers of remaining bright

spots, which gives the particle location information.

Figure 3.6 shows an example. The location of the center of each particle is marked with cross in Figure 3.6 (b). By obtaining the location information of an image stack, we can reconstruct and the 3D structure of colloidal suspension as shown in Figure 3.7.

3.5 Particle tracking

After obtaining the particle location information, we link these locations with a particle tracking code. The code was written by Katharine Jensen and further developed by Emily Russel. The algorithm looks for the particle at timestep (t) closest to a particle at the previous timestep ($t-1$). The largest distance to be considered must be within a particle diameter to allow tracking. While the trackable individual particles are assigned with an identification number, some untrackable particles are identified as "lost" particles and are assigned with no identification number. For the data that needs to be tracked in time, we set the imaging condition to have a fast scanning speed.

3.6 Structure analysis: Bond orientation order parameter

In studies of phase transformations, it is important to distinguish the two phases by their structure. We distinguish the crystalline phase from the liquid by assigning a bond orientation order parameter ϕ_i to individual particles[34].

We first define nearest neighbor particles (j) whose distances from center particles (i) are within a range of ${r_{ij}}^2 < 3{r_0}^2$ where r_0 is a minimum distance from the center atom. Then, we compute the bond angles θ between all of the nearest neighbor particle pairs.

The order parameter is defined as the number of in-line nearest neighbors: the number of 180° angles $cos\theta = 1$. However, in real systems, defects in the bulk crystals, such as vacancies,

(a)

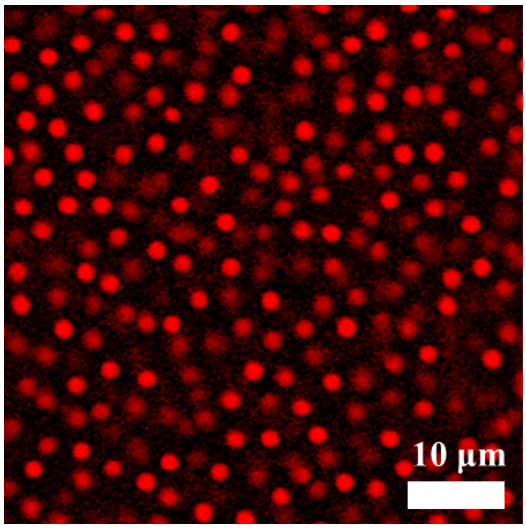

(b)

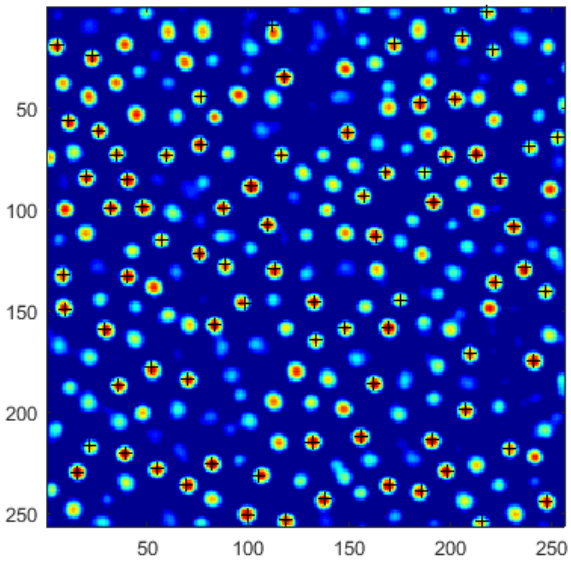

Figure 3.6: Particle locating in a confocal microscope image. (a) A confocal image of a fluorescently-dyed colloidal suspension. (b) Particle locations marked with cross correspond to the particles in a confocal image (a).

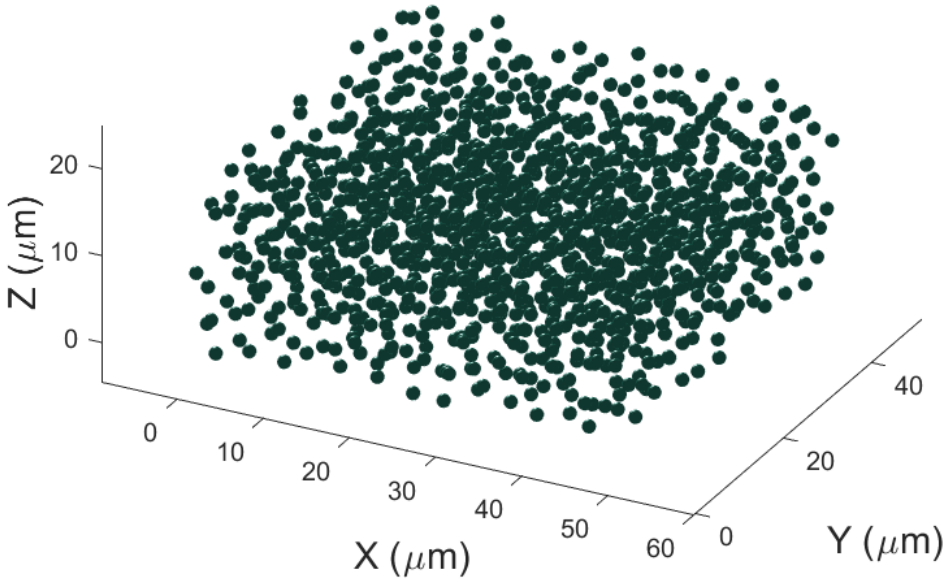

Figure 3.7: Reconstucted 3D structure of a colloidal suspension.

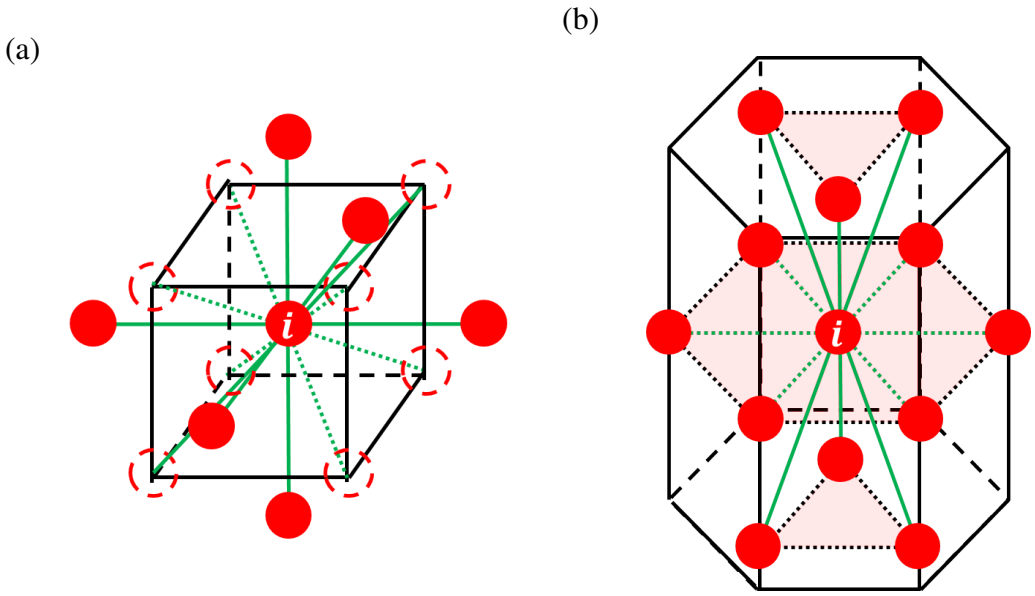

Figure 3.8: a) Body-centered cubic crystal structure. b) Face-centered cubic crystal structure.

will produce a low local order parameter, which will complicate the distinction between bulk crystal and liquid. We, therefore, use average order parameters $< \phi_i >$, which are averaged over center atom and its neighbors. Then, each particle is assigned with the average order parameter. Figure 3.8 shows the BCC and FCC crystal structure with in-line nearest pairs. The highest order parameter that a perfect crystal can have is 7 for BCC for 14 near neighbors (8 from nearest neighbors and 6 from next nearest neighbors) and 6 for FCC within 12 nearest neighbors.

Figure 3.9 (a) and (b) are snapshots of crystal-liquid interface of a BCC and a FCC crystal, respectively. The orientation of the crystals in the confocal image planes are (110) for BCC and (111) for FCC. The crystals always formed with these orientations parallel to the glass surface, probably due to surface effects, since these are the densest planes in each crystal structure. The projected images at the bottom are whole particles colored with their assigned order parameters. The region with an ordered structure has more yellow particles which have a high order

parameter.

While most crystalline particles are assigned higher average order parameters, the particles in the liquid region are assigned lower order parameters. The order parameters decrease gradually near the interface toward the liquid. We can distinguish the crystalline phase from liquid phase by choosing a threshold order parameter that is between those of crystal and liquid. We classified the particles into crystalline or liquid according to their assigned order parameters. Particles with $\phi_{i-BCC} > 3.5,\ \phi_{i-FCC} > 3$ are defined as crystalline, and the others as liquid. Figure 3.10 shows the crystalline particles in a two-phase FCC-liquid system. Although these particular order parameters distinguish well between crystalline and liquid, defects in the crystal and coincidental crystal-like structures in the liquid can blur the distinction.

In order to solve this problem, we introduced another parameter Z_i which counts the number of crystal neighbors of a crystal particle. Among the crystalline particles which we already distinguished by threshold order parameter, we count the number of crystalline neighbors. Figure 3.11 shows the FCC crystalline particles clarified by their number of crystalline neighbors. In the bulk crystal, far from the edges or interface, most of the particles have 12 nearest crystal neighbors ($Z_i = 12$), whereas the particles have fewer crystal neighbors toward the interface or edge.

We can use this approach to identify attachment/detachment of particles during the transformation process in Chapter 4, and at an equilibrated interface in Chapter 5 and 6. The details of identifying those particles will be explained in each chapter.

(a)

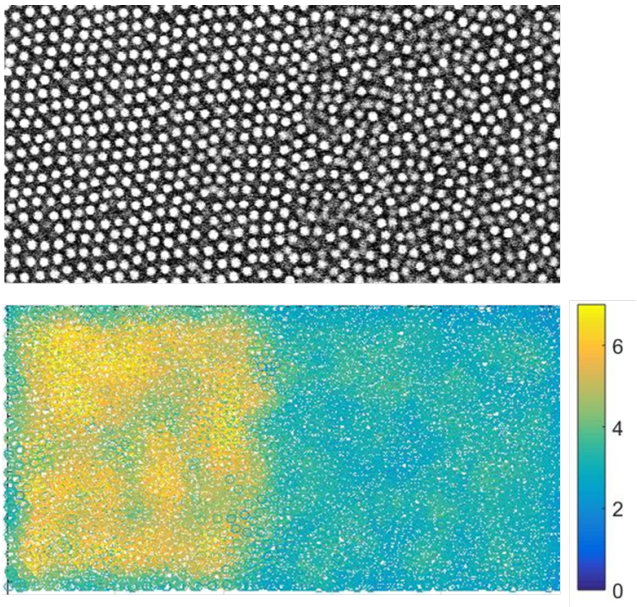

(b)

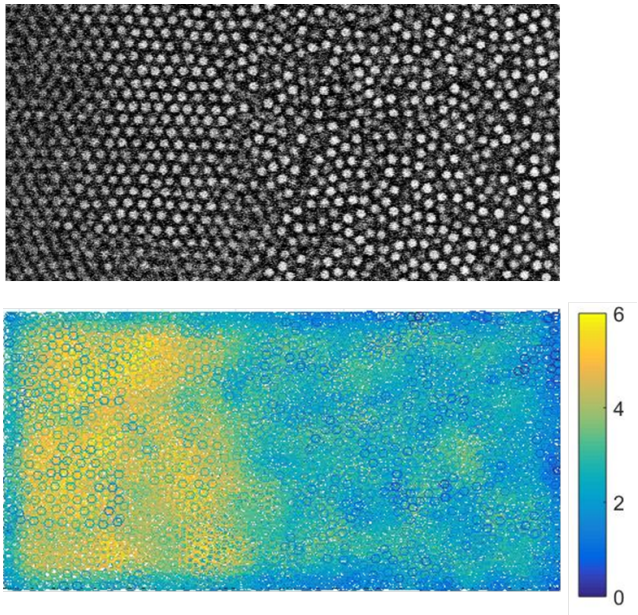

Figure 3.9: BCC crystal-liquid interface (top) and images of the particles colored with their order parameters (bottom). b) FCC crystal-liquid interface (top) and images of the particles colored with their order parameters (bottom).

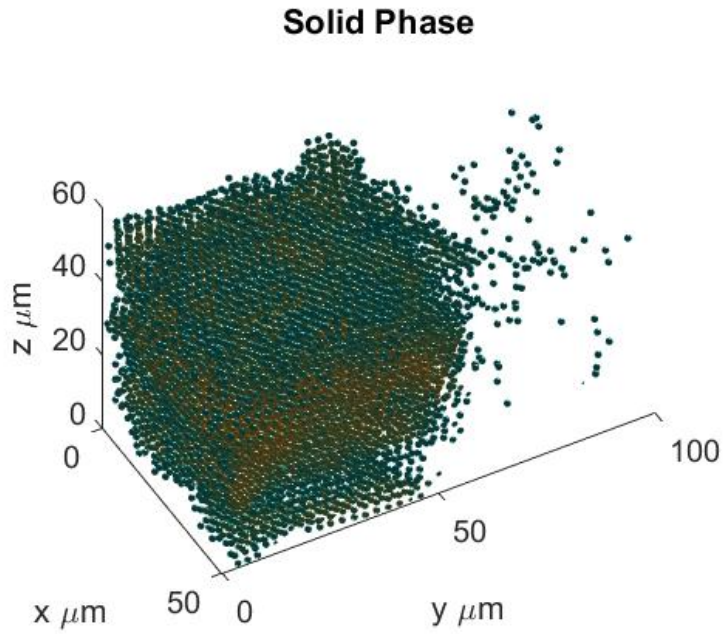

Figure 3.10: FCC crystalline particles in a two-phase crystal-liquid system distinguished by only threshold order parameter. Crystalline particles are colored with the number of crystal neighbors, Z_i.

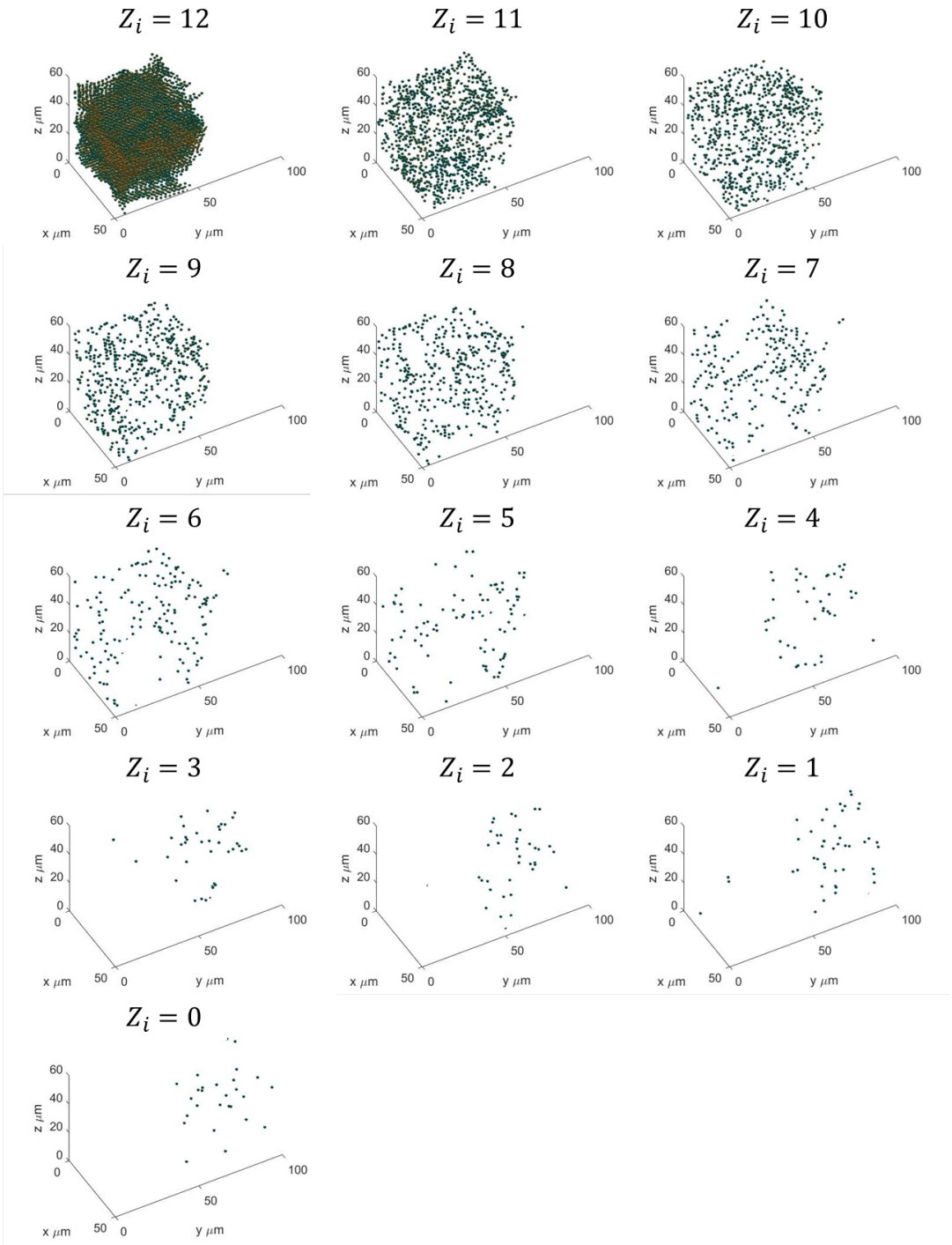

Figure 3.11: FCC crystalline particles identified by the number of their nearest crystal neighbors, Z_i

4

Results: A direct observation of crystallization and melting

In this chapter, we study the kinetics of crystal growth and melting of two types of colloidal crystals, body-centered cubic (BCC) crystals and face-centered cubic (FCC) crystals. An electric bottle system allows us to control the particle concentration, which further allows a real-time manipulation of the growth and melting. We were able to measure the attachment and detachment rates at the interface during the transformation processes. This provides a detailed view of the random-walk-

4.1 Introduction

Crystallization and melting of atomic crystals are fundamental transformations from one phase to another phase toward the thermodynamically most stable form. The free energy difference between two phases drives the transformations and they involve a transfer of atoms going forward and backward across an interface. While the net transfer of atoms results in the crystal either growing or melting, the kinetics of the the growth depends on the atomic movements[35]. The jump frequency k of an atom in a simply activated process can be written as

$$k = \Gamma exp\left(-\frac{\Delta G^*}{k_B T}\right), \tag{4.1}$$

in which Γ is an attempt frequency and ΔG^* is an activation energy. In some cases, especially monatomic systems such as metals or liquid gases, the mechanism is thought to be collision-limited, which corresponds to the absence of an activation barrier, $\Delta G^* \approx 0$ and hence $k = \Gamma$ [6,36]. Experimental evidents for this type of growth are measurements of the growth speed as a function of velocity. The detailed mechanism, however, for obvious reasons, has never been directly observed. A related question is the symmetry or lack thereof between the melting and freezing kinetics[37]. Again, direct observation can be very revealing.

4.2 Experimental details

The colloidal suspension consists of $r \approx 1.8\ \mu m$ polymethyl(methacrylate) particles sterically stabilized with poly(hydroxystearic acid). The particles are suspended in a non-polar solvent that is a mixture of 40 $vol.\%$ decahydronaphtalene (*cis*-decalin) and 60 $vol.\%$ tetrachloroethylene (TCE) as mentioned in Section 3.1. In this experiment, we used two kinds of colloidal suspen-

sions to produce two types of crystals resulting from the different interactions. The interaction between particles was repulsive as a result of the addtion of dioctyl sodium sulfoccinate (often referred to as Aerosol OT or AOT)[21]. An AOT concentration of 15 *mM* gives long range repulsive interactions between particles, whereas a concentration of 5 *mM* results in slightly charged spheres. We match the density of the particles with the solvent by using repeated centrifugation until no sedimentation is observed.

We used the electric bottle cell shown in Figure 3.2. It consists of alternating 1 *mm* wide gold electrodes and electrode-free regions on the top plate and a continuous ITO electrode at the bottom plate, which produce electric fields as depicted in Figure 3.5. It shows the calculated electric field profile in the horizontal center plane between the plates at 60 *V* and 80 *V*, $\omega = 1$ *MHz*. The ITO electrode is transparent, which enabled us to observe the density change under the electrode, which is not possible with the opaque gold electrodes.

The PMMA colloidal particles are more polarizable ($\varepsilon_p = 2.6$) than the suspending medium ($\varepsilon_m = 2.3$), so that the particles move toward stronger electric field. We first let the colloidal suspension reach the dielectrophoretic equilibrium by applying an electric field for two days. We then we start measurements at the crystal-melt interface that formed near the electrode edge. As described in Section 2.5.2, dielectrophoretic compression initiates the crystal nucleation and the crystal growth, starting from the electrodes, and melting starts when we switch off the electric field, as an action of relaxing to the original fluid phase.

With the real-time manipulation of the particle concentration in the electric bottle and the use of confocal microscopy, we are able to visualize the growth process in three dimensions at the single particle level. Images $100 \times 50 \times 40$ μm^3 ($512 \times 512 \times 161$ pixels) in size were taken every 4 seconds near the middle of the cell to exclude possible effects of the glass surface, and the individual particles were tracked in time and space.

4.3 Results and discussion

4.3.1 Spatial concentration distribution of particles

Dielectrophoretic equilibrium produces a particle concentration gradient in a single electric bottle. The spatial distribution of particles in the 15 mM and 5 mM AOT suspensions are shown in Figure 4.1 (a) and (b), respectively. We took images every 100 μm across the entire length of the cell. The number density η was measured by counting the number of particles obtained from the particle location image analysis[32]. The reconstructed 3D images were analyzed to give particle location information with a resolution of 0.03 μm in the x and y directions and 0.1 μm in the z direction. The initial uniform number densities of the 15 mM and 5 mM suspensions are $\eta_0 = 0.032\ \mu m^{-3}$ and $\eta_0 = 0.050\ \mu m^{-3}$, respectively. The density increases in the strong electric field region during the dielectrophoretic compression, resulting in the formation of crystals at higher densities; body-centered cubic (BCC) crystals are formed in the 15 mM suspension at $\eta = 0.036\ \mu m^{-3}$, and face-centered cubic (FCC) crystals are formed in the 5 mM suspension at $\eta = 0.054\ \mu m^{-3}$. In the latter, crystallization occurs at a volume fraction of 0.29, much lower than the 0.494 in the case of hard spheres. This illustrates the effect of the softer potential[10]. Figure 4.2 show the equilibrated crystal-liquid interfaces of the BCC and FCC crystals, respectively.

4.3.2 Identification of attachment and detachment

Figure 4.3 shows three-dimensional reconstructions of the crystalline and liquid phases. We identify the crystal and liquid phases by assigning an order parameter ϕ_i to each particle. More details about the order parameter were given in Section 3.6. Recall that we classify the particles with $\phi_{i-BCC} > 3.5, \phi_{i-FCC} > 3$ as crystal and all others as liquid. In Figure 4.3, we use yellow spheres to indicate the crystalline and blue spheres to indicate the liquid. The successive images show how the BCC crystals grow during dielectrophoretic compression, until the equilibrium is

(a)

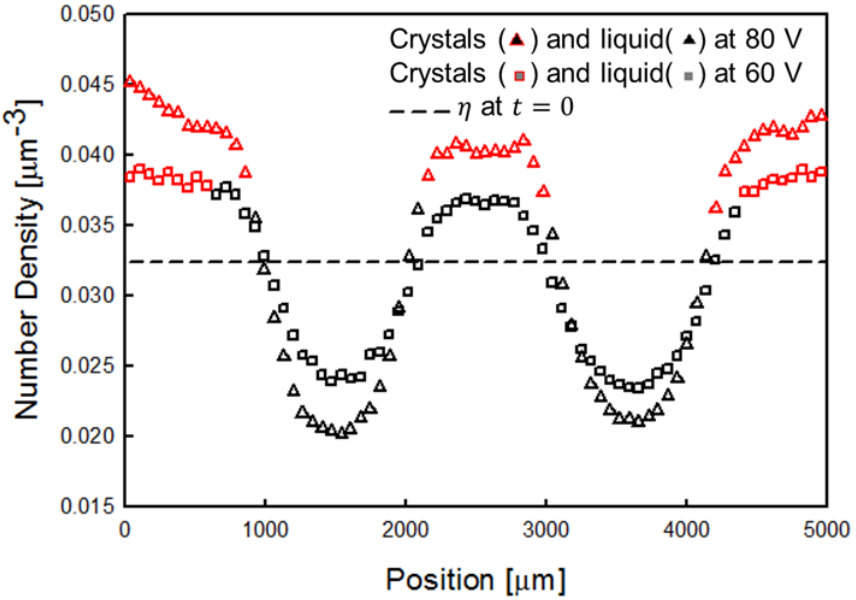

(b)

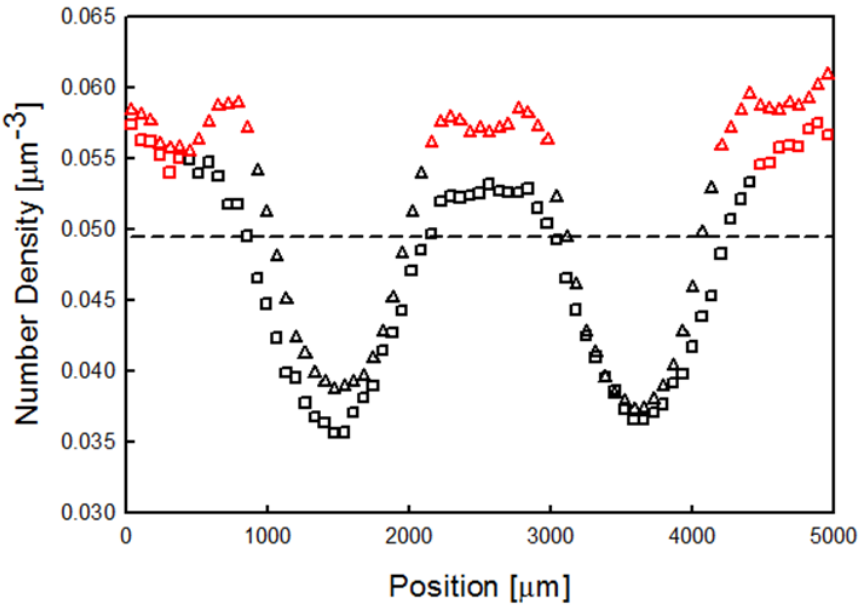

Figure 4.1: Spatial particle concentration profiles at dielectrophoretic equilibrium where the red dots correspond to the crystalline phase. (a) 15 *mM* AOT suspension forms BCC crystals. (b) 5 *mM* AOT suspension forms FCC crystals.

(a)

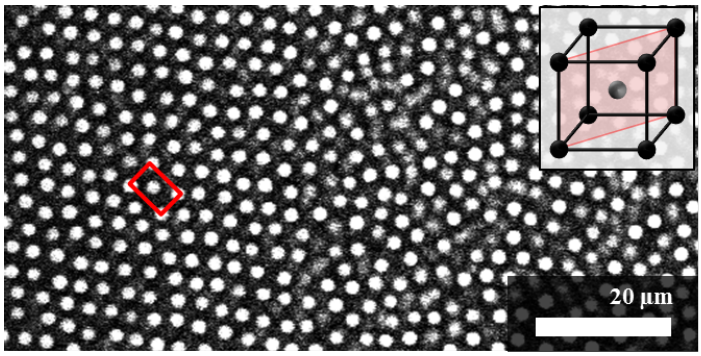

(b)

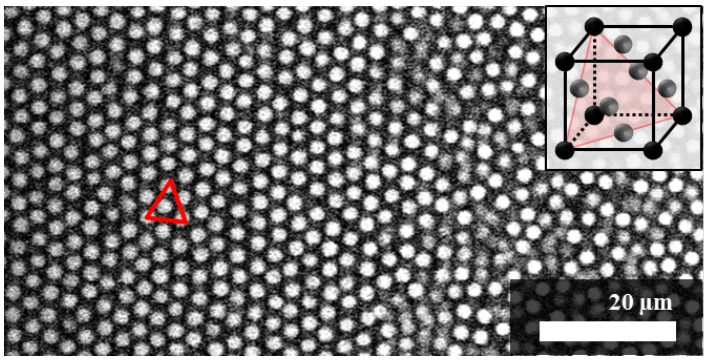

Figure 4.2: Confocal images of a crystal-liquid interface for (a) BCC and (b) FCC crystals, taken at the center of the electric bottle cell.

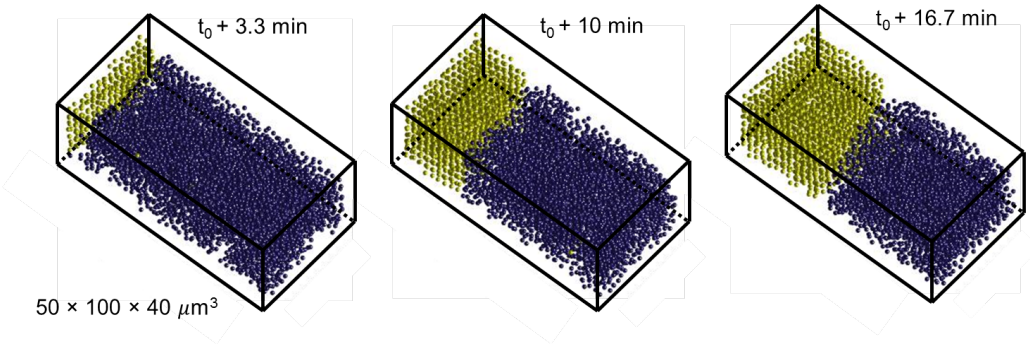

Figure 4.3: Crystal growth on the particle scale. Reconstructed images of crystallization, where the yellow spheres are crystalline and the blue spheres are liquid.

reached.

The tracking of the particles allows us to determine the rates at which particles attach to or detach from the interface, which are denoted by jump frequencies, k^+ and k^-, both in equilibrium and out of equilibrium. A schematic diagram of the attachment and detachment that occur at the crystal-liquid interface is shown in Figure 4.4. To identify the attaching and detaching particles, we used an additional parameter, Z_i, the number of crystal neighbors which is described in Section 3.6, but, assigned to the particles in all regions (crystal, interface, or liquid). The number of crystal particles that surrounds a particle, Z_i, depends on the region to which (crystal, interface, or liquid) the particle belongs. When the particles make jumps to attach to or detach from the interface, the number of its crystal bonds changes. Liquid particles which has low Z_i are categorized into two groups "interfacial" with $Z_{i-BCC} = 3 \sim 6, Z_{i-FCC} = 2 \sim 4$ and "liquid-like" with $Z_{i-BCC} = 0 \sim 2, Z_{i-FCC} = 0 \sim 1$. A change from liquid-like to interfacial at successive time points signifies attachment, and conversely a change from interfacial to liquid-like signifies detachment. Also, if a particle is stationary at the interface, it is defined as an interface particle. Figure 4.5 visualizes the attachment, detachment, and interface particles at equilibrium, which are represented with red, blue, and green spheres, respectively.

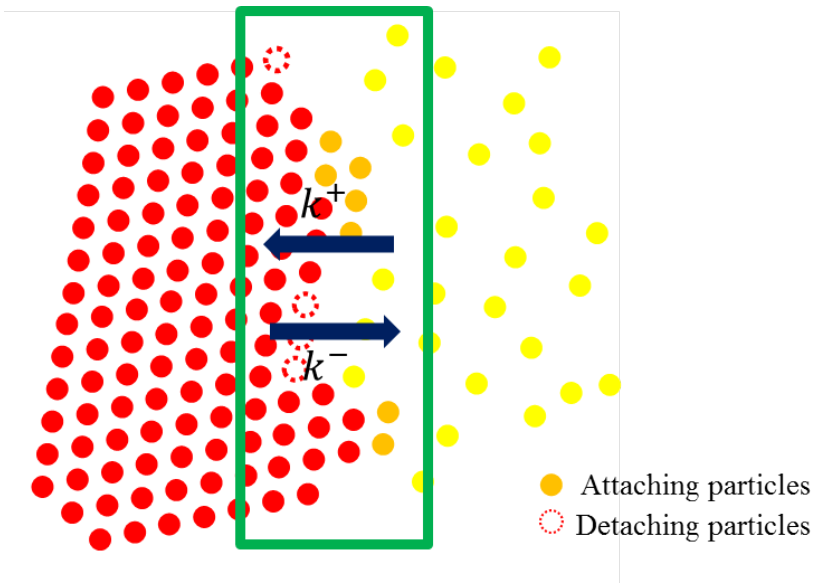

Figure 4.4: A schematic diagram of attachment and detachment at the crystal-liquid interface.

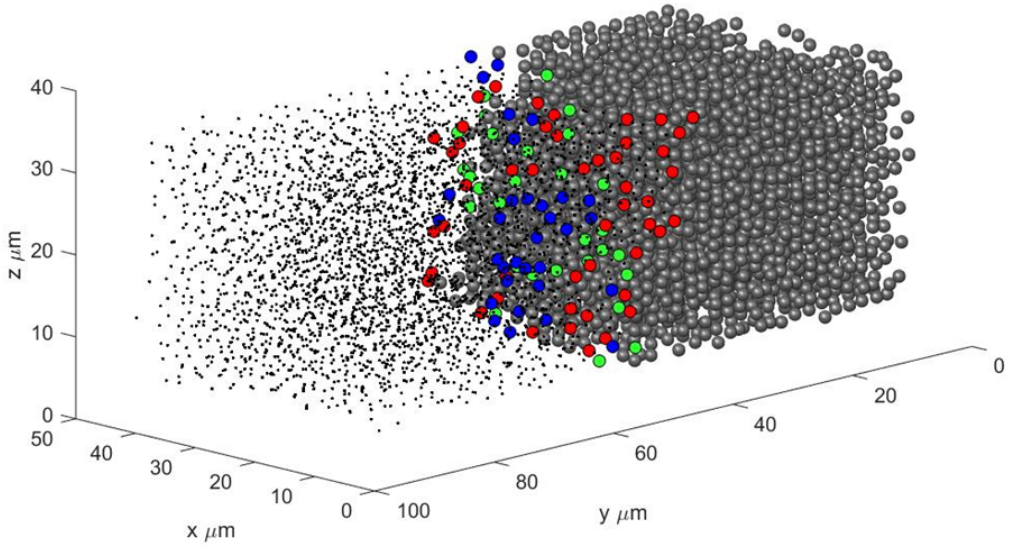

Figure 4.5: Identification of attachment and detachment at an interface. Red and blue correspond to attachment and detachment particles, respectively and green correspond to interface particles.

Jump rate $[sec \cdot particle]$	Equilibrium		Growth		Melting	
	k^+	k^-	k^+	k^-	k^+	k^-
BCC crystals	0.0716	0.0714	0.0753	0.0728	0.0797	0.0827
FCC crystals	0.0750	0.0750	0.0711	0.0682	0.070	0.0734

Table 4.1: Average jump rates of attachment/detachment particles at the interfaces.

The jump frequencies are obtained by counting the total number of attachment and detachment events in a time interval of 4 sec, and dividing by the time and the number of potential sites of the interface. The potential sites are the places where the arrival of a particle would turn it into a crystalline one. The results are listed in Table 4.1. The fluxes of attaching and detaching particles at equilibrium are equal ($k^+ = k^-$), while for crystallization $k^+ > k^-$ and for melting $k^- > k^+$. The average jump distances λ for attachment and detachment are 0.83 ± 0.03 μm and 0.76 ± 0.04 μm for BCC and FCC, respectively. The imaging interval of $4sec$ is sufficiently short for each observation of a jump to represent a single event.

4.3.3 Mean square displacements

To establish the attempt frequency Γ, we investigated the Brownian motion of the particles in the crystal, interface, and liquid at equilibrium. We calculated the mean square displacement $\langle \Delta r^2 \rangle$ which indicates the distance Δr traveled by a particle over a given period time Δt[38].

$$\langle \Delta r^2 \rangle = \langle (r(t + \Delta t) - r(t))^2 \rangle \tag{4.2}$$

In the crystal, interface, and liquid, the particles travel different distances, as the volume fractions of each region are different. Figure 4.6 (a) and (b) show the mean square displacements

$\langle \Delta r^2 \rangle = 6Dt$		Crystalline	Interface	Liquid
BCC crystals	$\langle \Delta r^2 \rangle [\mu m^2]$	0.57	0.64	0.86
	$D[\mu m^2/sec]$	0.024	0.027	0.036
FCC crystals	$\langle \Delta r^2 \rangle [\mu m^2]$	0.39	0.58	0.82
	$D[\mu m^2/sec]$	0.016	0.024	0.034

Table 4.2: Diffusion coefficients of particles at equilibrium calculated from the mean squared displacements in the crystal, interface, and liquid. The mean square displacement $\langle r^2 \rangle$ is for $\Delta t = 4$ *sec*

of the particles at the three regions in BCC and FCC. In the liquid phase, the quantity increases linearly with time. However, in the crystal or at the crystal-liquid interface, the particles are caged and diffuse only a short distance within the cage. This results in an limited increase of the mean square displacements and a transition to a plateau.

The diffusion coefficient D which is a measure of the speed of a diffusing object, can be computed from the mean square displacement with Equation 4.3. The results are listed in Table 4.2. The diffusion coefficient in the crystal is that for caged displacements, and not the one for vacancy diffusion of the particles, through the lattice.

$$\langle r^2 \rangle = 6Dt \tag{4.3}$$

The attempt frequency can be estimated by considering the one-dimensional diffusion jump frequency in Equation 4.4, using the mean used values of D and λ[39]. This gives $\Gamma_{BCC} = 0.078\ sec^{-1}$ and $\Gamma_{FCC} = 0.083\ sec^{-1}$ for BCC and FCC, respectively. We note that k and Γ have similar values. In other words, thermally-driven Brownian motion sets the upper limit of the attachment kinetics, therefore the process is limited by the random walk. This is equivalent

(a)

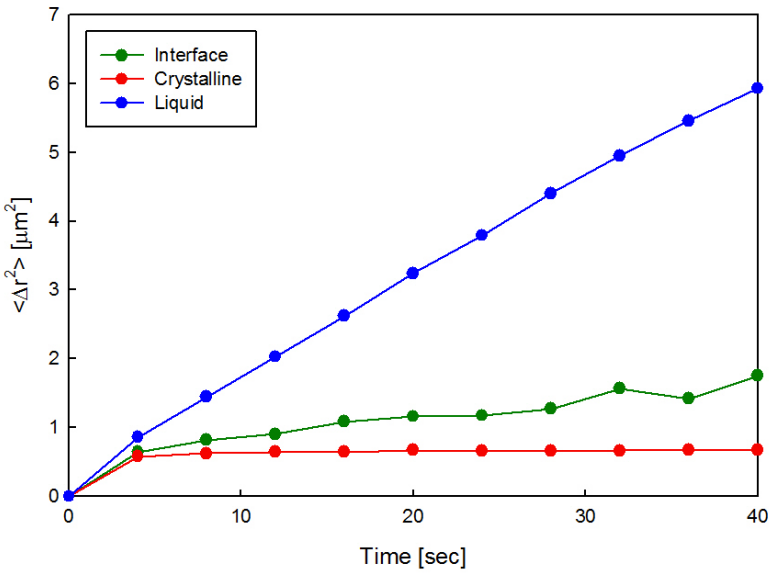

(b)

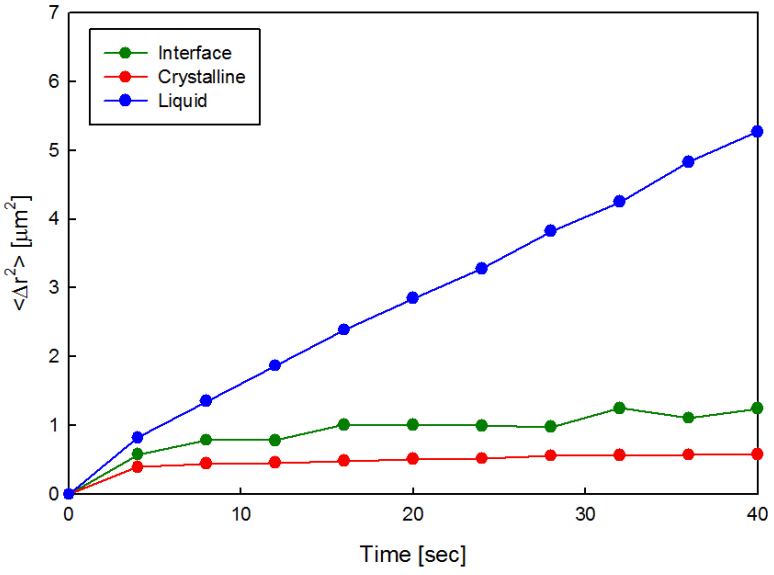

Figure 4.6: Mean square displacements in the crystal, interface, and liquid at equilibrium for (a) BCC and (b) FCC. Green, red, and blue lines correspond to interface, crystal, and liquid, respectively.

to collision-limited growth in atomic systems where ΔG^* becomes zero[40].

$$\Gamma = \frac{2D}{\lambda^2} \tag{4.4}$$

4.3.4 Biased random walk

During growth or melting, the random walk is biased by the free energy difference ΔG between two phases. The effect of the bias can be estimated in the following one - dimensional analysis[41].

Between collisions, a particle with a mass m has a Brownian velocity in one dimension

$$v_B = \frac{\lambda}{\tau}, \tag{4.5}$$

where λ is a jump distance and τ is a jump time. This velocity is related to the mass m

$$m = \frac{k_B T}{v_B^2} = \frac{k_B T \tau^2}{\lambda^2}, \tag{4.6}$$

by applying the equipartition principle to one component of the kinetic energy

$$\frac{k_B T}{2} = \frac{m v_x^2}{2}. \tag{4.7}$$

The phase transformation is driven by a difference in chemical potential, ΔG, caused by the concentration gradient produced by the dielectrophoretic forces. The driving force is the gradient of the chemical potential $F_x = \Delta G/\lambda$. The drift velocity in response to this driving force is, according to Newton's third law,

$$v_d = \frac{a\tau}{2} = \frac{F_x \tau}{2m} = \frac{\Delta G \lambda}{2 k_B T \tau}. \tag{4.8}$$

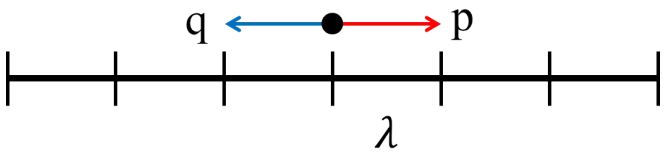

Figure 4.7: 1D random walk process with probabilities of forward jump p and backward jump q.

As Brownian motion is a random walk, a particle's net motion over time can be thought to be the sum of biased displacements. In a one-dimensional random walk, as shown in Figure 4.7, a particle makes l steps to the right with a probability p in n trials, and $n-l$ steps to the left with a probability $q = 1-p$, so that $\langle l \rangle = np$ and $n - \langle l \rangle = nq$.

The distance that the particle travel is the net number of steps in the growth direction (suppose, right):

$$\langle x(n) \rangle = \langle l \rangle \lambda - \langle (n-l) \rangle \lambda = n(p-q)\lambda. \tag{4.9}$$

The drift velocity is then

$$v_d = \frac{\langle x(n) \rangle}{t} = \frac{n(p-q)\lambda}{t} = \frac{(p-q)\lambda}{\tau}, \tag{4.10}$$

with $n = t/\tau$. Equating this to the drift velocity then gives

$$\frac{\Delta G \lambda}{2k_B T \tau} = \frac{(p-q)\lambda}{\tau}, \tag{4.11}$$

or,

$$\frac{\Delta G}{2k_B T} = 2p - 1. \tag{4.12}$$

Driving force, ΔG $[kT/particle]$	Growth	Melting
BCC crystals	0.0343	- 0.0363
FCC crystals	0.0425	- 0.0436

Table 4.3: Driving forces for the crystallization and melting processes.

Thus we find

$$\frac{p}{q} = \frac{k^+}{k^-} = \frac{1 + \frac{\Delta G}{2k_B T}}{1 - \frac{\Delta G}{2k_B T}} \approx 1 + \frac{\Delta G}{k_B T}. \tag{4.13}$$

The equation 4.13 has a relationship between the jump rates k^+, k^- and biasing factor $\Delta G/k_B T$. The free energy bias can therefore be computed from the ratio of the forward and backward jump frequencies. The results are listed in Table 4.3. Figure 4.8 is a 2-dimensional trajectory of a particle during crystallization. The red and blue dot indicate the starting and end point of the path, respectively. While the particles are jumping to join a phase, they are taking a complicated random path. Although they travel in every random direction with a same distance, they take more jumps toward a growing phase along the concentration gradient direction. This results in a growth of the phase during the transition.

4.3.5 Crystal growth rates at different electrical conditions

To check if the drift velocity is affected directly by the electric field, we measured the crystal growth rates at two different voltages, 60 V and 80 V. The comparison is shown in Figure 4.9 (a) and (b), which show the number of particles that join the crystal phase across the interface (1200 μm^2) as a function of time. When the growth rates of BCC ($0.403/sec,\ 0.403/sec$) and FCC ($0.526/sec,\ 0,479/sec$) are divided by the number of particles in the interface ($N_{BCC} = 170,\ N_{FCC} = 176$), they correspond to the net growth rate ($\Delta k = k^+ - k^-$) in Table 4.1.

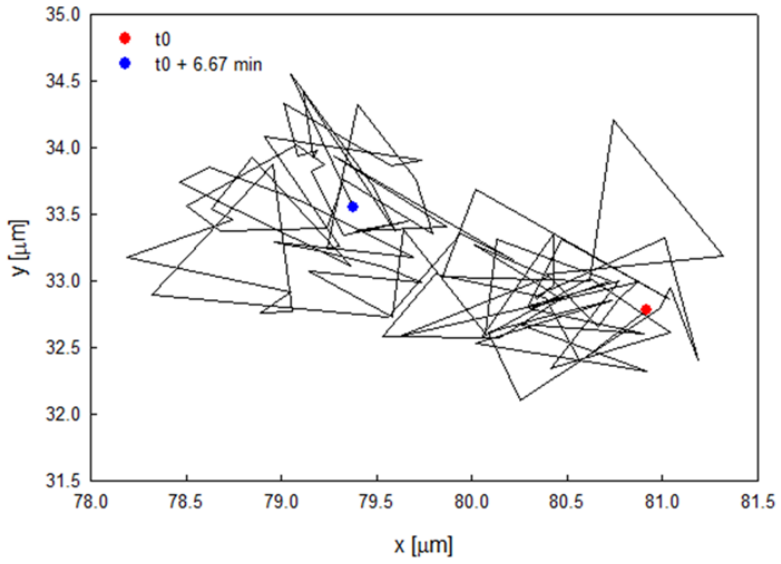

Figure 4.8: 2D projection of the trajectory of a particle near the interface during crystallization.

4.3.6 Interface velocity

The motion of the crystal-liquid interface is caused by a transfer of particles to a growing phase across the interface. When liquid particles join the crystal, each attaching particle adds a unit volume V_p to the crystal. When $\Delta N = N^+ - N^-$ particles join, the interface moves by

$$l = \frac{\Delta N V_p}{A} = \frac{(N^+ - N^-)V_p}{A}, \tag{4.14}$$

where A is the interface area (here: 1200 μm^2). The unit volume V_p in the BCC and FCC crystals are 27.90 μm^3 and 18.54 μm^3, respectively. Figure 4.10 (a) and (b) show the interface velocities during the growth and melting with $v_{growth} = 0.091\ \mu m/sec$, $v_{melting} = -0.164\ \mu m/sec$ for BCC and $v_{growth} = 0.082\ \mu m/sec$, $v_{melting} = -0.099\ \mu m/sec$ for FCC.

(a)

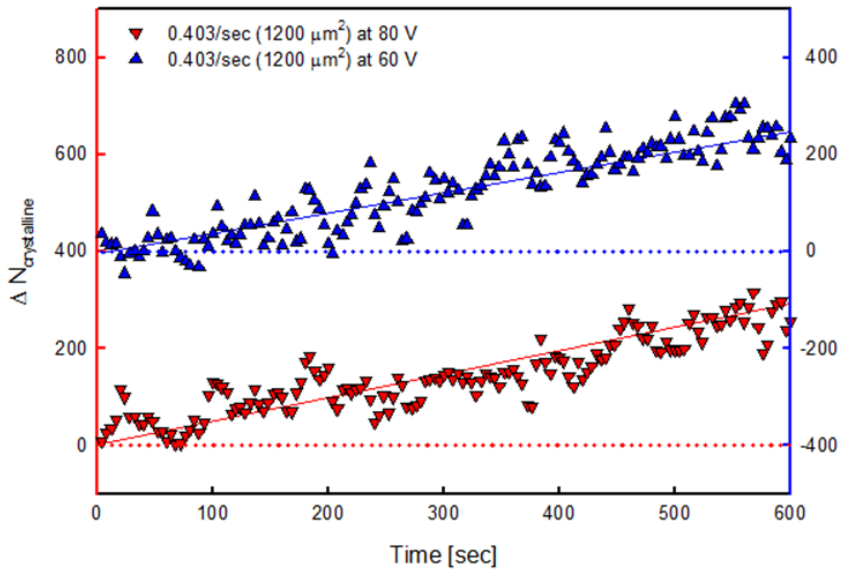

(b)

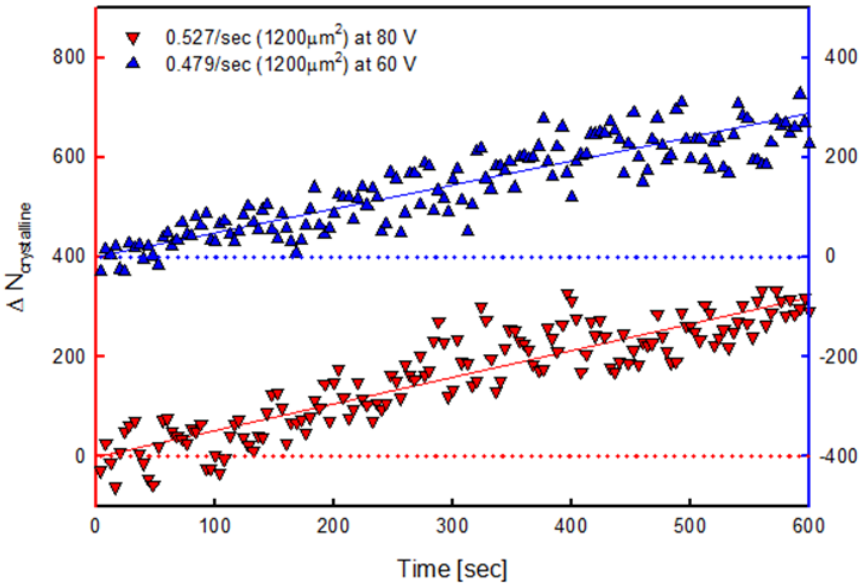

Figure 4.9: Crystal growth speed at two different electrical conditions. Red triangles pointing down for 60 *V*, and blue triangles pointing up for 80 *V*. (a) BCC crystal growth. (b) FCC crystal growth.

(a)

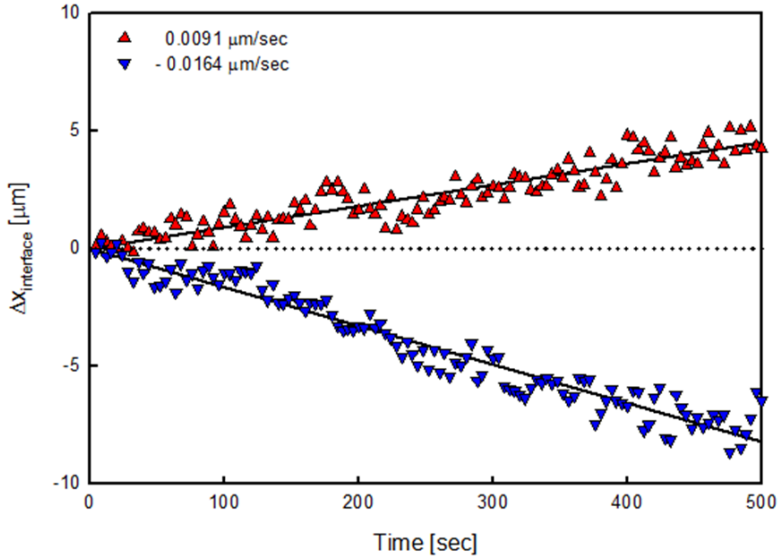

(b)

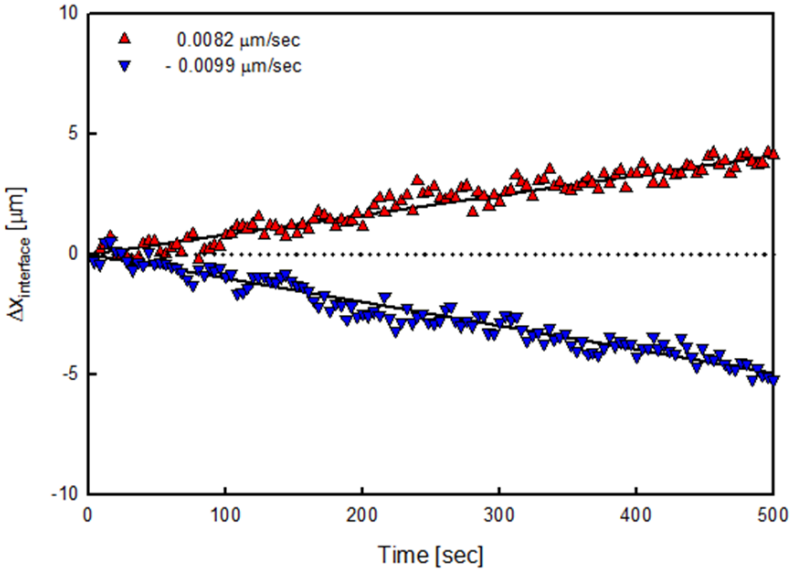

Figure 4.10: Interface velocities of crystallization and melting. Red triangles pointing down for crystal growing when the voltage is stepped from 0 *V* to 80 *V*, and blue triangles pointing up for crystal melting when the voltage is stepped from 80 *V* to 0 *V*. (a) BCC-liquid interface. (b) FCC-liquid interface.

Interface mobility $[m^2/J \cdot sec]$	Growth	Melting
BCC crystals	5.55×10^8	9.12×10^8
FCC crystals	3.57×10^8	4.20×10^8

Table 4.4: Mobilities for BCC- and FCC-liquid interface during growth and melting.

4.3.7 Interface mobility

A key quantity in the kinetics of melting and crystallization is the interface mobility, defined as

$$M = \frac{v}{\nabla G} = v\frac{\lambda}{\Delta G}, \tag{4.15}$$

where v is the interface velocity, which can be determined from the net jump frequencies[42]. Table 4.4 shows the mobility derived using the driving force ΔG in Table 4.3 and the velocity in Figure 4.10; the specific values of λ for crystallization and melting are $\lambda_{BCC} = 0.86\ \mu m$, $\lambda_{FCC} = 0.76\ \mu m$ and $\lambda_{BCC} = 0.83\ \mu m$, $\lambda_{FCC} = 0.76\ \mu m$, respectively. Surprisingly, the mobility for melting is greater than that for the growth in both crystals. Similar asymmetric melting and freezing kinetics have been observed in silicon[37]. This asymmetry is associated with inequivalent entropic contributions of the melting and freezing to the driving force. The free energy driving force ΔG for the growth and melting has the same magnitude, however, possible paths in phase space for a liquid particle to join the crystal are more restricted than for the reverse process.

4.4 Conclusions and outlook

We have investigated the crystallization and melting of colloidal crystals. The electric bottle's control of the particle concentration enabled us to manipulate the transformation between crystal and liquid phases. Crystallization is induced by dielectrophoretic compression and melting by switching off the electric field. A choice of a charge-stabilized colloidal systems produces two types of colloidal crystals, BCC and FCC crystals.

Measurement of the attachment and detachment rates provides detailed insight into the kinetics of solidification and melting. We investigated the Brownian motion of the particles, which is a random walk, to understand the nature of the impingement rate of the crystalline interface. The motion of the solidification or melting front is limited by the random motion of the particles near the interface. This knowledge gives us to have a better understanding of the solidification and melting of the elemental metals, whose growth is collision-limited in atomic systems.

5

Results: The equilibrium interface between a body-centered cubic crystal and a liquid

In this chapter, we studied the dynamics of the interface between a BCC crystal and its liquid in a colloidal system. The interfacial fluctuations are used to determine the interfacial stiffness.

5.1 Introduction

The interfacial energy γ, a key equilibrium property of the interface between two phases, is the free energy cost for the creation of a unit area of interface. Interfaces for gas-liquid, liquid-liquid, or amorphous solids have isotropic free energy, whereas the free energies of interfaces associated with crystals are orientation-dependent with respect to crystal axes and hence $\gamma = \gamma(\theta_1, \theta_2)$. Determining the actual values of the interfacial energy for the crystal-liquid interface is not easy. The method of choice is often computer simulation. A related technique is the capillary fluctuation method, which determines the interfacial stiffness

$$\tilde{\gamma}(\theta) = \gamma + \frac{\partial^2 \gamma}{\partial {\theta_i}^2} \tag{5.1}$$

from the interfacial fluctuations. By performing this measurements in a number of directions, it is possible to determine both γ and its anisotropy[43,44,45].

Interface fluctuations are experimentally accessible in a colloidal system. One study has determined the stiffness of the crystal-liquid interface in the hard-sphere colloidal system[46]. They grew hard-spheres on a template of high-symmetry planes of the FCC crystal and determined the stiffness from the equilibrium fluctuations of the interfaces. However, the stiffness of BCC crystal-liquid interface, which is unknown even from simulations, has not been investigated experimentally because creating it in a colloidal system was hard. The electric bottle is now a powerful means to establish the equilibrated interfaces between crystal and liquid via the concentration gradient. Here, we used the combination of an electric bottle and a charge-stabilized colloidal system to create an equilibrated interface between BCC crystal and liquid.

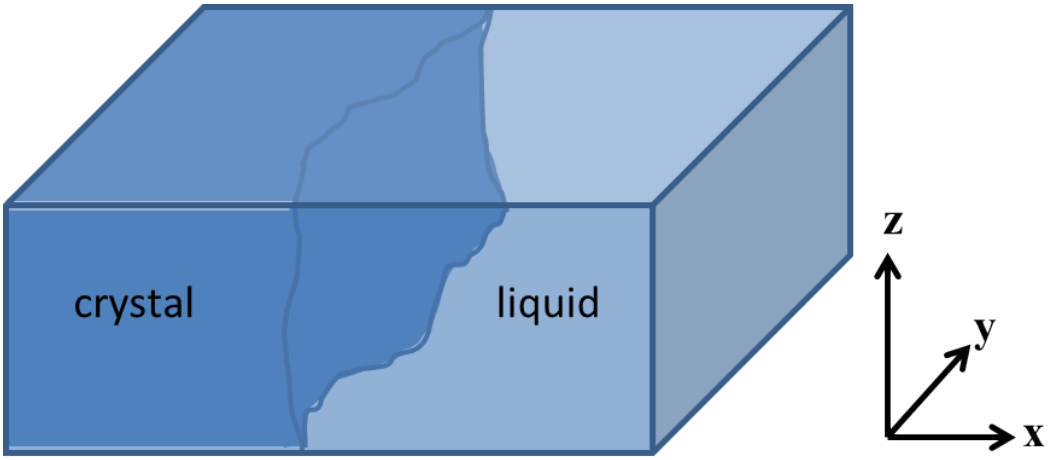

Figure 5.1: Schematic of colloidal crystal-liquid equilibrium interfaces in the sample cell.

5.2 Capillary fluctuation method

We can employ the capillary fluctuation method to an equilibrated crystal-liquid system at a certain condition shown in Figure 5.1.

The capillary fluctuation method is an analysis of the height fluctuations of an interface at equilibrium. Interface fluctuations are associated with a free energy cost. Local fluctuations of the interface can be described by a height function in Equation 5.2 which gives the local height deviation $z(x,y)$ from its average interface height $< z(x,y) >_t$.

$$h(\vec{\rho}) = h(x,y) = z(x,y) - < z(x,y) >_t . \tag{5.2}$$

The Fourier transform of the height function $h(\vec{\rho})$ is defined in Equation 5.3 where $\vec{k} = (k_x, k_y)$

is the two-dimensional wave vector.

$$h(\vec{\rho}) = \sum_{\vec{k}} A(\vec{k}) exp(i\vec{k} \cdot \vec{\rho}) \tag{5.3}$$

In the long wavelength limit, there is a relation between the height fluctuations and the interfacial stiffness[47,48].

$$\langle \mid A(k) \mid^2 \rangle = \frac{k_B T}{L^2 \tilde{\gamma}(\theta) k^2} \tag{5.4}$$

$A(k)$ is the amplitude of the interface height fluctuation with the wavelength $\lambda = 2\pi/k$.

5.3 Experimental details

A colloidal suspension is composed of $\sim$ 1.8 μm PMMA particles and a mixture of tetrachloroethylene and *cis*-decalin. To give a long-range repulsion to the particles, we dissolved 20 *mM* AOT surfactant into the solvent, which results in the formation of a BCC crystal at high volume fraction. The details about sample preparation and the repulsive potential are described in Section 3.1.2. We prepared the suspension with a particle volume fraction of $\phi \sim 0.1$ which is below the crystallization volume fraction. We chose this volume fraction range based on the phase behavior information obtained empirically. We filled the suspension in an electric bottle with three gold electrodes and electrode-free slits between in both top and bottom plates as shown in Figure 3.3. The sample cell was equilbrated for 3 days in the microscope room and then we applied the electric field at 80 *V* and $\omega = 1$ *MHz* for 3 days to make the system reach dielectrophoretic equilibrium. The density gradient is induced by dielectrophoresis, and forms a crystal-liquid interface $\sim$ 100 μm away from the electrode.

To make a comparison with the FCC crystal-liquid interface of the similar experimental sys-

tem, we also prepared the colloidal suspension with 5 *mM* AOT surfactants dissolved. Empirically, 5 *mM* is not high enough to dissociate the surface charges of the particle and to form the inverse micelles, thus the particles don't have sufficient repulsion to form BCC crystals at low volume fraction. But since the particles are slightly charged, they do repel, thereby shifting the crystal-liquid phase boundary from that of hard spheres. For this suspension, the electric field induced density gradient produces an FCC crystal at high volume fraction.

We used $\times$ 63 glycerol objective for the microscope measurements. An image of $100 \times 100 \times 60\ \mu m^3$ was taken every 15 *sec*. While we are scanning the 200 stacks, we took the XY images every 0.25 μm, which gives 240 slices in the Z-direction.

5.4 Results and discussion

Figure 5.2 (a) and (b) show confocal images of an equilibrated interface between a BCC crystal and the liquid obtained in an electric bottle. In the bulk crystal, the number density of BCC crystal is $\eta = 0.04\ \mu m^{-3}$. Empirically, the crystals always formed with a (110) plane parallel to the coverslip; this plane has lowest interfacial tension presumably because it is the densest one in BCC. The orientation of the interfaces was random. The interfaces of two orientations in Figure 5.2 (a) and (b) were achieved simultaneously near the same electrode end. The identification of the interface and interface orientation will be described in Section 5.4.1.

5.4.1 Identifying the interface

In order to define an interface, we use the order parameters ϕ_i and the number of crystal bonds Z_i, which are explained in Section 3.6. Interfacial particles are crystalline particles that have a small number of crystal neighbors. Recall that BCC crystalline particles are defined by sorting out the particles of $\phi_i > 3.5$. Then, according to the other assigned parameter Z_i, the number of crystal neighbors, we categorize the crystalline particles into three groups- crystal

(a)

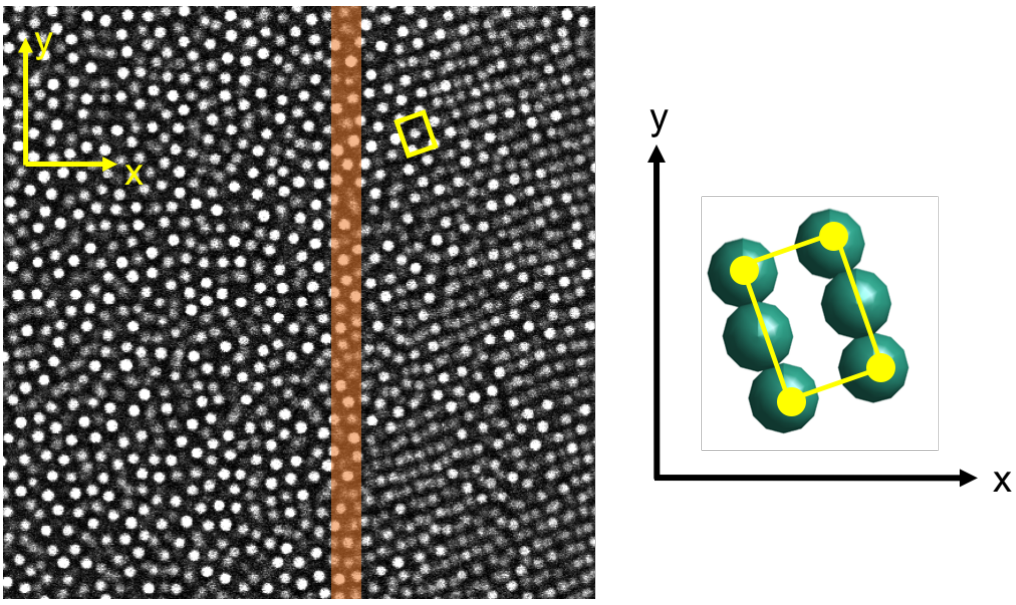

(b)

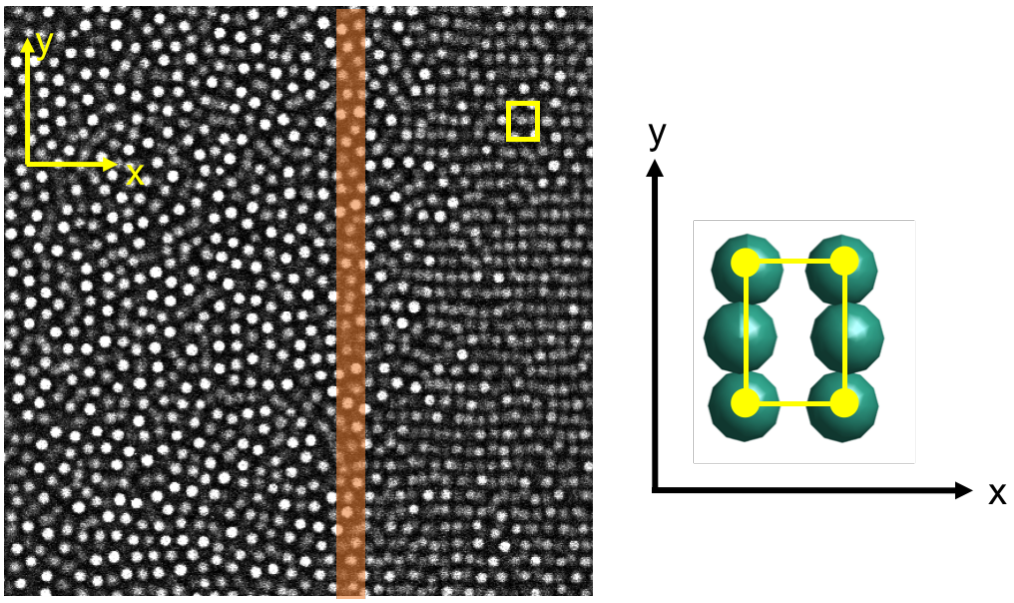

Figure 5.2: Confocal images of an interface between BCC crystal and liquid with interface orientations (a) $(\bar{3}\bar{1}4)$ and (b) $(\bar{1}01)$, and corresponding cubic unit cells of BCC crystals at each orientation in a projected view. Each image is $100 \times 100\ \mu m^2$.

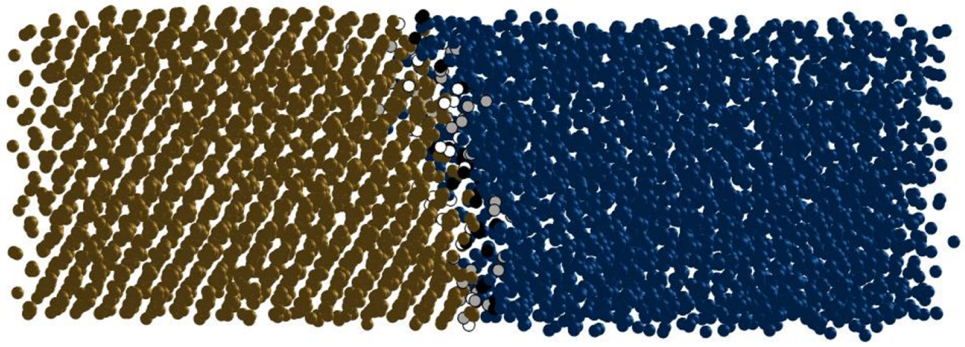

Figure 5.3: A snapshot of BCC crystal-liquid system which has an equilibrated interface in between. Yellow and blue particles correspond to crystal and liquid, respectively. The particles colored in gray are the interface particles and the gray scale corresponds to the number crystal bonds.

($Z_i \geq 11$), interface ($10 \geq Z_i \geq 7$), and remainders ($Z_i \leq 6$). The remainders often gives the particles near the interface and in the liquid some of which have higher ϕ due to coincidental configurations. The particles identified as interface are shown in Figure 5.3. They lie between two phases and form continuous two-dimensional surface.

We obtained 200 configurations of two different interfaces with an area of $45 \times 90\ \mu m^2$. An image stack was taken every 15 seconds. In most cases, the interface induced in an electric bottle is parallel to the yz plane. However, depending on how accurately the electrodes are aligned, the interfaces can be inclined with respect to the yz plane. Nevertheless, these tilted interfaces showed the equilibrium fluctuations by keeping their average positions. To determine the equilibrium height fluctuation in Equation 5.2, we rotate the interface to make it parallel to the xy plane. Based on the rotated data, we obtain the height profiles of every particle at each timestep as a function of x and y. An example of an interface is shown in Figure 5.4. Figure 5.5 shows an interface at a single timestep colored by height deviation profiles along x and y components over a geometrically rectangular interface area.

(a)

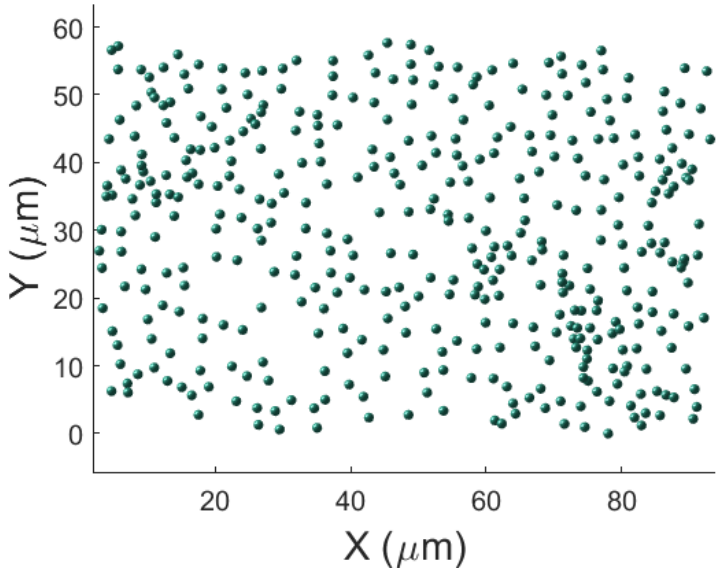

(b)

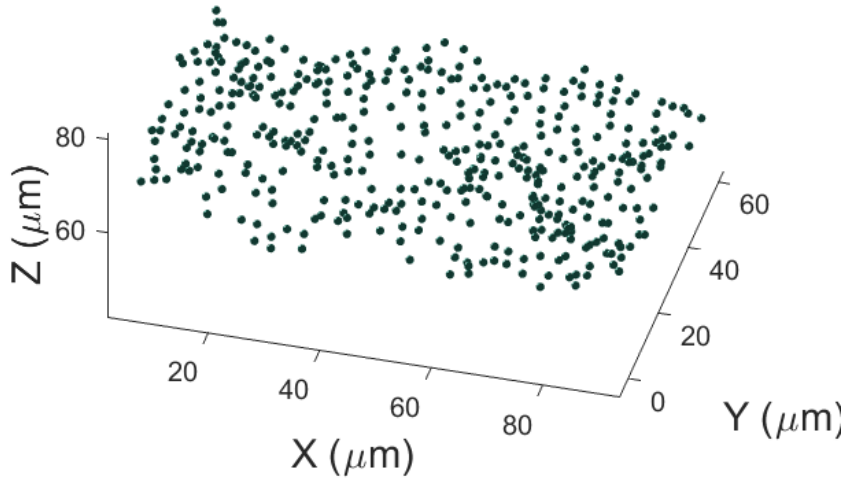

Figure 5.4: A crystal-liquid interface viewed along two angles. (a) A head-on view and (b) a tilted view, showing the height variation and the curvature.

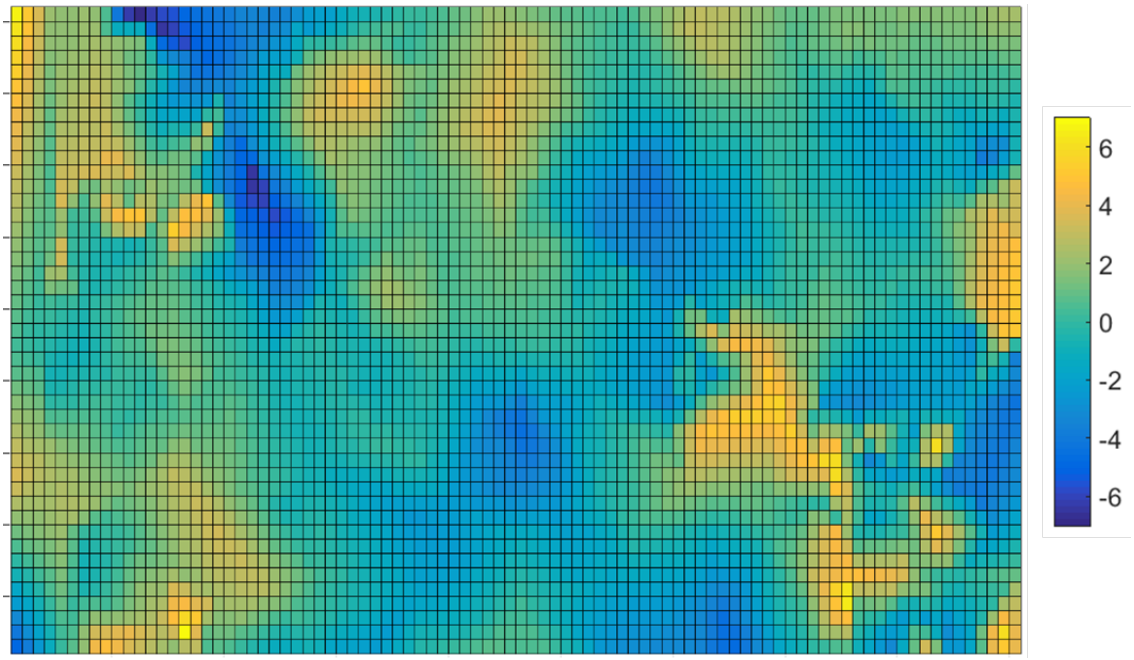

Figure 5.5: A color map of the height profile of a crystal-liquid interface. $\Delta h \approx \pm 7\ \mu m$.

To identify the crystal orientation of the interface planes, we determined the angles between unit cell axes of the BCC crystals and the orientation of the interface. In Figure 5.2, projected views of each unit cell correspond to their confocal image. Although the crystal planes which face up the glass surface are the same, the interfaces where lie between crystal and liquid have different orientations as indicated in the confocal images. Using an equation of plane with a given normal vector to the plane and the unit cubic cell, we can compute the intercepts along the three main axes, which finally give the Miller indices[49]. The orientations of the interface planes in Figure 5.2 (a) and (b) are $(\bar{3}\bar{1}4)$ and $(\bar{1}01)$, respectively.

5.4.2 Determination of the interfacial stiffness

Recall that the interfacial stiffness $\tilde{\gamma}(\theta)$ is a function of the inverse of the averaged squared Fourier components of height profiles $\langle \mid A(k) \mid^2 \rangle^{-1}$ Equation 5.4. To investigate the isotropy of

the stiffness in the plane, we made a plot of the $\langle \mid A(k) \mid^2 \rangle^{-1}$ of the two interface planes.

Figure 5.6 shows log-log plots of the fluctuation spectrum $\langle \mid A(k) \mid^2 \rangle$ vs. k, for the two interfaces. The amplitudes follow a k^{-2} by having a slope of -2 in low k, which is consistent with the behaviors at long wavelengths. The two interfaces have different magnitudes of the amplitudes, indicating that the stiffness depends on the interface orientation.

Figure 5.7 (a) is a logarithmic plot of the $\langle \mid A(k) \mid^2 \rangle^{-1}$ for the $(\bar{3}\bar{1}4)$ interface. The pattern shows isotropy of the stiffness in the low k region. We looked into the long wavelength region which corresponds to low wavevector k region in Figure 5.7 (b), which is also depicted with a linear contour plot in Figure 5.8. The interfacial stiffness for this orientation appears isotropic.

To determine the stiffness of the interface, we computed the inverse Fourier components as a function of k^2 by averaging the components azimuthally, which is plotted in Figure 5.9. The capillary approximation applies in the long wavelength region. Thus, we used a linear regression for several data points in low k, whose slope is $\tilde{\gamma}_{\bar{3}\bar{1}4} = 0.14\ k_B T \sigma^{-2}$ and an offset is $\alpha_{\bar{3}\bar{1}4} = -0.01\ \sigma^{-4}$. This stiffness is measured by fitting from point 2 ($q^2 = 0.2\ \sigma^{-2}$) to point 6 ($q^2 = 0.8\ \sigma^{-2}$) which follow k^{-2} behavior in Figure 5.8.

We performed the same analysis for the $(\bar{1}01)$ BCC-liquid interface. The logarithmic plots of the inverse averaged Fourier components of the $(\bar{1}01)$ plane for the entire k and low k regions are shown in Figure 5.10. In a long wavelength region, we found the isotropy of the Fourier components of the interface, as shown in Figure 5.11 as a linear contour plot. Although the interface has rectangular symmetry, for which isotropy is not expected, the stiffness is nevertheless isotropic.

A linear fit in the long wavelength region gives a slope of $\tilde{\gamma}_{\bar{1}01} = 0.07\ k_B T \sigma^{-2}$ and an offset of $\alpha_{\bar{1}01} = -0.001$, which is less than that of the high-index interface. The slope was estimated by fitting several scatter points in Figure 5.11 that follow k^{-2} behavior in low k. We fit from point 2 ($q^2 = 0.2\ \sigma^{-2}$) to point 5 ($q^2 = 0.7\ \sigma^{-2}$).

(a)

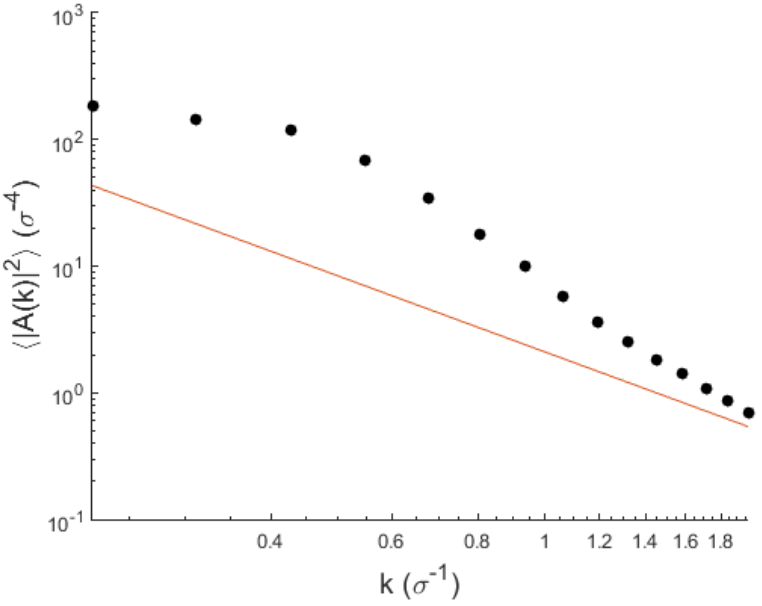

(b)

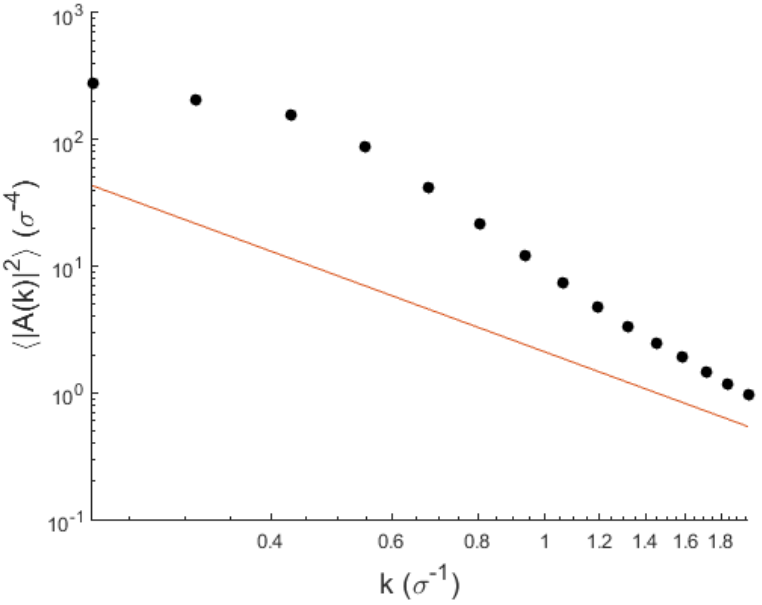

Figure 5.6: Power spectrum of interface fluctuations for k of (a) $(\bar{3}\bar{1}4)$ and (b) $(\bar{1}01)$ interface planes.

(a)

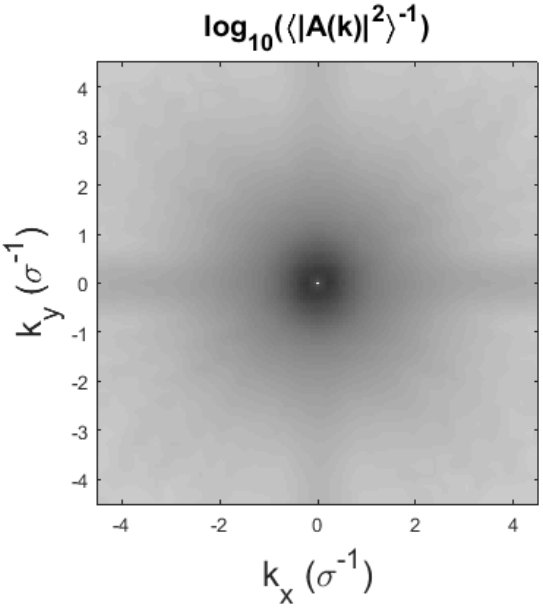

(b)

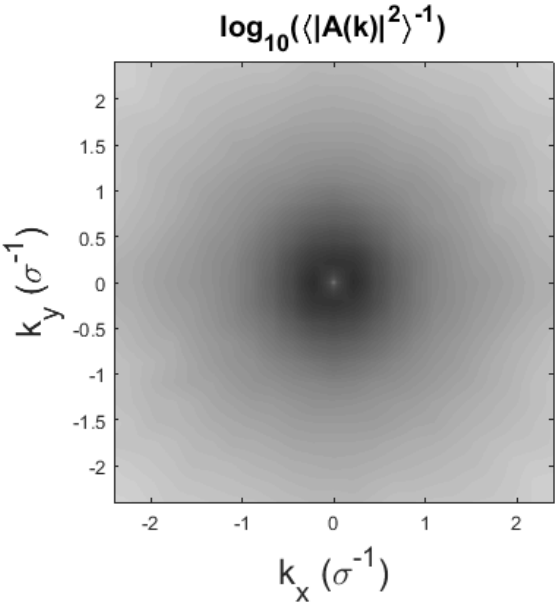

Figure 5.7: Inverse averaged squared Fourier components of the $(\bar{3}\bar{1}4)$ interfacial height profile. Logarithmic grayscale plots of the components (a) in the entire k region and (b) the low k region.

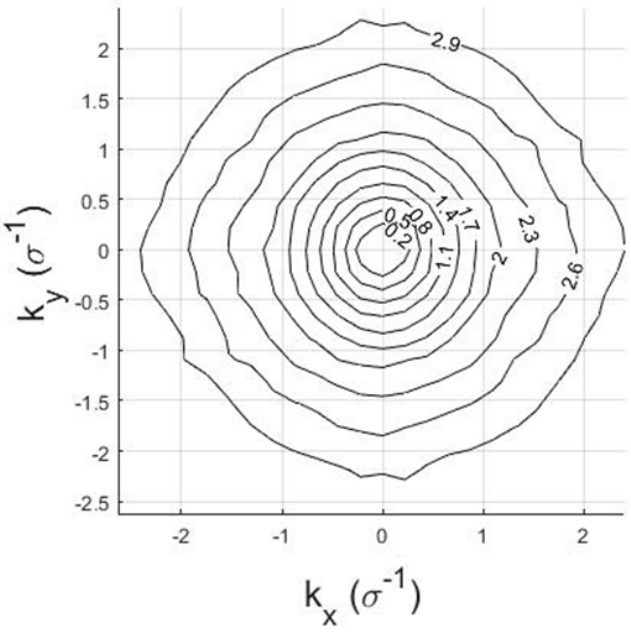

Figure 5.8: A linear contour plot of the inverse Fourier components of $(\bar{3}\bar{1}4)$ interface plane in low *k* region, corresponding to Figure 5.7 (b).

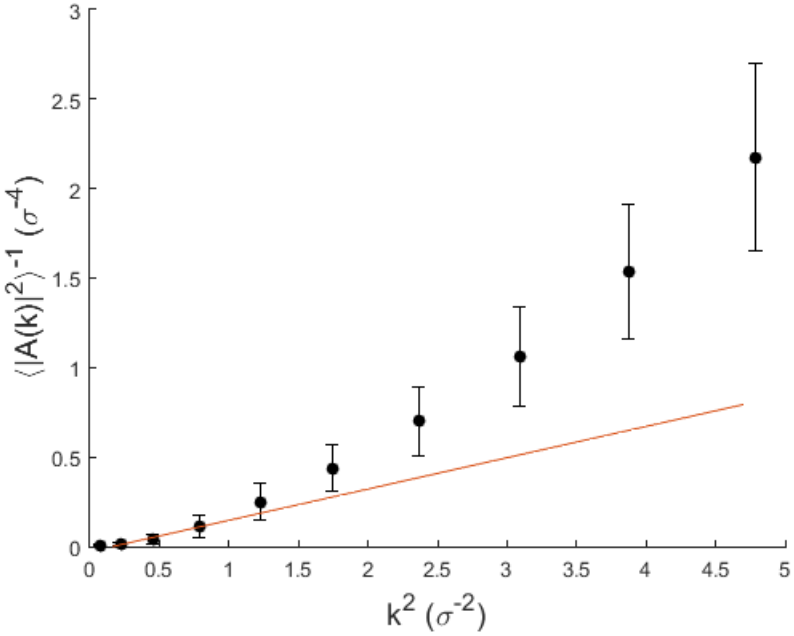

Figure 5.9: Inverse of the azimuthally averaged squared Fourier components of the $(\bar{3}\bar{1}4)$ interfacial height profiles as a function of k^2 with a linear regression to the small wave vector region.

(a)

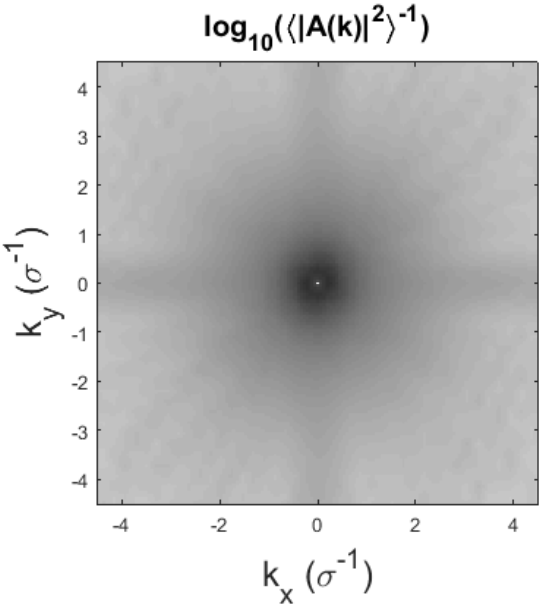

(b)

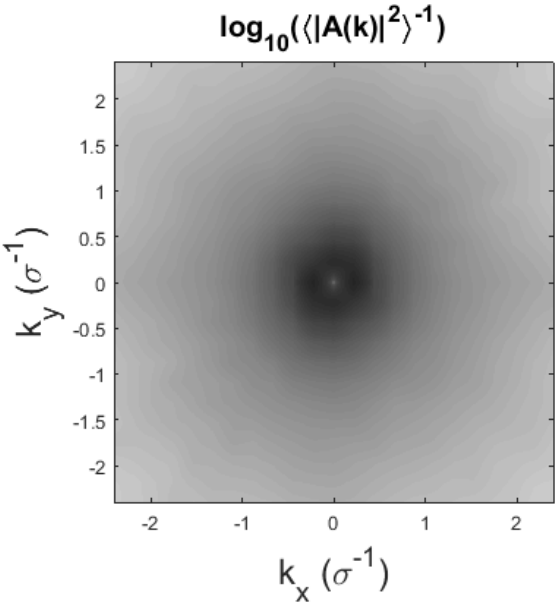

Figure 5.10: Inverse averaged squared Fourier components of the $(\bar{1}01)$ interfacial height profile. Logarithmic grayscale plots of the components (a) in the entire *k* region and (b) the low *k* region.

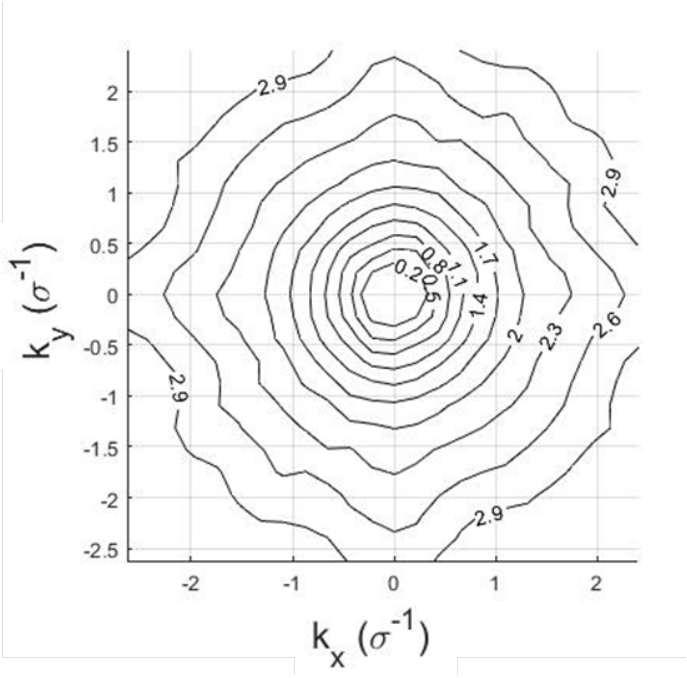

Figure 5.11: A linear contour plot of the inverse Fourier components of $(\bar{1}01)$ interface plane in low *k* region where corresponds to Figure 5.10 (b).

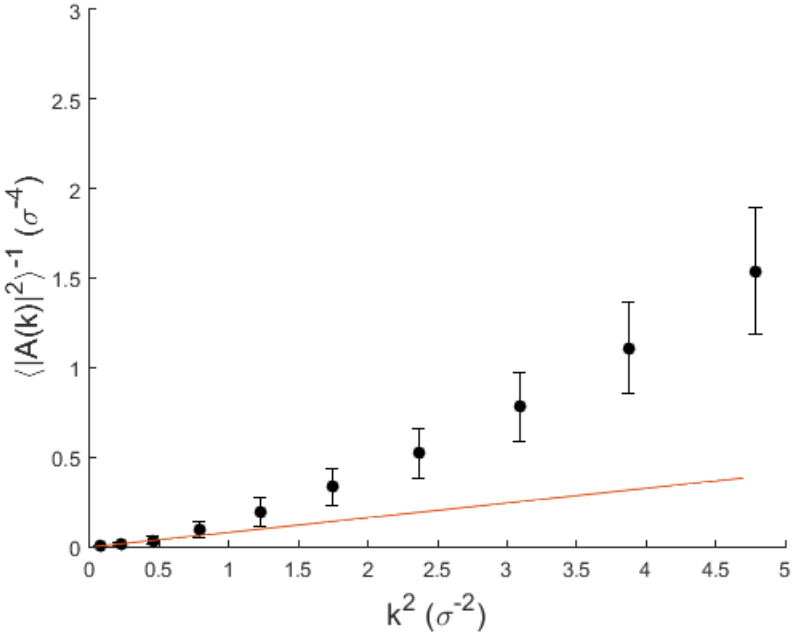

Figure 5.12: Inverse of the averaged squared Fourier components of the $(\bar{1}01)$ interfacial height profiles as a function of k^2 with a linear regression to the small wave vector region.

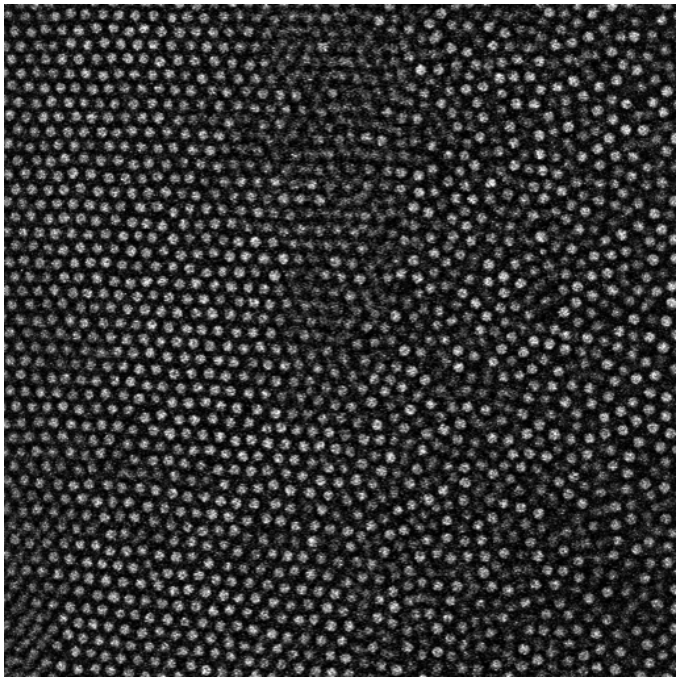

Figure 5.13: A confocal image of FCC crystal-liquid interface, at dielectrophoretic equilibrium.

Compared to the stiffness for FCC crystal-liquid interface in the hard-sphere system (0.66 $k_BT\sigma^{-2}$, 1.1 $k_BT\sigma^{-2}$, and 1 $k_BT\sigma^{-2}$ for (111), (100), and (110), respectively), the stiffnesses in our system are lower, presumably because of the softer interactions from charges[46]. Thus, in order to make a better comparison between BCC and FCC, we have performed the analysis in a similar experimental system composed of charge-stabilized colloids that produce FCC crystals.

Figure 5.13 is a confocal snapshot of an FCC-liquid interface. The repulsive interaction of the particles is weaker than in the BCC system. The number density η of a bulk FCC crystal is 0.07 μm^{-3} and the resulting volume fraction is $\phi = 0.16$, which is much lower than the crystallization volume fraction of hard spheres. The orientation of the interface plane is $(\bar{1}1\bar{1})$ which has 3 fold symmetry, and hence has an isotropic stiffness.

The same analysis was performed with the the equilibrium fluctuations of the interface. The

inverse Fourier component plot is isotropic in the long wavelength region as shown in Figure 5.14.

The linear fit of the slope in Figure 5.15 gives the stiffness of $\tilde{\gamma}_{\bar{1}1\bar{1}} = 0.16\ k_B T\sigma^{-2}$ with an offset of $\alpha_{\bar{1}1\bar{1}} = -0.007$. In comparison with the previous study with a hard-sphere system, $\tilde{\gamma}_{111} = 0.66\ k_B T\sigma^{-2}$[46]. Therefore, the charges seem to modify the dynamics of the interface.

5.5 Conclusions and outlook

We have investigated the BCC-liquid interfaces at equilibrium. The interfaces have orientations $(\bar{3}\bar{1}4)$ and $(\bar{1}01)$, and fluctuations due to capillary waves. Because the surface energy is similar to the thermal energy, thermal fluctuations allow the capillary waves to be observed. Analysis of the height fluctuations yields the stiffness of the crystal-liquid interfaces. For both orientations, the Fourier components of the height profiles were isotropic in the interface plane. The extracted stiffness for high index surface is higher than that of the 2-fold symmetric plane, which correlates with the interface energy: the high index plane, which is composed of a lower-coordinated atoms likely has a higher interface energy. The interface of an FCC crystal, created in a similar experimental system, had a higher stiffness than the BCC interfaces.

The measurements show development possibilities for further studies. With an electric bottle, we can employ many different kinds of colloidal system that are not limited to hard spheres, which should have different dynamics at their interfaces or grain boundaries. Also, to improve the statistics to calculate the stiffness, it should be possible to capture a lot more particles in a larger interface area.

(a)

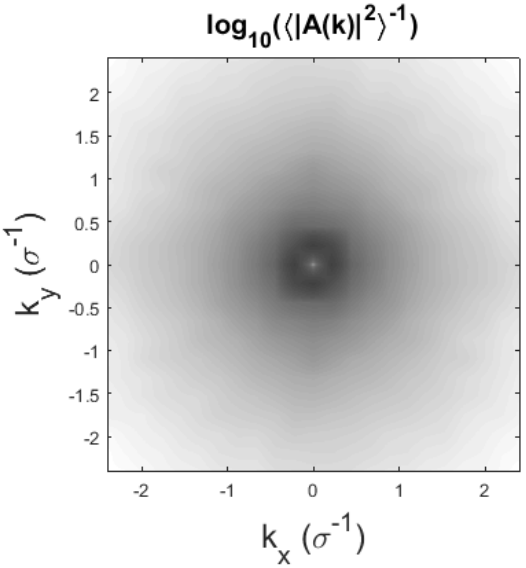

(b)

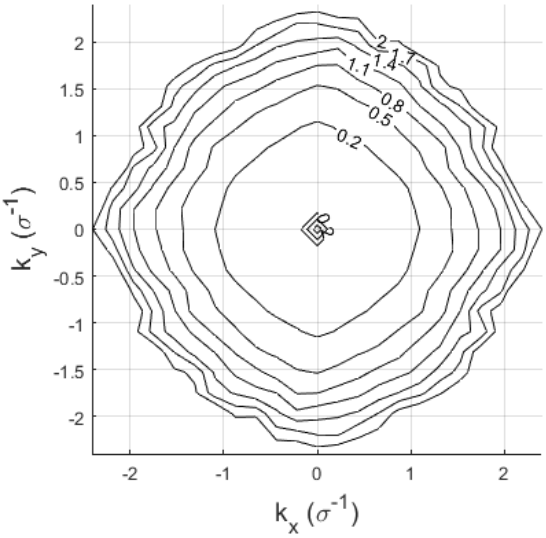

Figure 5.14: Inverse averaged squared Fourier components of the $(\bar{1}1\bar{1})$ interfacial height profile. (a) Logarithmic grayscale plot of the components and (b) contour plot for low k region.

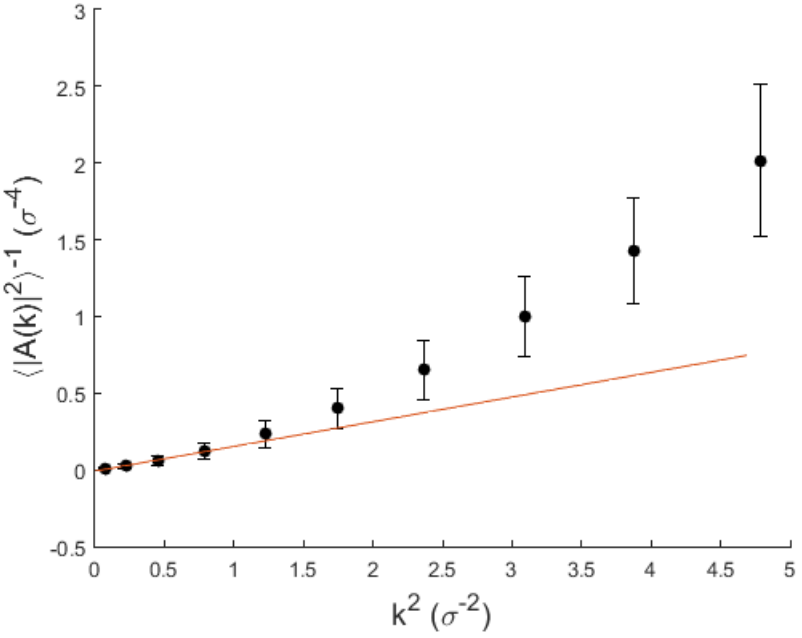

Figure 5.15: Inverse of the averaged squared Fourier components of the $(\bar{1}1\bar{1})$ interfacial height profile as a function of k^2 with a linear regression to the small wavevector section.

6

Results: Experimental observation of the BCC-FCC transition

This chapter describes an experimental observation of the transformation processes between two different crystal structures, BCC and FCC. As an electric bottle controls the packing fraction, it can provide information on details of the solid-solid transition that are difficult to obtain in other experiments.

6.1 Introduction

Crystal-crystal transformations occur in many elemental systems and alloys[50,51]. Many common transitions between two crystals have been studied for industrial applications. However, the atomic-scale details of the transitions still have a lot of unanswered questions. Although colloidal model systems allow us to gain more information on the single particle level, a control over the phase behaviors has been a barrier to the study of crystal-crystal transitions[52].

The crystal-crystal transition we study here is the transformation between BCC and FCC, which is the transition between α-iron with BCC structure and γ-iron with FCC structure[53]. Most previous studies are phenomenological and were performed on atomic crystals with X-ray diffraction and electron microscopy[54,55]. The microscopic kinetic pathways of the transformation, however, remains poorly understood.

In this experiment, we exploited the electric bottle to observe BCC-FCC transitions. The electric field gradient generates a density gradient in structure, therefore, it can induce a transformation from BCC to FCC.

6.2 Experimental details

We used a charge-stabilized colloidal system the details of which are explained in Section 3.1.2. In this experiment, the PMMA particles are suspended in a 20 *mM* AOT solvent mixture. At this amount of surfactant concentration, the colloidal suspension crystallizes into BCC crystalline at a volume fraction of $\phi \approx 0.07 \sim 0.2$. We loaded a suspension of $\phi = 0.15$ into an electric bottle sample and let the sample equilibrate for a week. The colloidal suspension with repulsive particles changes to the ordered state by forming a BCC crystal as shown in Figure 6.1, which is also called as a colloidal Wigner crystal[56]. Once the system is equilibrated with the crystalline structure, we apply the electric field at 80 *V* and $\omega = 1$ *MHz*.

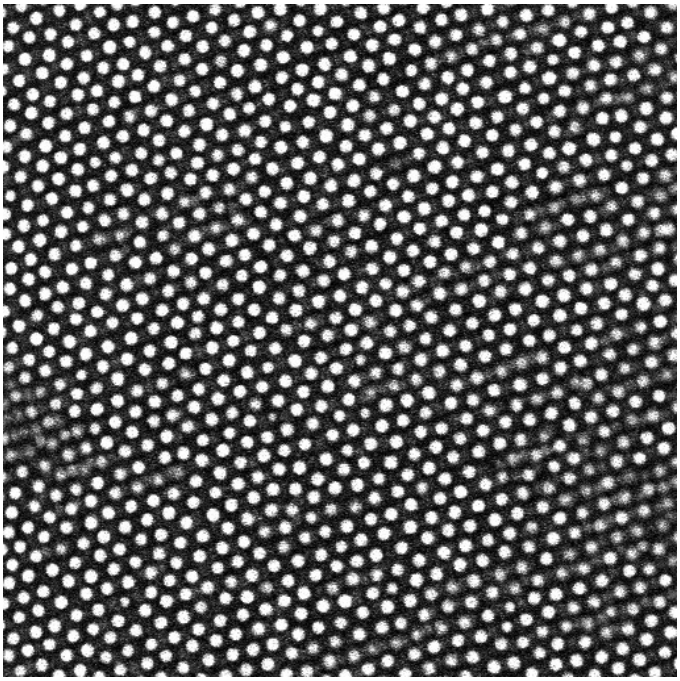

Figure 6.1: A confocal image of a colloidal Wigner (BCC) crystal at $\phi \sim 0.15$ with a (110) parallel to the electrodes.

6.3 Results and discussion

Under the action of dielectrophoresis, the equilibrated BCC crystals are exposed to electric field gradients. Although the particles tend to keep their distances by electrostatic repulsion, this force can be excluded by the dielectrophoretic one. Therefore, in the region of strong electric field, inter-particle distances get shorter and the volume fraction higher until the system reaches an equilibrium. The increase of volume fraction causes the change of structure at a particular value. Figure 6.2 shows the evolution of the structure change from BCC as a function of time. The position of the electrode is on the right side of each image, where the particles are expected to be concentrated and each image was taken in the center plane of the cell. After several hours of dielectrophoretic compression, an unusual structure formed on the right side of the images, and it gradually expanded. From the structure analysis, the crystal has a body-centered tetragonal (BCT) structure. Eventually, when the system reaches dielectrophoretic equilibrium, it forms a phase boundary between FCC and BCC as shown in Figure 6.3.

Imaging the whole transformation process makes it possible to study the dynamics of a BCC-FCC transition. Studies are ongoing to examine the deformation of the crystal unit cell as a function of packing fraction and to determine the dynamics of the transition. By tracking individual particles, we can see where the unusual structure started and how it can cause the transformation from BCC to FCC. Furthermore, we can also investigate the equilibrium fluctuations of the interface which is the grain boundary between two different crystal structures. The observation will provide us new insight for all kinds crystal-crystal transitions.

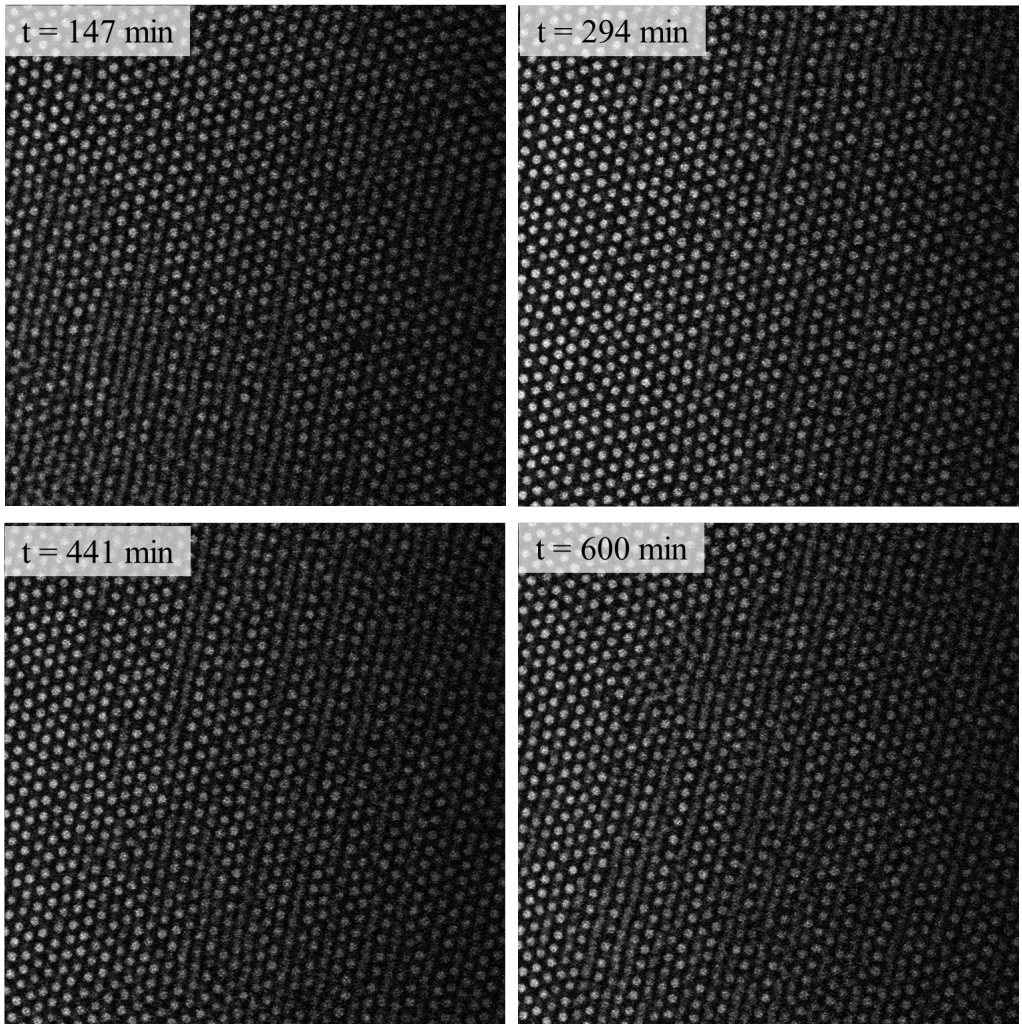

Figure 6.2: Confocal images of the changes in structure during dielectrophoretic compression as a function of time. All images are $100 \times 100 \mu m^2$ and taken at the center plane of the cell.

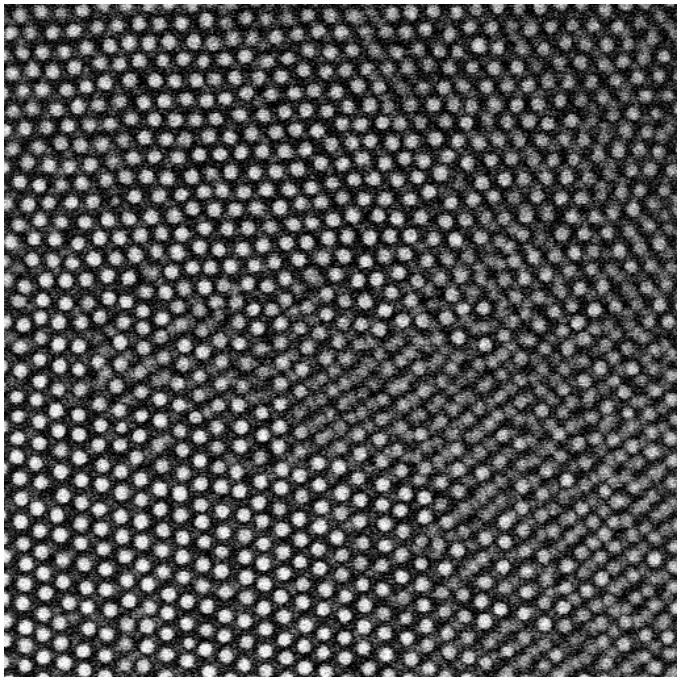

Figure 6.3: A confocal image of an interface between BCC and FCC crystals, where the upper half is FCC and the lower half BCC. The image is $100 \times 100 \mu m^2$ and was taken at $t = 23\ hr$.

7

Conclusion

In this thesis, we have presented the experimental investigations on the crystal-liquid transitions in a colloidal system. Colloids behave as big atoms, thus they are good model systems to study the dynamics of condensed matter. Their phases are determined by the particle concentration which can be controlled by external forces. We studied the transitions such as crystallization and melting in a controlled way. With a confocal microscopy, we were able to obsserve the transitions at single particle level in three-dimension.

In Chapters 2-3, we introduced an "electric bottle" which played a significant role to induce the transitions. A detailed description of colloidal systems and analysis procedures is also described.

Chapters 4-6 presented crystal-liquid transitions and a crystal-crystal transition. We observed crystallization and melting at single particle level and measured the attachment and detachment

rates at the crystal-liquid interface. The random walk governs the atomic attachment, which is equivalent to collision-limited growth of atomic crystals. We obtained the driving force for solidification or melting from a biased random walk. The mobilities for crystallization are greater than melting. We also studied the equilibrated interfaces between the body-centered cubic crystal and the liquid. Using the capillary fluctuation method, we determined the stiffness of the interface from equilibrium fluctuations. The stiffness were observed to be isotropic for the high-index interfaces and those with rectangular symmetry, and to be less stiff than those in hard-sphere colloids. A crystal-crystal transition was also observed.

We explored the crystal-liquid transitions through using the combination of the electric bottle and colloids. Instead having multiple samples to study the phase behaviors as a function of volume fraction, we were able to obtain a concentration-dependent phase diagram in single sample cell. The design of the sample cell can be further developed to induce the various kinds of density gradient. Also, many other phase behaviors resulted from different type of colloidal interactions can be studied.

References

[1] R. A. Jones, *Soft condensed matter*, vol. 6. Oxford University Press, 2002.

[2] F. Perrin, "Mouvement brownien d'un ellipsoide-i. dispersion diélectrique pour des molécules ellipsoidales," *J. phys. radium*, vol. 5, no. 10, pp. 497–511, 1934.

[3] W. B. Russel, D. A. Saville, and W. R. Schowalter, *Colloidal dispersions*. Cambridge university press, 1992.

[4] V. J. Anderson and H. N. W. Lekkerkerker, "Insights into phase transition kinetics from colloid science," *Nature*, vol. 416, no. 6883, pp. 811–815, 2002.

[5] B. V. Derjaguin, "Theory of the stability of strongly charged lyophobic sols and the adhesion of strongly charged particles in solutions of electrolytes," *Acta Physicochim. USSR*, vol. 14, pp. 633–662, 1941.

[6] H. C. Andersen, J. D. Weeks, and D. Chandler, "Relationship between the hard-sphere fluid and fluids with realistic repulsive forces," *Physical Review A*, vol. 4, no. 4, p. 1597, 1971.

[7] P. N. Pusey and W. Van Megen, "Phase behaviour of concentrated suspensions of nearly hard colloidal spheres," *Nature*, vol. 320, no. 6060, pp. 340–342, 1986.

[8] W. K. Kegel and A. van Blaaderen, "Direct observation of dynamical heterogeneities in colloidal hard-sphere suspensions," *Science*, vol. 287, no. 5451, pp. 290–293, 2000.

[9] G. L. Hunter and E. R. Weeks, "The physics of the colloidal glass transition," *Reports on Progress in Physics*, vol. 75, no. 6, p. 066501, 2012.

[10] A. Yethiraj and A. van Blaaderen, "A colloidal model system with an interaction tunable from hard sphere to soft and dipolar," *Nature*, vol. 421, no. 6922, pp. 513–517, 2003.

[11] J. Sprakel, P. J. Lu, T. E. Angelini, F. Spaepen, P. Schall, and D. A. Weitz in preparation.

[12] Y. Mao, M. E. Cates, and H. Lekkerkerker, "Depletion force in colloidal systems," *Physica A: Statistical Mechanics and its Applications*, vol. 222, no. 1, pp. 10–24, 1995.

[13] J. Zhu, M. Li, R. Rogers, W. Meyer, R. Ottewill, W. B. Russel, and P. Chaikin, "Crystallization of hard-sphere colloids in microgravity," *Nature*, vol. 387, no. 6636, pp. 883–885, 1997.

[14] Z. Cheng, W. B. Russel, and P. M. Chaikin, "Controlled growth of hard-sphere colloidal crystals," *Nature*, vol. 401, no. 6756, pp. 893–895, 1999.

[15] Pohl, "The motion and precipitation of suspensoids in divergent electric fields," *Journal of Applied Physics*, vol. 22, pp. 869–871, July 1951.

[16] M. T. Sullivan, K. Zhao, A. D. Hollingsworth, R. H. Austin, W. B. Russel, and P. M. Chaikin, "An electric bottle for colloids," *Physical review letters*, vol. 96, no. 1, p. 015703, 2006.

[17] M. Sullivan, K. Zhao, C. Harrison, R. H. Austin, M. Megens, A. Hollingsworth, W. B. Russel, Z. Cheng, T. Mason, and P. Chaikin, "Control of colloids with gravity, temperature gradients, and electric fields," *Journal of Physics: Condensed Matter*, vol. 15, no. 1, p. S11, 2003.

[18] J. Perrin, *Atoms*. New York: Van Nostrand, 1923.

[19] A. Einstein, "On the theory of the brownian movement," *Annalen der physik*, vol. 4, no. 19, pp. 371–381, 1906.

[20] J. N. Israelachvili, *Intermolecular and surface forces: revised third edition*. Academic press, 2011.

[21] M. F. Hsu, E. R. Dufresne, and D. A. Weitz, "Charge stabilization in nonpolar solvents," *Langmuir*, vol. 21, no. 11, pp. 4881–4887, 2005.

[22] T. Kanai, N. Boon, P. J. Lu, E. Sloutskin, A. B. Schofield, F. Smallenburg, R. van Roij, M. Dijkstra, and D. A. Weitz, "Crystallization and reentrant melting of charged colloids in nonpolar solvents," *Physical Review E*, vol. 91, no. 3, p. 030301, 2015.

[23] C. Böttcher, O. C. Van Belle, P. Bordewijk, A. Rip, and D. D. Yue, "Theory of electric polarization," *Journal of The Electrochemical Society*, vol. 121, no. 6, pp. 211C–211C, 1974.

[24] Z. Ahmad, "Polymeric dielectric materials," *by Silaghi MA. InTech, Rijeka*, pp. 3–26, 2012.

[25] S. S. Dukhin, V. N. Shilov, and J. J. Bikerman, "Dielectric phenomena and double layer in disperse systems and polyelectrolytes," *Journal of The Electrochemical Society*, vol. 121, no. 4, pp. 154C–154C, 1974.

[26] P. Perrot, *A to Z of Thermodynamics*. Oxford University Press on Demand, 1998.

[27] N. F. Carnahan and K. E. Starling, "Equation of state for nonattracting rigid spheres," *The Journal of Chemical Physics*, vol. 51, no. 2, pp. 635–636, 1969.

[28] K. R. Hall, "Another hard-sphere equation of state," *The Journal of Chemical Physics*, vol. 57, no. 6, pp. 2252–2254, 1972.

[29] H. Yukawa, "On the interaction of elementary particles. i," *Nippon Sugaku-Buturigakkwai Kizi Dai 3 Ki*, vol. 17, no. 0, pp. 48–57, 1935.

[30] G. K. Batchelor, *An introduction to fluid dynamics*. Cambridge university press, 2000.

[31] S. Iacopini, R. Rusconi, and R. Piazza, "The ?macromolecular tourist": Universal temperature dependence of thermal diffusion in aqueous colloidal suspensions," *The European Physical Journal E*, vol. 19, no. 1, pp. 59–67, 2006.

[32] Y. Gao and M. L. Kilfoil, "Accurate detection and complete tracking of large populations of features in three dimensions," *Optics express*, vol. 17, no. 6, pp. 4685–4704, 2009.

[33] K. E. Jensen, "Structure and defects of hard-sphere colloidal crystals and glasses," 2013.

[34] P. J. Steinhardt, D. R. Nelson, and M. Ronchetti, "Bond-orientational order in liquids and glasses," *Physical Review B*, vol. 28, no. 2, p. 784, 1983.

[35] C. A. MacDonald, A. Malvezzi, and F. Spaepen, "Picosecond time-resolved measurements of crystallization in noble metals," *Journal of applied physics*, vol. 65, no. 1, pp. 129–136, 1989.

[36] C.-J. Lin and F. Spaepen, "Nickel-niobium alloys obtained by picosecond pulsed laser quenching," *Acta Metallurgica*, vol. 34, no. 7, pp. 1367–1375, 1986.

[37] J. Y. Tsao, M. J. Aziz, M. O. Thompson, and P. S. Peercy, "Asymmetric melting and freezing kinetics in silicon," *Physical review letters*, vol. 56, no. 25, p. 2712, 1986.

[38] A. Isaacs, *Oxford dictionary of physics*, vol. 1. Oxford University Press, 1996.

[39] R. W. Balluffi, S. Allen, and W. C. Carter, *Kinetics of materials*. John Wiley & Sons, 2005.

[40] M. J. Aziz and W. J. Boettinger, "On the transition from short-range diffusion-limited to collision-limited growth in alloy solidification," *Acta metallurgica et materialia*, vol. 42, no. 2, pp. 527–537, 1994.

[41] H. C. Berg, *Random walks in biology*. Princeton University Press, 1993.

[42] J. W. Cahn and A. Novick-Cohen, "Motion by curvature and impurity drag: resolution of a mobility paradox," *Acta materialia*, vol. 48, no. 13, pp. 3425–3440, 2000.

[43] J. J. Hoyt, M. Asta, and A. Karma, "Atomistic and continuum modeling of dendritic solidification," *Materials Science and Engineering: R: Reports*, vol. 41, no. 6, pp. 121–163, 2003.

[44] J. J. Hoyt, M. Asta, and A. Karma, "Method for computing the anisotropy of the solid-liquid interfacial free energy," *Physical Review Letters*, vol. 86, no. 24, p. 5530, 2001.

[45] K. Binder and M. Müller, "Computer simulation of profiles of interfaces between coexisting phases: Do we understand their finite size effects?," *International Journal of Modern Physics C*, vol. 11, no. 06, pp. 1093–1113, 2000.

[46] I. B. Ramsteiner, D. A. Weitz, and F. Spaepen, "Stiffness of the crystal-liquid interface in a hard-sphere colloidal system measured from capillary fluctuations," *Physical Review E*, vol. 82, no. 4, p. 041603, 2010.

[47] D. S. Fisher and J. D. Weeks, "Shape of crystals at low temperatures: Absence of quantum roughening," *Physical review letters*, vol. 50, no. 14, p. 1077, 1983.

[48] M. P. A. Fisher, D. S. Fisher, and J. D. Weeks, "Agreement of capillary-wave theory with exact results for the interface profile of the two-dimensional ising model," *Physical Review Letters*, vol. 48, no. 5, p. 368, 1982.

[49] N. W. Ashcroft and D. Mermin, *Solid State Physics*. Harcourt: New York, 1976.

[50] D. A. Porter, K. E. Easterling, and M. Sherif, *Phase Transformations in Metals and Alloys, (Revised Reprint)*. CRC press, 2009.

[51] W. F. Smith, *Principles of materials science and engineering*. McGraw Hill Book Co., New York, NY, 1986.

[52] Y. Peng, F. Wang, Z. Wang, A. M. Alsayed, Z. Zhang, A. G. Yodh, and Y. Han, "Two-step nucleation mechanism in solid–solid phase transitions," *Nature materials*, vol. 14, no. 1, pp. 101–108, 2015.

[53] R. E. Reed-Hill and R. Abbaschian, *Physical metallurgy principles*. Van Nostrand New York, 1973.

[54] R. Z. Khaliullin, H. Eshet, T. D. Kühne, J. Behler, and M. Parrinello, "Nucleation mechanism for the direct graphite-to-diamond phase transition," *Nature materials*, vol. 10, no. 9, pp. 693–697, 2011.

[55] D. J. Erskine and W. J. Nellis, "Shock-induced martensitic phase transformation of oriented graphite to diamond," *Nature*, vol. 349, no. 6307, pp. 317–319, 1991.

[56] E. R. Russell, F. Spaepen, and D. A. Weitz, "Anisotropic elasticity of experimental colloidal wigner crystals," *Physical Review E*, vol. 91, no. 3, p. 032310, 2015.